# A NEW STATISTICAL APPROACH TO STRAIN-BASED STRUCTURAL HEALTH MONITORING OF COMPOSITES UNDER UNCERTAINTY

by

Hessamodin Teimouri

B.A.Sc., Sharif University of Technology, Iran, 2007

M.A.Sc., Sharif University of Technology, Iran, 2009

A THESIS SUBMITTED IN PARTIAL FULFILLMENT OF

THE REQUIREMENTS FOR THE DEGREE OF

DOCTOR OF PHILOSOPHY

in

THE COLLEGE OF GRADUATE STUDIES

(Mechanical Engineering)

THE UNIVERSITY OF BRITISH COLUMBIA

(Okanagan)

January 2015

## Abstract

Structural Health Monitoring (SHM) technology has been widely applied in different industrial areas. The technology promises to reduce the cost of required safety measures and extend the interval between manual inspections by providing a continuous automated monitoring throughout the life of a given structure. A major concern in developing 'robust' SHM systems, however, is the impact of uncertainty of input parameters in the accuracy and reliability of the monitoring. The purpose of this thesis is implementing advanced statistical pattern recognition techniques capable of considering variations in input parameters, and eventually arriving at a new structural monitoring system immune to uncertainty of parameters. For this purpose, first to show the need for such robust SHM systems in real-world case studies, two different composite structures, namely a T-joint and an airfoil are investigated to statistically evaluate the importance of potential manufacturing/loading errors compared to the presence of delamination (as the most common type of damage in composite materials). Results of this preliminary stage of the study proved the importance of uncertainty analysis in the development of a reliable and precise SHM system. Next, a complete neural network based SHM system was developed for the airfoil case study to investigate single damage scenarios in the form of artificial delaminations of variety of sizes at different locations. The reliability and robustness of the network was assessed in the presence of noisy input caused by inaccurate production process (e.g., thickness variation in composite plies). It was seen that the poor predictability of the network can only be corrected by adding an oversized database of all the noisy scenarios in the training stage, which is practically unacceptable both time- and budget-wise. Next, a new concept of Signal-to-Noise (SN) ratio analysis in SHM was implemented to weigh the first layer of the neural network in the case of uncertain inputs. This approach worked remarkably well, but still a practical concern persisted and that is the precise estimation of the weighting factors. At last, Gaussian Processes (GP) was proposed to train the SHM system in the presence of large uncertainty effects. The new GP SHM in the given case study proved to be distinctively capable of analyzing the input data and predicting both the location and size of the single damage in the composite structure.

# Preface

Some parts of Chapters 4 and 5 have been published earlier as a book chapter and a conference article as follows.

1. H. Teimouri, A. S. Milani, R. Seethaler (2013) “On the effect of fabrication and testing uncertainties in structural health monitoring”, Design of Experiments Applications, M. Silva (Ed.), ISBN: 978-953-51-1168-9, InTech, DOI: 10.5772/56530.

2. H. Teimouri, A. Milani, R. Seethaler, A. Abedian, A. Heidarzadeh, B. Teimouri (2013) “Towards strain-based structural health monitoring of a composite airfoil under uncertainty”, The 19th International Conference on Composite Materials, Montreal.

Results of the proposed Neural Network, Signal-to-Noise Weighted Neural Network, and the GP SHM methods (Chapters 6 to 8) are under submission to separate peer-reviewed journals. Drs. Abbas S. Milani and Rudolf Seethaler have co-supervised the work and co-authored all these publications.

## Table of Contents

## List of Tables

## List of Figures

## Nomenclature

| | |
|---|---|
| $\sigma$ | Stress |
| $E$ | Young's modulus |
| $\epsilon$ | Strain |
| $u(x, y, z)$ | Displacement vector |
| $\gamma$ | Extend and location of damage in the structure |
| $r$ | Position vector |
| $\sigma^{healthy}$ | Stress field in the healthy structure |
| $\sigma^{perturbation}$ | Deviated stress field due to the presence of damage/ abnormalities |
| $\epsilon^{perturation}$ | Perturbation strain field |
| $\{p_n\}$ | Chosen set of points away from the damaged zone |
| $\{p_m\}$ | Chosen set of points in the vicinity of the damaged zone |
| $e_\infty$ | Strain field at $\{p_n\}$ points |
| $f(\gamma, T, r)$ | The stress field as a function of damage attributes and location |
| $k(x, x')$ | Covariant function between the points $x$ and $x'$ |
| $v$ | Matern parameter |
| $K_v$ | Bessel function |
| $\sigma_f$ | Maximum allowable covariance |
| $l$ | Characteristic length scale |
| $\delta(x, x')$ | Kronecker delta function |
| $\sigma_n$ | Noise level |
| $x_*$ | New input value in Gaussian Process |
| $K$ | Covariant matrix |
| $K_*$ | Covariant vector |
| $K_{**}$ | Covariant scalar |
| $\bar{y}_*$ | Predicted output for the new input of $x_*$ |
| $var\ (y\ *)$ | Variance of the predicted output for the new input of $x_*$ |
| $\theta$ | GP hyperparameters |
| $D$ | The training set in GP |
| $\epsilon = N(0, \sigma_n^2)$ | Noise distribution in GP |
| $p(y\|X, w)$ | The likelihood in GP training |
| $\Sigma_p$ | Covariant matrix in GP training |
| $p(\boldsymbol{w}\|\boldsymbol{y}, X)$ | Posterior distribution in GP |
| $p(\boldsymbol{y}\|X)$ | Marginal likelihood in GP |
| $\phi(x)$ | Space of basis functions in GP |
| $\mathrm{I}_{n\times n}$ | Identity matrix |
| $\beta \approx N(b, B)$ | Distribution of the mean functions in GP training; $b$ is the mean value and $B$ is the covariant matrix. |
| SN-S | Larger-the-better static SN ratio |
| SN-T | Smaller-the-better static SN ratio |
| SN-L | Nominal-the-best static SN ratio |
| SN-D | Zero-proportional dynamic SN ratio |

## Acknowledgments

First I would like to thank my co-supervisors, Dr. Abbas S. Milani and Dr. Rudolf Seethaler. Their honesty, advise, constant support, inspiration, kind guidance, and patience were keys to my PhD success. Thank you for everything you have done for me.

I would like to thank the members of my thesis advisory committee, especially Dr. Jason Loeppky and Dr. Lukas Bichler for their accessibility, constructive suggestions, and recommendations. Also great comments and feedback from my external examiner, Dr. Huber Pascal from McGill University, are acknowledged.

My deepest thanks go to my family. I cannot find any suitable words to fully describe and thank their endless support throughout my life. Their love and encouragement made this dissertation possible.

I would also like to acknowledge all organizations and companies provided support for my PhD studies, including the Natural Sciences and Engineering Research Council of Canada (NSERC), Bombardier Aerospace Inc., and the University of British Columbia.

## Dedication

This thesis is dedicated to my family, Rasoul, Fariba, Behnam and Saba for all their endless support.

# Chapter 1

# Overview of the Thesis

### Chapter preview

In this chapter the motivation of this research and a general map of the dissertation are presented. The connections between different chapters will also be highlighted in more detail in the preview section of each subsequent chapter.

# 1. Motivation and the organization of this dissertation

Structural health monitoring (SHM) systems have already been found widespread applications in different industries such as aviation, civil infrastructures, oil, machinery and railway industries. However, to achieve the desired level of safety and avoid false positive/missing negative alarms, the impact of uncertainty factors on the performance and accuracy of these automated monitoring systems (SHM) still requires further investigations. Most of the literature regarding uncertainty analysis in SHM systems is devoted to the study of the *propagation* of uncertainty in an already developed network, in order to post-assess the variation of the outcome caused by potential uncertainty of input parameters. In the current dissertation, a novel alternative approach has been taken: advanced statistical pattern recognition algorithms were implemented to develop a SHM system immune to uncertainty of input parameters *from the first stage of its training*.

The dissertation consists of eight chapters. In the current chapter the overall body of the research and the connection between the subsequent chapters are presented. In Chapter 2, a comprehensive literature review regarding different SHM techniques and examples of successful industrial programs on structural health monitoring are reviewed. Chapter 3 represents the mathematical background of the methodologies used for developing the new SHMs. In chapter 4 a preliminary feasibility study (proof of concept) is conducted on a sample benchmark problem from the literature, namely a composite T-joint, to statistically evaluate the importance of uncertainty analysis and the impact of sensor positioning in measured abnormalities at sensor points. To further show the need for a robust SHM as well as to evaluate the effect of size of sensing system, Chapter 5 focuses on a different case study-- a composite airfoil profile. The airfoil was prototyped and tested by the author and employed in the rest of the thesis with an embedded uncertainty of different nature compared to case study 1 (namely, here a varying thickness of different plies of the composite structure is introduced). Then, in Chapter 6, a multi-layer perceptron neural network is developed to predict the extent and location of internal (unseen) damage in the airfoil case study. It will be shown that the conventional neural network is not able to deal with the large effect of uncertainty. Subsequently, in the same chapter, a Signal-to-Noise (SN) ratio analysis is implemented with the framework of SHM. The SN analysis provides a set of weighting coefficients to modify the conventional neural network by giving more importance to neurons with minimum noise effects (i.e., with higher SN ratios). The practical issues in dealing with SN analysis, however, led to the development of a more novel approach: Gaussian Process (GP) for structural health monitoring, which is presented in Chapter 7. The GP is a non-model based statistical algorithm for pattern recognition/classification, especially when imposed to large noises and uncertain parameters. Finally, in Chapter 8, all the aforementioned efforts in developing a robust SHM approach are summarized. Figure 1.1 illustrates the connection/workflow of the chapters, along with highlights of each.

| | |
|---|---|
| **Chapter 1** | • Motivation and organization of the thesis. |
| **Chapter 2** | • Literature review on SHM techniques and examples of successful programs in the past. |
| **Chapter 3** | • Mathematical background and literature review on Neural Network, Signal-to-Noise analysis and Gaussian Processes. |
| **Chapter 4** | • Proof of concept study 1: Effect of fabrication/testing uncertainties in SHM of a composite T-joint.<br>• Two different sensing architectures are statistically investigated. *Uncertainty effect will be shown to be as important as damage itself, and adding more number of sensors does not necessarily eliminate the effect of uncertainty in SHM predictions.* |
| **Chapter 5** | • Proof of concept study 2: Effect of manufacturing errors on the SHM performance of a composite airfoil.<br>• Only 3 damage scenarios are considered initially. *It will be shown that only about 1/4th of sensors are able to detect damage correctly and all the rest are misled by the noise.*<br>• Next a second and more comprehensive damage signature databse (DSD) was established using 162 damage scenarios. For each scenario, one original model and 5 noisy models (with randomly varying ply thicknesses) are developed. *It will be shown that no sensor is able to merely focus on the damage status and the accuracy of all sensors is affected by the presence of uncertainty.* |
| **Chapter 6** | • The conventional and Signal-to-Noise (SN) ratio modified Artificial Neural Networks.<br>• *It will be shown that the conventional neural network is able to predict damage status only if a large amount of information about the noise is provided during the training stage, or when it is weighted with SN ratios at the input layer.* |
| **Chapter 7** | • A new Gaussian Processes SHM.<br>• The GP approach will illustrate several advantages compared to the above methods, such as no need for data weighting, shorter architectural optimization time and high accuracy. |
| **Chapter 8** | • A summary of all the proposed methods, conclusions, and future work recommendations. |

**Figure 1.1.** The organization of the thesis and highlights of each chapter

## 1.1. Objectives and expected contribution to knowledge

The ultimate goal and expected contribution of this research is to present a new SHM procedure capable of considering uncertainty in the manufacturing/measurement aspects of structures. In this regard, the following successive objectives have been defined:

1. Demonstrate the effect of potential manufacturing/testing errors in SHM through benchmark problems on damage prediction of complex composite structures;
2. Evaluate the effect of size of sensing system and the damage signature database (DSD) in coping with uncertainty effect in SHM of composite structures;
3. Develop a new weighted Artificial Neural Network through a Signal-to-Noise (SN) analysis for an application in SHM under uncertainty;
4. Develop a new Gaussian Processes-based SHM to enhance the prediction of both the location and size of damage in structures under uncertainty, while minimizing the size of required data (DSD) for training of SHM.

# Chapter 2

# Literature Review on Structural Health Monitoring Systems

## Chapter preview

In this chapter a comprehensive literature review on the past successful structural health monitoring programs, mainly in aeronautical and civil engineering applications, is presented. The chapter follows by a brief discussion regarding the importance of uncertainty analysis in structural health monitoring and description of a research program investigating the uncertainty analysis for an aircraft wing under dynamic loading. Finally, the chapter ends with a review of different SHM measurement techniques including (such as vibration-based SHM, fiber optic SH, etc.). More emphasis will be given to strain-based techniques as well as SHM of composites as pertinent to the topic of this dissertation.

## 2.1. Introduction to the concept of Structural Health Monitoring

Sensitive/ high risk structures should be carefully designed such that catastrophic failures can be avoided. Traditionally this has been achieved by considering safety factors in order to compensate for potential lack of knowledge on a structure's full-scale behavior, and/or to create a margin between real-time operational loading and residual strength that is left in the structure's material to carry the load. Reduction in the structure's strength is attributed to degradation and damage induced by the operational loading and environmental conditions over service life. Once more knowledge about a current structure's behavior is gained, safety factors may be reduced without compromising the likelihood of failure. This knowledge (health status of the structure at a given time), in turn, can be of great importance due to its impact on avoiding catastrophic failures, along with economic benefits.

Historically, *safe-life* (i.e., when structural elements are designed to stay operational up to their end of life time) and *fail-safe* (i.e., when the overall failure of a structure is prohibited, in case some main elements fail, by using redundant (reserved) structural elements to carry extra load) methodologies have been main design strategies for many years. But the increasing impact of economic considerations and emerging inspection technologies eventually led to a new design strategy called *damage tolerance* strategy [1]. For damage tolerant designed structures, inspection intervals and damage thresholds are computed. At every inspection point the structure's health is investigated by looking for maximum flaw and crack lengths and orientations, especially in vulnerable spots. If necessary, a modified investigation time is proposed. This method relies on scheduled maintenance intervals and requires considerable hours of out-of-service for the structure. This adds cost and confines economic profits. To produce a damage tolerant structure, two design objectives must be met [2]:

- Controlled flaw growth
- Adequate remaining residual strength considering imperfection

In turn, damage tolerant designs and fracture control includes the following [2]:

- Applying fracture resistant materials.
- Inspectable design.

- Multiple load paths.
- Crack stoppers

Despite the success of damage tolerant design strategies and the advancement of NDI (Non-Destructive Inspection)/NDE (Non-Destructive Evaluation) techniques, some inherent limitations still remained. In particular, the current damage tolerant design philosophy does not provide a continuous assessment of the structure's health status and on-demand interrogations require ground engaging of the structure [2].

Over time, the advancement of Non-Destructive Testing (NDT) technologies, economic justifications, and the occurrence of catastrophic failures eventually led to the introduction of the concept/philosophy of *Structural Health Monitoring* (SHM). It is hard to find a comprehensive, consistent definition of SHM in the literature, but as Boller suggested in [1], "*SHM is the integration of sensing and possibly actuation devices to allow the loading and damage state of the structure to be monitored, recorded, analyzed, localized, quantified and predicted in a way that non-destructive testing becomes an integral part of the structure*". This definition contains two major elements of SHM which are load monitoring and damage diagnosis as the consequence of operational loading, which is subjected to data noise. It should be added that, there is a major difference between the latter design philosophy and the earlier damage tolerance design strategy and that is related to time-based or condition-based inspection intervals. In SHM, by implementing in-situ sensors, actuators and on-board processors, there is no need for extra ground inspections and the overhaul maintenance schedule depends on the current health status of the structure and its damage extent [1].

Three main motivations for increasing interest and investment in SHM philosophy in different industries can be pointed out. The first is avoiding fatal failures and catastrophic events by providing on-line damage extent assessments of structures. The second is the desire toward condition-based health investigations, instead of current time-based schedules. A Time-based schedule requires considerable downtime and has a higher chance of missing flaws and damages that may lead to other failures before the next maintenance schedule. On the other hand, SHM is condition-based monitoring where the structure's current health status is recorded, which eliminates unnecessary downtimes while increasing the safety level. The last motivation factor would be the tendency of many companies that produce high capital expenditure products, such as airframes, jet engines and large construction equipment to move to a business model where they lease this equipment as opposed to selling them. Within this model, the manufacturer would take on the responsibility for maintenance of the equipment and SHM technology enables the company to monitor the structure's health while keeping it in the field to produce revenue and fees would be based on the system life used up and induced damage to the equipment, instead of current rental time arrangements [2].

Figures 2.1 and 2.2 illustrate the position of SHM within the technological evolution of complex structures (Figure 2.1) and Life Cycle Cost – LCC (Figure 2.2) [2, 3]. As Figure 2.1 shows, there is a continuous trend of development from simple to complex structures starting from homogenous materials with their natural properties followed by multi-materials (composites) in which we design a material with desired properties, followed by the next generation which consists of making the properties of structures adoptable to changes in environmental conditions – e.g., using Smart Materials/Structures (SMS). Classically, three types of SMS exist; SMS controlling the shape, SMS controlling the vibration and SMS controlling the health status. Integrated SHM systems belong, at least in the short term, to the less smart type of SMS where structures are made immune by embedding sensors and actuators, while the next step toward smarter structures is towards fully employing self-repairing materials [2].

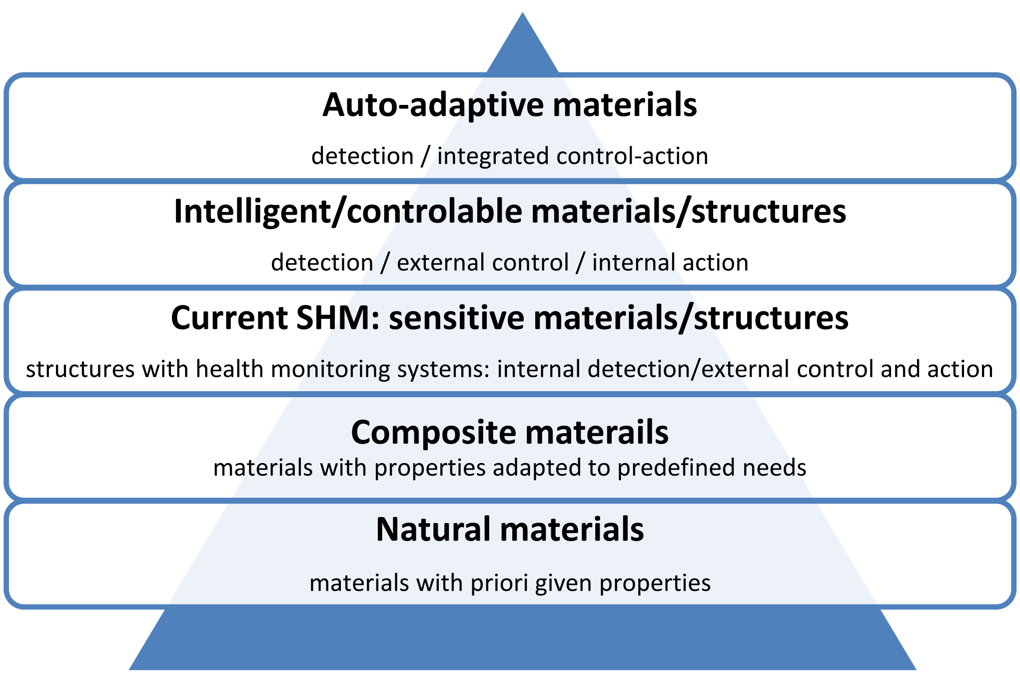


**Figure 2.1.** General evolution of materials/structures and place of SHM [2]

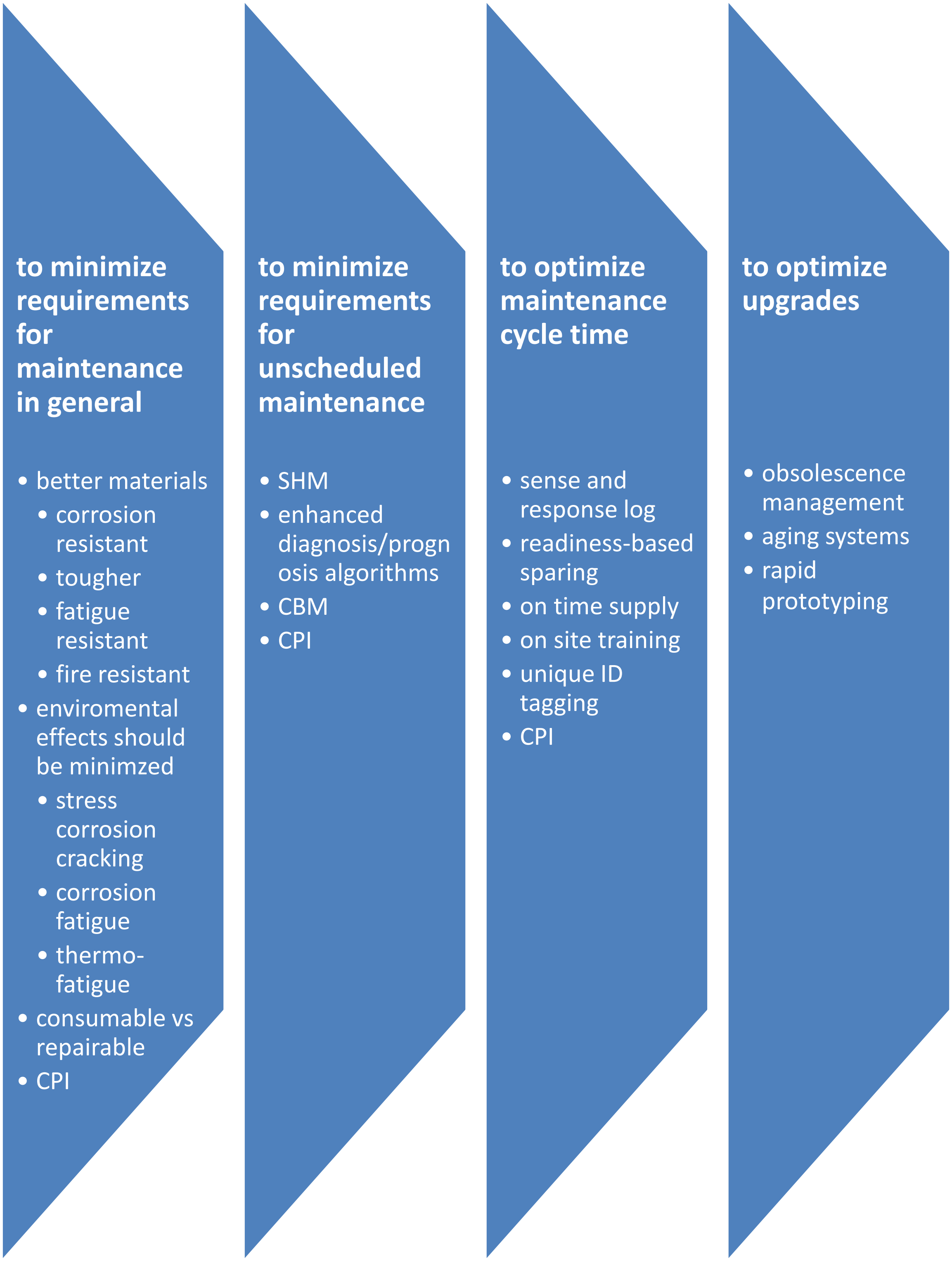


**Figure 2.2.** The position and importance of SHM in reducing Life Cycle Cost [3]

From an implementation perspective, the concept of SHM should be closely viewed with four other subjects: *Condition Monitoring* of rotating and reciprocating machines, *Nondestructive evaluation techniques, Statistical Process Control, and Damage Prognosis* [2-4]. Condition Monitoring (CM) has a long history in the field of damage monitoring for rotating and reciprocating machines, and thanks to well-developed databases, successful monitoring systems have been introduced and applied in different industries. Nondestructive testing (NDT) is analogous to Structural Health Monitoring, but it is carried out offline, locally or globally, and trained technicians and scheduled maintenance programs are required. The Statistical Process Control (SPC) deals with techniques that statistically monitor the behavior of a process and control its quality. SPC is signal-based rather than structure-based, and analyzes raw data transmitted from distributed sensors to monitor abnormalities and estimates the cause of changes in the structure. Damage Prognosis (DP) algorithms are used to predict the remaining life-time of the structure after the current state of damage distributions in the structure has been established, e.g., using SHM techniques. Figure 2.3 illustrates the territories of NDT and SHM and other fields/technologies, such as computing/pattern recognition algorithms and sensor/actuator technologies, which are required to develop a precise Structural Health Monitoring. SHM is fundamentally based on NDT techniques combined with efficient programming and signal processing methods; but additional restrictions limit the number of developed NDTs that can be used as the pillar for making an accurate and reliable SHM system [2].

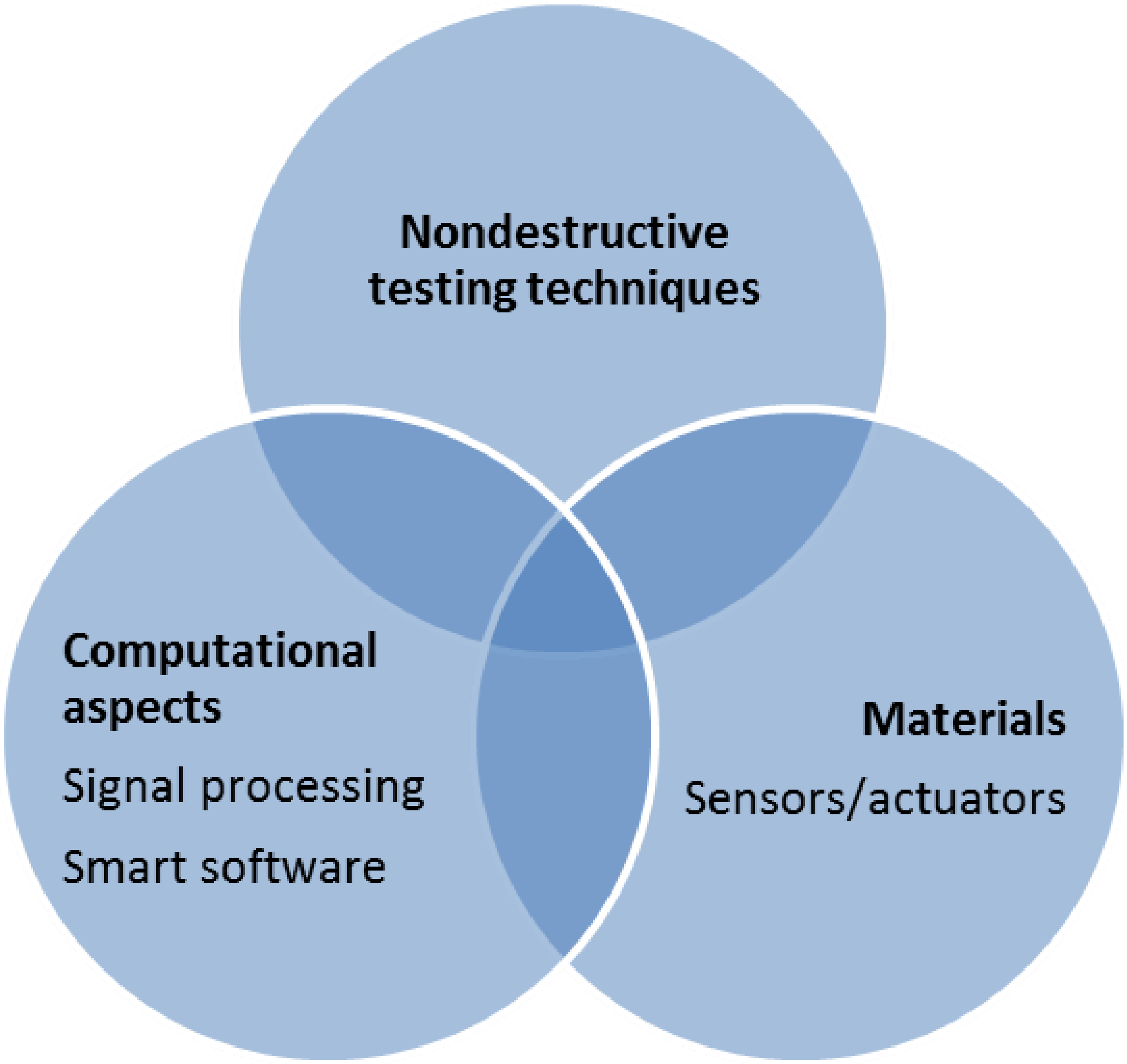


**Figure 2.3.** The basic components of SHM [2]

There are six different levels of complexity and difficulty that can be achieved when implementing a SHM program [2]:

1) **Damage existence realization**; at this level, the system notifies the maintenance operators of the existence of flaws.

2) **Damage localization**; at this level, the approximate location of damage is determined. This information is helpful in case the damage has occurred at vulnerable locations.

3) **Damage severity assessment**; at this level, a quantitative assessment is done to measure the extent of damage.

4) **Damage source identification**; at this level, the source of damage, e.g. delamination, corrosion, fatigue, local failure due to impact loading etc. is identified. This information is important in order to understand the behavior of structures in operational and environmental loading conditions.

5) **Damage prognosis**; at this level, the future system performance is anticipated by assessing the current damage state, estimating the future loading for that system, and by making predictions through simulation and past experience.

6) **Self-healing of damage**; at this level, the structure is made of smart materials and is equipped with an SHM system which generates suitable commands to both reduce/eliminate the source of damage and treat the damaged part of the structure. For instance, if a crack is detected in a structure, actuators can change the local stress flow in order to keep the crack tip at compression loading.

## 2.2. Review of some Structural Health Monitoring programs

The literature regarding the development of SHM systems for different industrial applications can be divided into five categories:

- Condition monitoring of reciprocating machinery
- Oil industries
- Railway industry
- Civil infrastructures
- Aeronautical structures

In this section, a concise review of SHM in the field of aeronautical engineering is presented, as related to the topic of subsequent chapters in this PhD thesis. Only a few programs are pointed out in this field and further information can be found in other works such as [5].

The Shuttle Modal Inspection System (SMIS) which is based on vibration damage identification techniques has been used since the 1980s to monitor fatigue damage in the components such as control surfaces and lifting surfaces which are covered by thermal protection. Along the development of space station programs, vibration-based techniques have been used to monitor debris impact damage on truss links by implementing analytical/experimental methods, aimed at identifying modal properties of the structure caused by reduction in stiffness indices [2].

Since the 1990s, Fiber-Optic sensors have been used to monitor delamination caused by debris impact on reusable composite fuel tanks of the launch vehicles. The main challenge has been the different behavior of composites under impact loadings compared to identical metallic structures [2].

In the past decade, piezoelectric transducers have been of much interest in the Structural Health Monitoring of aero-structures. BAE (Broadband Acoustic Emission) [7-9] applied these transducers to the F-16 fuselage and full scale Boeing 777, BALRUE [10, 11] applied them to full scale Airbus wings, AHMOS [12] applied them to the Eurofighter's composite wing box and fuselage panel, IMRS (Integrated Monitoring, test and Recording Subsystem) applied them to the Eurofighter2000 [13,14], AEFIS (Acoustic Emission Flight Instrumentation System) [15] applied them to the DC-XA Delta Clipper, and AE-HUMS (Acoustic Emission-Helicopter health and Usage Monitoring System) [16] was developed for detecting damage in helicopter drivetrains.

References [7] and [8] describe the development and characteristics of a system based on Broadband Acoustic Emission waves which have been designed to automatically monitor crack status and growth rate with good accuracy using over a thousand installed sensors distributed over the structure. The Broadband Acoustic Emission (BAE) system has been applied to monitor fatigue damage on full-scale Boeing 777 [9] and F-15 [10] in which several components such as bulkhead and connecting wing lugs were investigated using lamb waves in the two modes of pitch-catch and pulse-echo.

Similar to the BAE program, British Aerospace in cooperation with Lloyd's Register of Shipping (LR), Ultra Electronics Ltd. (UE) and Ocean Systems developed a modified acoustic emission SHM system called BALRUE. Before being applied to a full-scale metallic wing of the Airbus A320, the BALRUE system was previously verified on large-scale metallic and composite structures and the reliability of the system was proven [11]. Installation of surface-bonded acoustic sensors on the Airbus wing subjected to fatigue loading of 30,000 simulated flight cycles, corresponding to 14 months of testing period, resulted in early detection of artificial damages implemented in the structure just after a couple of months. This system was also able to detect and locate early fatigue damages after two months which could not have been detected by conventional nondestructive techniques after eight to eleven months of testing period.

Active Health Monitoring of Structures (AHMOS) is another program which uses Fiber Brag Grating (FBG) sensors, Acoustic Emissions and strain-gauges to monitor the health status of the pylon housing box of a Eurofighter and a composite fuselage panel of a Fokker 100 [12]. This system seems to be less advanced compared to BAE regarding poor signal de-noising capability and accuracy of damage localization.

Integrated Monitoring, test and Recording Subsystem (IMRS) is another Structural Health Monitoring system developed for the Eurofighter [13, 14]. The IMRS system was designed for EF2000, and integrates both on-board avionics and ground-station support system. Two different versions of IMRS have been developed which are strain gauge-based or parametric-based fatigue monitoring systems.

In the strain gauge-based IMRS system, the stress distribution is calculated based on the measured strain distribution obtained from strain gauges at an iteration rate defined by the user. A real-time cycle counting algorithm is performed in order to calculate the stress-spectra and the fatigue life of the structure. In the parametric-based IMRS system, real time data are captured from flight control systems, armament control system and fuel gages. These data are then fed into a pattern recognition algorithm which calculates the stress distribution by comparing the data provided by flight systems and the data stored in the internal memory, representing approximately 17,500 templates. The templates derived from finite element simulations and ground fatigue tests, corresponding to identical aircraft configuration and flight parameters. This process is iterated to generate stress history and stress-spectra which leads to damage calculation.

Acoustic Emission Flight Instrumentation System (AEFIS) is a Structural Health Monitoring system based on acoustic emission and acousto-ultrasonic sensors [15]. The AEFIS was successfully installed on board of the DC-XA Delta Clipper to primarily provide feedback information about the fuel tank structure and other parameters, such as temperature, vibration and background noise, in the rocket. The AEFIS was then used to monitor damages induced by debris impact. In the event of an impact, the Acoustic-Emission (AE) sensors roughly detect and localize the possible damage, and then the Acousto-Ultrasonic (AU) sensors will actively pulse the AE sensors in a vicinity of the damage zone in order to localize the damage and quantify its extent and severity. This information was processed by an algorithm to determine the risk of structural break-up for the next re-entry to the atmosphere to execute go/no-go command.

Airbus A380 is the subject of one of the most comprehensive Structural Health Monitoring programs. The SHM requirements pursued by Airbus follows the NASA DoD (Department of Defense) TRL (Technology Readiness Level) requirement list; namely TRL6 which requires the most advanced technologies available [17]. The two dominant requirements of TRL6 are reliability and durability. To ascertain reliability, both probability of detection (PoD - the same concept and definition as in conventional NDTs) and pyramidal testing algorithms should be combined. The pyramid of testing dictates gradual testing and verification of the developed SHM system starting from a large number of coupon tests to subcomponent tests (at scales of 3m $\times$ 5m) and full-scale testing. Currently Airbus A380 SHM system consists of 6 different types of sensors (Figure 2.4), each responsible for monitoring specific parts of the aircraft [17]:

- Comparative Vacuum Monitoring (CVM)
- Acoustic Emission (AE)
- Eddy Current Foil Sensors (ETFS)
- Crack wire sensors
- Imaging Ultrasonic (IA)
- Acousto-Ultrasonic (AU)

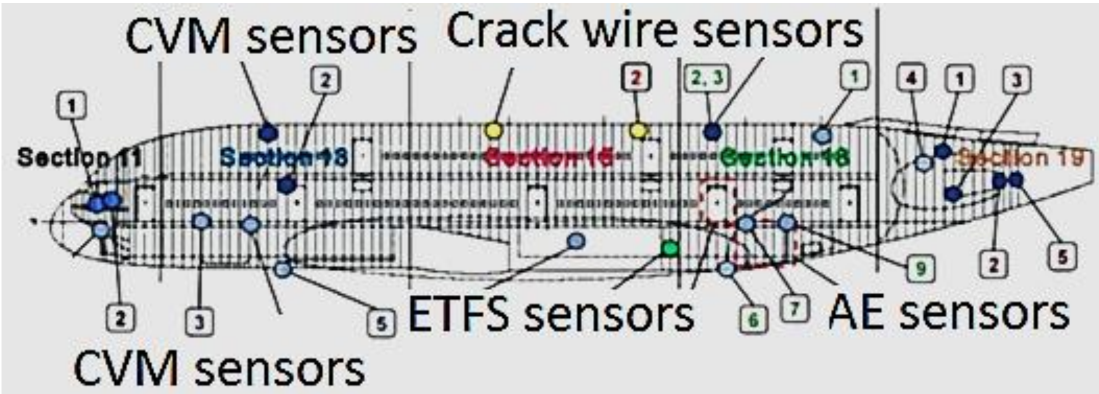


**Figure 2.4.** Position and type of different SHM sensors for Airbus A380 [17]

For certification of airplanes, Airbus carries out a large number of tests. For instance, the three major structural tests for A380 are [17]:

- A380 ES-the static test of the entire structure
- A380 EF-the full scale fatigue test on the entire structure
- A380 RET-a combined static and fatigue test carried out on the rear part of the fuselage and empennage

The A380 EF is a comprehensive structural testing plan which is used to prove fatigue worthiness and damage tolerance of the main metallic structure during the proposed service life of the aircraft. This program consists of different subsystems, such as the test specimens representing the metallic primary structure, the dummy parts and load transmitter features, test rigs, pneumatic loading system and data acquisition system. The corresponding fatigue cycling started on September 1, 2005 and was successfully accomplished with 5000$^{th}$ simulated flight cycle on December 24, 2005. More detail regarding the test setup and the corresponding design requirements are found in [17].

In order to summarize and mention some other international research regarding SHM in aeronautical engineering, Table 2.1 has been taken from the literature review of Auweraer & Peeters [5].

**Table 2.1.** International projects on SHM systems and technologies in aeronautical engineering (source: [5])

| Acronym | Researcher | Duration | Research type | Title | Results |
|---|---|---|---|---|---|
| **OSMOS** | Bertin et Cie | 1992-1995 | Sensors & control | Optical fiber sensing system for monitoring of structures | Quasi-distributed polarimetric sensing system; microwave sensing system; impact sensor |
| **MADAVIC** | U. Napoli Federico II | 1996-1998 | Sensors & control | Magneto-restrictive actuators for damage analysis and vibration control | Magneto-restrictive actuators for vibration-based damage detection and active control |
| **MONITOR BAE** | Defense Ltd | 1996-1999 | Sensors & control | Monitoring online integrated technologies for operational reliability | Multiple sensor technologies, optical fibers, acoustic emission, were evaluated and integrated in a flying test-bed |
| **DAMASCOS** | Uni. Strathclyde | 1998-2001 | Sensors & control | Damage assessment in smart composite materials | Ultrasonic excitation combined with piezo and optical detectors and DSP analysis of scatter patterns |
| **AMADEUS** | CASA | 1998-2001 | Monitoring | Structures accurate modeling and damage detection in high safety & cost structures | Comparison of accurate reference models with in-service measured behavior. Detection of damage using Neural Network |

| | | | | | |
|---|---|---|---|---|---|
| **HIPER-CRACK** | SENER | 2000-2003 | Monitoring & crack growth prognosis | High performance approach to fatigue crack analysis and life prediction | Advanced tools for predicting crack initiation and growth |
| **ADMIRE** | Alenia Aerospazio | 2000-2004 | Monitoring & crack growth prognosis | Advanced design concepts & maintenance by integrated risk evaluation for structures | Develops a probabilistic foundation of damage tolerant design (using crack growth and residual strength calculations) |
| **SINOPSYS** | LMS Int. | 1997-1999 | Monitoring | Model-based structural monitoring using in-operation system identification | in-operation system identification, novel statistical test-based detection method |
| **FLITE** | SOPEMEA | 2001-2003 | Monitoring | Flight test easy | in-operation system identification, flight flutter analysis, use of automatic modal analysis |
| **COST-F3** | Uni. Liege | 1997-2001 | Networks-Cost | Structural dynamics | Model updating, structural health monitoring and identification of nonlinear systems |
| **ADSTREFF** | BAE Systems | 1998-2000 | Networks-BETN | Targeted research action in advanced structural efficiency | From design & manufacturing to service life monitoring |
| **ASSET** | Uni. Strathclyde | 1998-2001 | Networks-BETN | Application of smart structures in engineering technology | Basic technologies (sensing, materials, actuation) and integrated tools/software |

## 2.3. Importance of Uncertainty Analysis in Structural Health Monitoring

From the review above, it is believed that current and future computer aided SHM designs will continue to rely increasingly on computer simulations and modeling tools for a wide range of applications. However, a basic concern is the reliability and robustness of these systems when imposed to practical uncertainties in the data/input parameters or system characteristic features. To elaborate on the concept of uncertainty propagation, consider a sample SHM system developed for an aircraft shown in Figure 2.5.

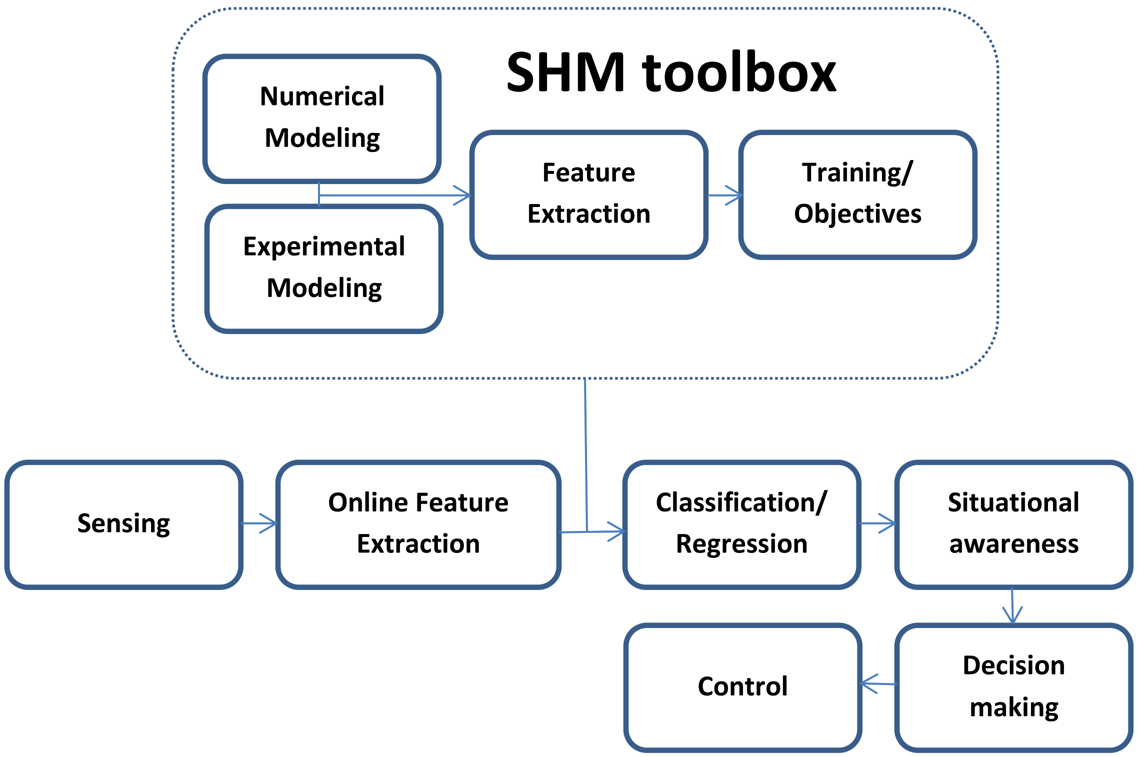


**Figure 2.5.** Example of an SHM system developed for an aircraft [2]

The uncertainty of structure parameters and the modeling process itself may put the performance and accuracy of the output/damage predictions at risk at many levels of the system development process. The uncertainty may come from the sensing systems by means of inaccurate data transmitted from sensors or imprecise database developed during the damage signature development process, manufacturing errors, environmental noises, loading perturbations, or the feature extraction/classification toolboxes which could be occasionally misleading and result in a non-robust-imprecise Structural Health Monitoring system.

The majority of the earlier SHM research works investigating quantification, fusion and propagation of uncertainty have focused on the development of neural network algorithms, and uncertainty analysis has been a separate, time-consuming stage after the network training is accomplished. More precisely, it has been only to assess the sensitivity and accuracy of an existing/developed network using recognized theories of uncertainties such as classical probability theory, evidence theory and convex models (rather than being an integral part of the network development from the beginning—i.e., at the training stage).

Although uncertainty analysis is and should be a crucial part of any SHM system design, only a small number of publications describe the process of performing uncertainty analysis in the field. For instance, Manson et al. [18-21] performed uncertainty analysis for an accelerometer based SHM system for the Gnat jet trainer wing located at DSTL Farnborough, as shown in Figure 2.6. The wing was equipped with 12 accelerometers to measure the vibration response induced from a shaker installed on the underside of the wing surface. The wing had nine removable panels p1-p9 (Figure 2.7) which could be removed and replaced to provide a representation of changing conditions on the wing structure. Data were collected from the installed 12 accelerometers (Figure 2.8) for a variety of healthy-normal conditions (when no panel was removed) and simulated damage data. The accelerometer were organized into 3 groups (A, B and C) and instead of recording individual responses, the experiments were designed to measure the ratio of recorded accelerations between transducer pairs AR/A1, AR/A2, etc., resulting in 9 measurement variables recorded in the frequency range of 1024-2048 Hz. The effect of simulated damage on the spectral response of the transmissibility functions was modeled by a systematic removal of panels. For each damage scenario (panel removal) 100 individual measurements were recorded twice (two replications) for each of the nine defined transmissibility ratios, resulting in a total of 16,200 damaged simulations. Additionally, seven healthy conditions were recorded for each of the nine transmissibilities, taking 100 individual measurements leading to 6,300 results representing the structure’s healthy condition. This information was then fed into a Multi-Layer Perceptron (MLP) neural network implemented by NETLAB toolbox of MATLAB consisting of one hidden layer with four hidden nodes. This optimized architecture was determined using a cross-validation technique by dividing the original data set into three subsets called **training**, **validation** and **test** groups.  After establishing a MLP neural network using crisp input values, the next step was performing sensitivity analysis of the classification performance of the network subject to fluctuations in its input nodes to evaluate network robustness in case of imprecise input information. The first idea was to implement the standard Monte Carlo approach, randomizing the input information and monitoring the average output changes; but this approach had a significant drawback especially when applied to nonlinear neural networks because it is impossible to be certain about mapping all combination of input parameters and distinguishing the worst possible scenario. For this reason a convex model consisting of a series of input intervals was considered in the study using INTLAB toolbox of MATLAB to implement the interval calculations propagating through MLP (Multi-Layer Perceptron) network. The above mentioned research program showed the steps needed to be followed for neural network classifiers in the case of monitoring safety-critical structures under uncertainty. The advantage of the new proposed SHM models in this dissertation, however, is that the uncertainty analysis is *a generic part of the training algorithm itself*.

**Figure 2.6.** The Gnat aircraft with the data acquisition system [19]

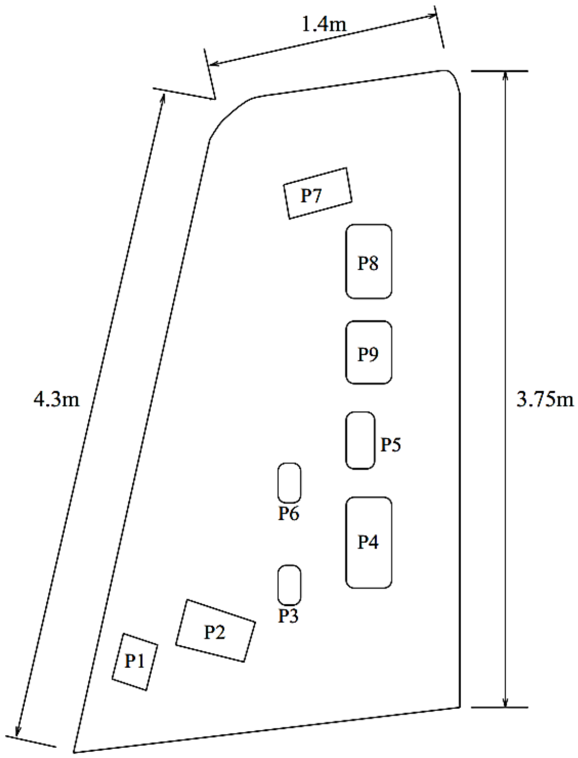


**Figure 2.7.** Schematic of the Gnat wing inspection panels [20]

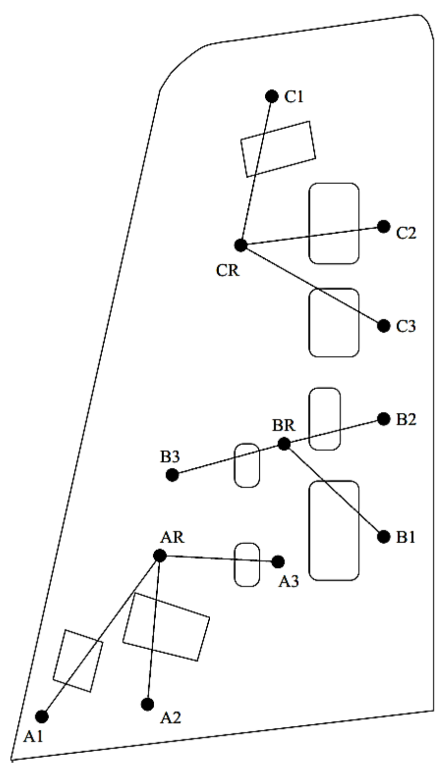


**Figure 2.8.** Schematic of transducer positions during the Gnat wing inspection [20]

## 2.4. Common measurement techniques in SHM

In this section a review on various structural health monitoring measurement techniques applied in the fields of aeronautical and civil engineering is presented. Classification of the techniques is based on the reference [2] as follows:

1) Vibration-based SHM
2) Fiber optic sensors in SHM
3) Piezoelectric transducers in SHM
4) Electrical resistance techniques for SHM

### 2.4.1. Vibration-based SHM

In general, non-destructive measurement techniques can be local or global; for instance, ultrasonic and x-ray NDT techniques are mainly local methods which require prior knowledge about the vulnerable spots in the structure under investigation and the approximate damage location. This reduces the effectiveness of these techniques in dealing with large scale structures such as bridges and airplanes. Vibration-based non-destructive testing is one of the measurement techniques that have been developed to conquer this problem [2].

Vibration-based methods can generally be categorized into local and global techniques. The difference is in the frequency and wavelength of the induced waves. High frequency, short wavelength, vibrations leads to more accurate, highly damping, local identification techniques; while on the other hand, low frequency, long wavelength, vibrations leads to less accurate global vibration of the structure. In global vibration-based techniques there is no need for a prior knowledge about the position of the damage, since the whole structure is tested under vibration. But due to long wavelengths some defects might be lost especially when the dimensions of the defect are less than the corresponding wavelength. In local vibration-based SHM, the wave amplitude of the waves rapidly decays, which requires a denser sensor distribution to cover the whole structure [2].

The basic idea in vibration-based SHM is that presence of damage induces changes in physical/mechanical properties of the structure such as changes in local mass, damping ratio, stiffness, local loading patterns and stress-strain flows, which lead to detectable changes in modal characteristics of the structure such as natural frequencies, mode shapes and modal damping. To generalize, there are eight techniques that are commonly used for damage localization and quantification in SHM [2]:

1) Change of the flexibility matrix
2) Change of the stiffness matrix
3) Strain-energy indicator method
4) Static displacement method
5) Inverse Eigen-sensitivity or study of eigenvalues and eigenvectors
6) Modal force residual method
7) Modal strain-energy based sensitivity method
8) Force vibration and Frequency Response Function (FRF)

Based on the features extracted, the damage identification methods can be categorized as follows [2]:

- Natural-frequency based methods
    - The forward algorithm (more theoretical)
    - The inverse algorithm (more practical)
- Mode-shape based methods
    - Traditional mode shape based methods
    - Mode shape analysis using modern signal processing techniques
- Curvature/strain mode-shape based methods
    - Traditional modal curvature methods

    - Modern signal processing modal curvature methods
    - Modal strain energy based methods
- Methods based on mode-shape combined with natural-frequency
    - Modal flexibility based methods
    - Optimization based methods

The damage identification techniques based on monitoring the frequency change can be applied to localize and quantify damage in controlled environmental conditions. However, it is not reliable for structural health monitoring of complex structures with multiple/severe defects. Most of the basic mode-shape techniques can only roughly localize the damage. In order to precisely localize the defects using mode-shapes, optimization algorithms and signal processing techniques should be implemented. The curvature/strain mode-shape methods, using direct changes in strain/curvature or applying signal processing techniques, are known powerful algorithms for damage localization [22].

In vibration-based structural analysis, the excitation and response are inherently measured in the form of time history; while often it is difficult to extract damage characteristics from the provided time-based measurements directly. A more popular approach in vibration-based SHM is to transform the measured time domain data into frequency domain data using Fourier analyzers, and then the modal space data can be extracted from the transformed frequency domain data. Within the past few decades, great efforts have been put in research related to damage identification in time, frequency, modal domains and wavelet analysis, time and frequency domains [23].

Vibration-based damage identification techniques can be categorized into model-based and signal-based. In the model-based approach a detailed description of the structure, quantitative or qualitative, is available. In the quantitative model-based approach an analytical or numerical model is provided (also called analytical redundancy); while, in qualitative approach, a knowledge-based redundancy is provided. On the other hand, signal-based (also called response-based) diagnosis consists of time, frequency, modal and wavelet domains, which implement the experimental response data measured by the distributed sensors spread over the structure.

Doebling et al. have presented an extensive literature review on vibration-based structural health monitoring up to the year of 1996 [24]. Sohn updated the literature presented by Doebling to cover those research performed up to the year of 2001 [25]. Carden and Fanning, continued on Sohn's paper to cover the literature regarding vibration-based techniques up to the year of 2003 [50]. The latest literature review of vibration-based damage identification methods was done by Fan and Qiao in 2011 [26]. In the latter report, based on a finite element simulation of a beam structure, a comparative study of five extensively used damage identification algorithms (namely; Single Damage Indicator, Generalized Fractal Dimension, Mode Shape Curvature, Gapped Smoothing and Damage Index Method) is provided to assess the effectiveness of each algorithm in different scenarios (single versus multiple damage scenarios under sensor spacing effect).

### 2.4.2. Fiber Optic sensors in SHM

Optical systems are devices into which the object under investigation introduces modifications or modulations in a light beam that passes through the system [27]. The transmitted light is usually modulated by its amplitude, phase, frequencies or polarization state. Optical fiber technology started in the 1970's for communication purposes, but due to advancements in the design and development of optoelectronic components, they have found a variety of applications as high precision sensors in different industries such as oil, civil infrastructures and aeronautical engineering. Figure 2.9 shows the basic components in an optic fiber sensor [27].

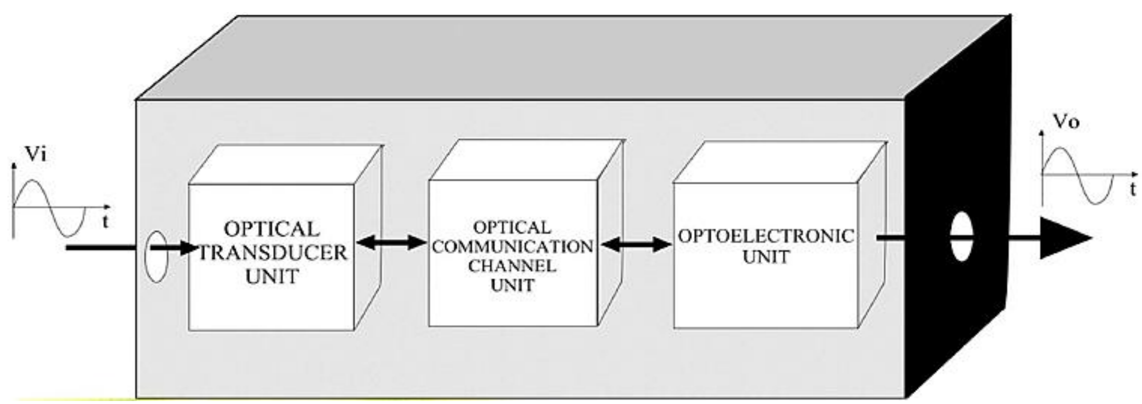


**Figure 2.9.** Main blocks of an optical fiber sensor [27]

Different models can be used to explain the physical phenomena happening to the light transmitted in the fiber optics and its interaction with the surrounding matter; such as [27]:

1. Geometrical optic model; this model merely deals with reflection and refraction based on Fermat principle.
2. Scalar wave model; this model considers reflection, refraction and diffraction and is based on the Huygens equations.
3. Electromagnetic model; this model deals with polarization of light and is based on Maxwell equations.
4. Quantum optics model; this model is the most sophisticated type which is based on Schrodinger equation and deals with the interaction of light and matter (absorption and emission of energy).

Optical Fibers (OFs) are cylindrical waveguides used to propagate light along a structure and are normally made from high purity, low loss optical materials (usually silica) [2]. Most of the interesting advantages of the OFs are contributed to the characteristics of the silica cover which is light weight, dielectric and immunity to electromagnetic interferences, with low losses at optical frequencies (which make measurements, sensing and transmission possible over long ranges such as kilometers along pipe lines). It can also withstand high operating temperatures. In industrial applications optical fibers are protected by a plastic coating and usually several optical fibers are assembled by Kevlar to make robust optical fiber cables which can withstand scratches and rough industrial manipulations [4].

Three different approaches for classifications of fiber optics are presented in the literature. The first approach is based on polarization of light inside the fibers, while the second approach deals with the applications and types of measurement to be monitored, and finally, the third classification is based on the spatial distribution of sensors over the structure and data acquisition methodology [27].

*Classification of fiber optics based on the polarization of light:*

Depending on the polarization state of the light inside the optical fiber, OFs can be classified into two main groups, single and multimode OFs. Eq. 1 calculates the number of discrete solutions, polarization of light which takes place inside the optical fiber depending on the core diameter, $a$, the wavelength, $\lambda$ and the corresponding mode numbers $n_1$ & $n_2$.

$$V = \sqrt{2\,\pi^2 a^2 \frac{n_1^2 - n_2^2}{\lambda^2}}\,. \qquad \text{(Eq. 1)}$$

In single mode optical fibers which have a diameter of less than 10 $\mu m$, $V$<2.4, and therefore only two orthogonal polarizations occur through the fiber. Optical wave attenuation is smaller for single mode OFs compared to multimode OFs. This may be caused by the group dispersion of waves in multimode OFs, which is brought by different modes of travelling at different speeds. The main advantage of multimode OFs is the larger core they have (30 to 100 $\mu m$) which makes the alignment of the fiber and optical source easier.

*Classification of fiber optics based on the application and type of measurement:*

Based on the type of damage and the corresponding variables to be monitored, different types of optical sensors have been developed which are [2]:

1) Intensity based sensors which are usually used as proximity detectors, loading perturbation indicator, hydrogen detection and curing monitoring.

2) Phase-modulated optical fiber sensors or interferometers, which are perhaps the most accurate tools for distance detection. The most common interferometry architectures are Mach-Zender, Michelson (commercially known as SOFO) and Fabry-Perot.

3) Wavelength based sensors or Fiber Bragg Gratings (FBG) which have been the main focus of attention recently because of their characteristics. Namely, FBSs are absolute, interruption immune strain sensors. FBGs are widely used in civil engineering applications.

*Classification of fiber optics based on the spatial distribution of sensors:*

Considering the spatial distribution of the measurement system over a given structure, fiber optic sensors can be classified as point, integrated, quasi distributed or distributed, as follows (Figure 2.10).

1) In Point OFs different channels each one accessing a single point are used.

2) In Integrated OFs a single value is used which integrates all the objective variables.

3) In Quasi-distributed OFs, the desired variable is evaluated at discrete points located along a single fiber.

4) In distributed OFs, the desire variable is measured along a line in space with a given spatial resolution.

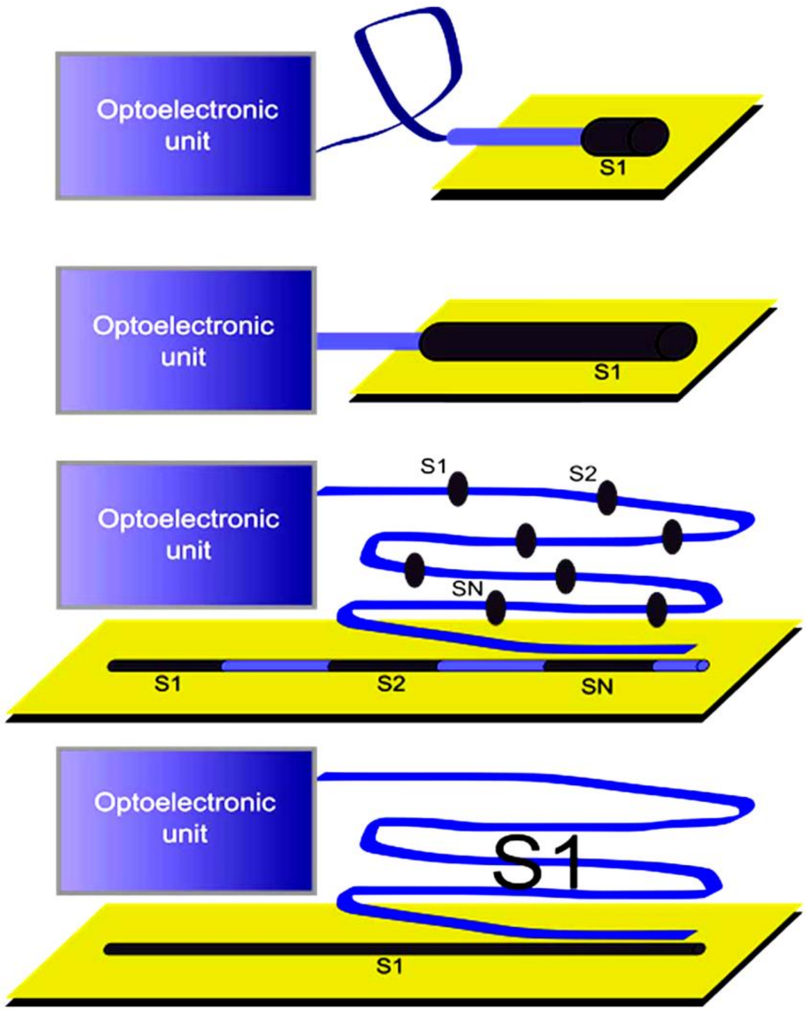


**Figure 2.10.** Different types of Optic Fiber Sensors (OFS) [27]

A wide range of techniques and technologies for high precision optical measurement have been presented in different industrial sectors, but not all of them have stayed successfully active for modern applications. According to López-Higuera & Cobo [27], the most successful technologies in the field of optical fiber sensing suitable to use with structural health monitoring systems are [27]:

1) Long Transducers for Elongation Measurement
2) Transducers Based on Fiber Bragg Grating Technology
3) Fabry–Perot Interferometers
4) Fiber Bend-Based Transducers

One of the most successful technologies in the field of long transducers for elongation measurements is called SOFO (both for static and dynamic applications). [27] This technology consists of two single mode optical fibers, one of them attached to the structure while the other one is loosely placed in the same cable. The static SOFO uses Michelson interferometer to make a precise measurement of the path unbalance, while the dynamic SOFO is based on Mach–Zehnder interferometer.

Fiber Bragg Grating (FBG) technology can be understood as an OF with a periodic refractive index pattern of the core matter such that it diffracts the optical signal at specific wavelengths into core-bounded, cladding or radiation modes. FBGs can be produced as quasi-distributed sensor systems of high resolution, high sensitivity and insensitive to electromagnetic interferences [27].

One of the developed Fabry–Perot Interferometers is called the Extrinsic Fabry–Perot Interferometer (EFPI) which consists of two cleaved optical fibers facing each other with a tiny air gap (a few to tens of micrometers) between them. This mechanism is high sensitive to strain, vibration and pressure and can be used for long-term high precision strain measurements [27].

Micro and Macro bend transducers are optical fibers installed between two plates of saw-shaped edges to enable distributed pressure measurement by measuring deformation and vibration of the surrounding plates. Bend sensors can be produced as point, distributed and quasi-distributed sensors. Commercial micro-bend optical sensors can have the sampling precision and rate of $1\ \mu m$ and $100\ Hz$, respectively, with a gauge length of $10\ cm - 10\ m$) [27].

### 2.4.3. Piezoelectric transducers in SHM

The piezoelectric effect is generation of mechanical loading through local strain upon subjecting the material to electric charge and vice versa. Acoustic Emission (AE) and Acoustic Ultrasonic (AU) are accurate and reliable techniques in non-destructive testing of structures which are able to detect local or global defects long before they lead to catastrophic failure of the part under loading. Traditional AE and AU techniques suffer from problems such as accessibility to the parts, poor signal-to-noise ratio in highly damping materials such as composites. Fortunately, these problems can be overcome by implementing the embedded or bonded piezoelectric transducers to the structure. Piezoelectric methods can be implemented both as passive and active techniques. In the passive approach, the transducer senses the elastic waves propagating the structural layers due to an external source such as impact; while in the active approach, a group of sensors convert the provided electric charge to local strain field which propagates through the structure and the rest of sensors gather the transmitted information. In this section a review of the most common sensing techniques in the field of structural health monitoring based on piezoelectric transducers is provided. The review can be classified in three categories of techniques including Acoustic Emission (AE which is passive), Acoustic Ultrasonic (AU which is active) and Electromechanical Impedance (EMI which is a mixed method) [2].

*Acoustic Emission detectors:*

AE is based on gathering transitory waves of different frequencies and wavelengths that are propagating through the material as surface vibration due to the release of energy caused by the transient local deformations. AE is a passive method and can only detect evolutionary defects, i.e. stable/passive defects are not detectable. Acoustic emission waves are classified as continuous and discrete. In discrete AE, which is usually observed for composite materials, the burst waves are in the shape of damped sinusoid; while in continuous AE, mostly observed in plastic deformation of metallic materials, the transitory waves are so frequent that they result in an apparent increase of the background noise. The real challenge for application of Acoustic Emission transducers in real-time structures under loading, especially in aviation industries, is the background ambient/structural noise caused by airflow, electromagnetic interferences, robbing noise of bolts and fasteners [28-30].

*Acoustic Ultrasonic transducers:*

Acoustic Ultrasonic (AU) transducers can be used to generate Lamb, Bulk, Surface Acoustic Waves (SAW) and Rayleigh waves to study composite and metallic structures of different characteristics and thicknesses. Bulk waves are usually used for thick plates/structures, Rayleigh waves can be used to detect sub-surface flaws in thick plates, and SAWs are suitable for bulk structures. Lamb waves are high frequency, low attenuating waves that can propagate over long distances and therefore a few sensors are needed to be bonded/embedded to cover a wide area of the structure. Lamb waves can be excited by variety of techniques, such as fine-point-contact, wedge, air-coupled, laser-generation and Inter-Digital Transducers (IDTs) and embedded piezoelectric array technique [31]. Lamb waves have two popular modes: symmetric, $S_0$, and anti-symmetric, $A_0$. The symmetric mode is usually used for surface crack detection in metallic structures, while the anti-symmetric mode, because of its sensitivity to delamination, is widely used for composite plates [2].

Three SHM technologies based on ultrasonic piezoelectric sensors are industrially available; e.g., SMART Layer®, Hybrid SMART Layer® and SWISS System [2]:

1) The SMART system, which stands for Stanford Multi-Actuator-Receiver Transduction, was developed by Stanford University. It consists of a piezoelectric network of patches in a dielectric material producing Lamb waves for composite or metallic plates [32].

2) Acellent Technologies Inc. made some modificationw in the original SMART system by including optical fiber sensors as response receivers, while original piezoelectric transducers are acting as actuators. The new industrial system is called Hybrid SMART Layer® [2].

3) The SWISS system consists of a phase array of transducers working in the pulse-echo mode. SAPHIR$^{plus}$ is the name of the phased transducer array hardware and software. The SAPHIR$^{plus}$ software enables the transducers to provide a C-scan of the sample that takes into account the beam divergence of the ultrasonic waves [2].

*Electro-Mechanical Impedance (EMI) transducers:*

In this technique the electrical impedance of the piezo patches is analyzed. There are a few articles describing the implementation of this technique for composite SHM purposes. Pardo de Vera detected artificial cracks in quasi-1D GFRP samples using the EMI technique [33]. Giurgiutiu detected bond breakage in composite panels by analyzing the electromechanical impedance of piezoelectric discs [34]. Bois studied delaminations in quasi-1D carbon-epoxy composites using the EMI transducers [35].

### 2.4.4. Electrical resistance techniques for SHM

In the electrical resistance technique the composite structure itself is used as the transmitter and the receiver and the damage assessment is based on measuring the electrical resistance through the material. This technique can be used for Carbon Fiber Reinforced Polymers and hybrid glass-carbon FRPs. Since carbon fibers are good electrical conductors ($\rho \approx 1.5\ 10–5\ \Omega$ m) in an isolating material of low conductivity ($\rho \approx 1013$ to $1015\ \Omega$ m), the electrical resistance measurement is a valuable criteria to assess the integrity of the structure and defects such as delamination, breakage of fibers, rebounding of fiber and the matrix, transverse cracks for cross plies and fiber failure can be monitored through precise analysis of the output electrical signals. This approach satisfies the most desirable features of a good structural health monitoring system which are avoiding any damage to the structure, easy transmission of data to the central processor and easy access to the inaccessible areas. In this regard, two types of composite architectures can be considered, which are continuous fiber CFRPs (or hybrid glass-carbon FRPs), and randomly distributed carbon fiber composites which may include short fibers and/or carbon nanotubes [2].

Figure 2.11 shows the electrode's location for resistance measurement and Figures 2.12 and 2.13 illustrate longitudinal resistivity versus inverse of length along the measurement path.

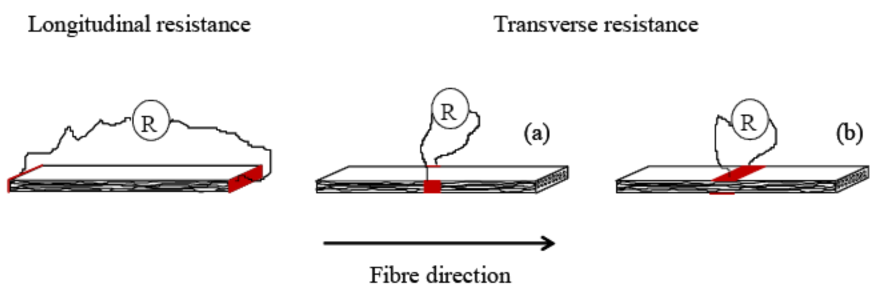


**Figure 2.11.** Location of electrodes for resistance measurement [2]

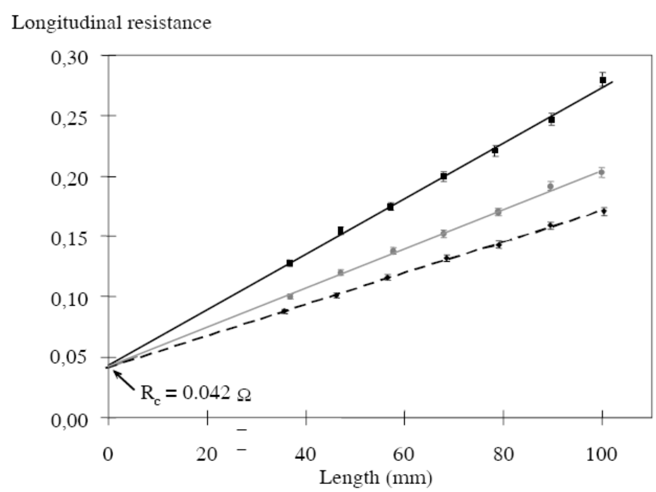


**Figure 2.12.** Longitudinal resistance for $V_f$=0.43 (back-solid), 0.49 (black-dash) and 0.58 (grey-solid) [2]

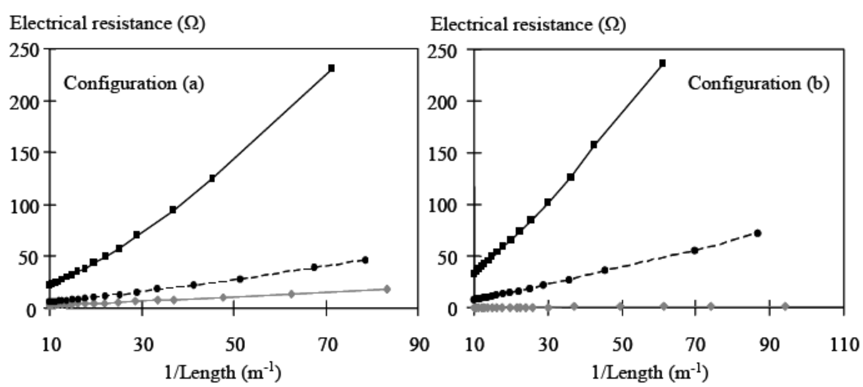


**Figure 2.13.** Transverse resistance for $V_f$=0.43 (back-solid), 0.49 (black-dash) and 0.58 (grey-solid) [2]

The first research regarding implementation of the electrical resistance technique for structural monitoring application through the study of potential distribution was the work by Kemp [36]. In that work a cross ply $[(0/90)_4]_s$ (300 × 300 mm; 2 mm thickness) CFRP laminate was instrumented with a 6×6 array of sensing wires carrying electrical current to the material. The plate was subjected to impact loading from 2J to 8J. Results showed the effectiveness of this technique for higher energy impacts (6J and higher), but no remarkable difference could be distinguished between different damage scenarios [36, 37].

Hou [38] embedded thin copper wires (120 μm diameter isolated by epoxy film) in the cross-ply laminates in fiber directions for both plies. This technique provided good results for the cross-ply composites subjected to low velocity impacts compared to X-ray method.

Angelidis et al. [39] used this method for detecting location and size of low-velocity impact damages in CFRP plate composites with stacking sequences of $[(0/90)_4]_s$ and $[0_2/45_2/90_2/45_2]_s$ using an 11 × 11 set of probes implemented on one face. This research was done in a similar way of the first methodology proposed by Kemp [36], but in more detail.

In general, despite the efforts and researches in order to apply electrical resistance technique for SHM, it appears that it still needs more development for industrial applications.

## 2.5. Strain-based Structural Health Monitoring

It is well recognized that some civil and aeronautical structures, which have been in service for a long time close to or beyond their originally designed life time, are suffering from multi-site and wide-spread defects which may cause catastrophic failures if they are not dealt with properly. Implementing the developed on-ground non-destructive testing can provide an insight into the health status of these structures, but can never guarantee their reliability and safety between inspection time intervals. Therefore, the need for more frequent, ideally online, damage assessment techniques is deemed vital. Monitoring of structures basically consists of two parallel tasks which are load monitoring and structural health monitoring [2]. Operational load monitoring can help to estimate the accumulated fatigue damages and accordingly the residual life time of the parts can be assessed based on the S-N fatigue life evaluation curves. To monitor the loading spectra applied to a structure, a variety of sensors can be implemented such as accelerometers, resistant strain gauges and fiber optics. To monitor the initiation and propagation of damage in structures, a wide range of bonded or embedded sensors have been developed and applied, such as ultrasonic transducers, accelerometer, resistant strain gauges, fiber optics, etc [2]. Resistant strain gauges and fiber optics investigate the stress-strain fields in the structure, looking for abnormalities in the recorded patterns. Resistant strain gauges are the most basic, economic and one of the most common type of sensors used for structural health monitoring systems. Fiber optics, in the form of silica or polymer fibers, are perhaps the most accurate, high precision, multiplexing sensors to date to acquire strain distribution in structures.

Resistant strain gauges are relatively mature, but the main disadvantage for using this type of sensor is the wiring and data transmission which may add to the complexity, maintainability and final cost of the developed SHM system. The first implementation of fiber optics was reported in the 1980s with the OTDR (Optical Time-Domain Reflectometer) technology in telecommunication industry [40]. Since then, fiber optics has been extensively used for load monitoring and damage assessment of critical structures. Over the past decades different types of optical fibers have been studied and a few have successfully found their way to different industrial applications.

Figure 2.14 shows the most applied optical fiber sensors according to [40]. The colorful boxes represent those sensors which have reached an industrial maturity level with commercial products. Table 2.2 summarizes the performance of the mentioned technologies [40]. FBGs are the most common type of optical fibers used in industries. Figure 2.15 illustrates how to classify the FBG interrogation methods based on the measurement frequency ranges.

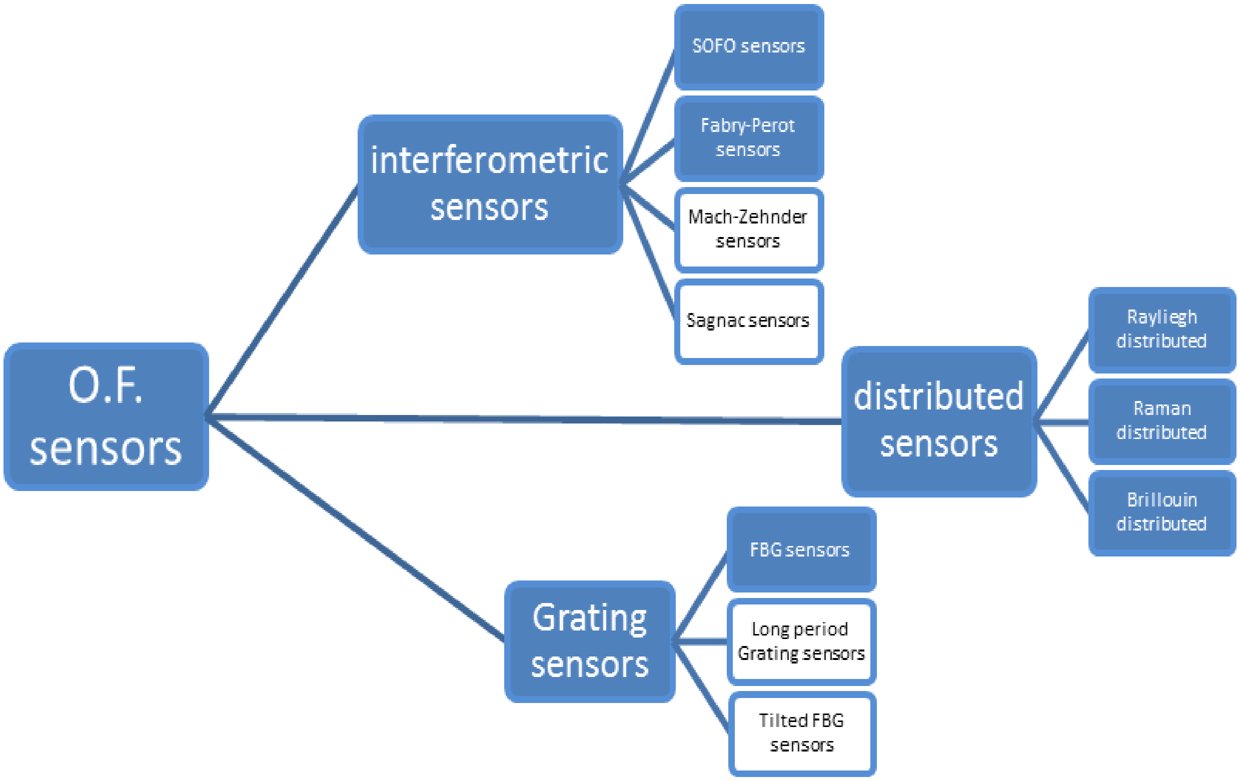


**Figure 2.14.** An overview of the most industrialized OF sensors [40]

**Table 2.2.** Summary of the most applicable OF technologies (source: [40])

| | Fabry-Perot | SOFO | OTDR | ROTDR | BOTDR | FBG |
|---|---|---|---|---|---|---|
| DAQ mode | point | Long range | Distributed | Distributed | Distributed | Semi-distributed |
| Measured parameter | Strain Temperature Pressure Rotation | Strain Force Deformation | Break location Fiber loss | Temperature | Strain Temperature | Strain Temperature Pressure Rotation |
| Multiplexing | Parallel Time division | Parallel Time division | Distributed | Distributed | Distributed | Quasi distributed |
| Number of measurement points in one line | 1 | 1 | Depends on range and resolution | Depends on range and resolution | Depends on range and resolution | 10-15 |
| Typical strain resolution ($\mu$) | 0.15 | 1 | NA | NA | 20 | 1 |
| Typical temperature resolution | 0.1 | NA | NA | 0.1 | 0.2 | 0.1 |
| Capable of detecting large wavelength shift? | Y | N | N | N | N | Y |

| | | | | | | |
|---|---|---|---|---|---|---|
| Spatial resolution | 0.1 | 0.1 | 1-10 | 1 | 1 | 0.1 |
| Capable of fast response detection (for acoustic signals - >100kHz)? | Y | N | N | N | N | Y |
| Advantages | High accuracy<br>High sensitivity | Long range measurement<br>High spatial resolution | Wide applications | Infinite sensing points<br>Fiber integrated | Infinite sensing points<br>Fiber integrated | Accuracy<br>High resolution<br>Inherent WDM encoding<br>Linearity in response |
| Disadvantages | Single point | Low speed (10s) | Detection limitations | Temperature only<br>Expensive | Cross sensitivity | Cross sensitivity |

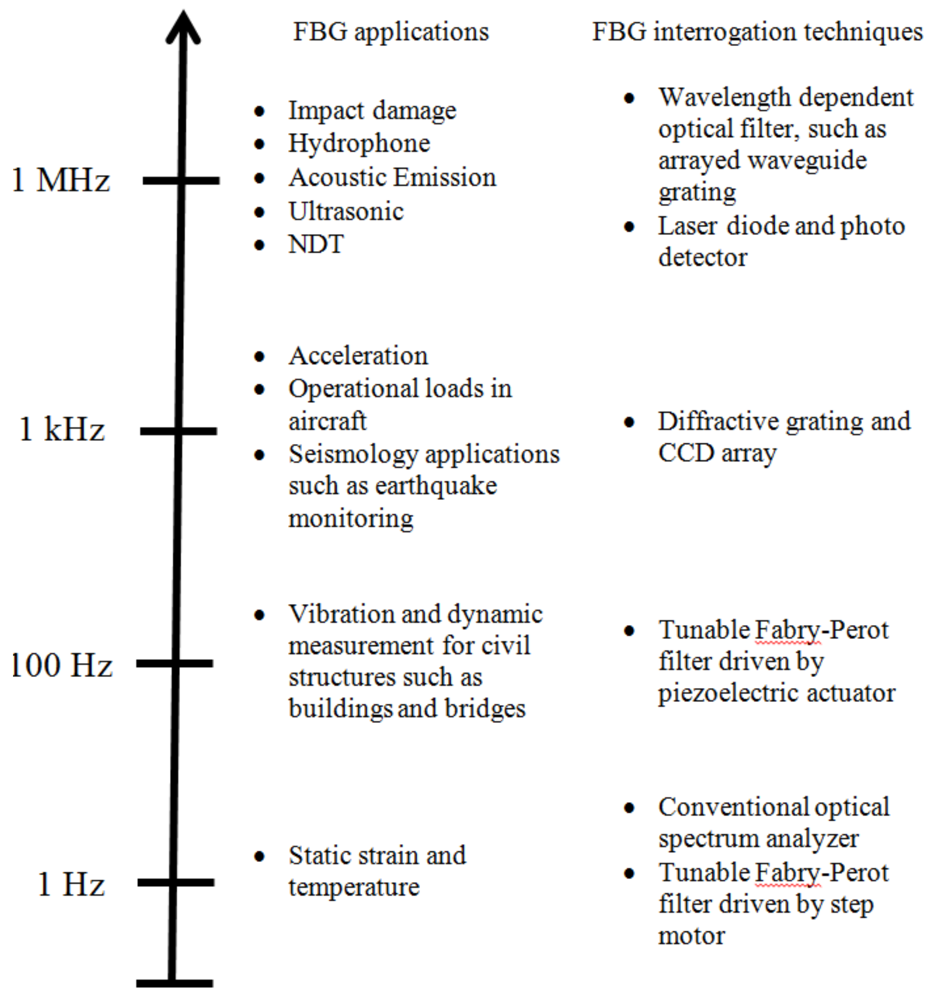


**Figure 2.15.** Classifying the FBG sensors based on the measurement frequency [40]

*The theory behind strain-based SHM systems:*

This section briefly discusses the theory behind strain-based structural health monitoring systems [40]. Then, a literature review on examples of successful industrial strain-based systems will be presented.

In Figure 2.16 a random-shape three-dimensional body with a few defects under tensile loading is illustrated. The array $\gamma$ summarizes the attributes, extend and location, of all the damages, discontinuities and abnormalities in the structure including multi-side damages. After the application of the loading, the body will deform by the displacement vector, $u(x, y, z)$, and therefore the strain tensor field and stress tensor field, $\epsilon(x, y, z)$ and $\sigma(x, y, z)$ respectively, will be generated. Assuming the body is undergoing elastic deformation, the constitutive equation embedding the governing parameters of the problem, $\{\sigma, \epsilon, T, \gamma\}$ can be written as (Eq. 2) [40].

$\sigma = E\ \epsilon$ or $\epsilon = E^{-1}\ \sigma.$ (Eq. 2)

The elastic relation between stress and strain fields help to eliminate one of the parameters from the original set, therefore, leaving $\{\sigma, T, \gamma\}$ as the set of governing parameters. Each of the mentioned parameters can be defined as a function of the other parameters (Eq. 3) [40].

$$\sigma = f(\gamma, T, r). \quad \text{(Eq. 3)}$$

In (Eq. 3) $r$ is the position vector of the point. Assuming the body is under elastic deformation, the total stress-strain field at each point can be described as a linear superposition of the healthy and damaged states (Eq. 4) [40].

$$\sigma(r) = \sigma^{healthy}(r) + \sigma^{perturbation}(r). \quad \text{(Eq. 4)}$$

Where $\sigma$ and $\sigma^{perturbation}$ refer to stress tensors of the damaged structure. Figure 2.17 illustrates the idea of separating the stress-strain field into healthy and damaged states around a two-dimensional crack. Implementing Eq. 3 to Eq. 4, and taking into account that the healthy strain field ($e^{healthy}$) is a function of loading/damage-set parameters, the perturbation strain field can be written as Eq. 5 [40].

$$\epsilon^{perturation} = f(\gamma, T, r) - f_{healthy}(T, r). \quad \text{(Eq. 5)}$$

Now assume $\{p_n\}$ represents a set of points chosen far from the cracked regions such that the perturbations caused by distributed damages have diminished in their vicinity. The array, $e_\infty$, collects the measured strain field tensor components at the $\{p_n\}$ points (Eq. 6) [40].

$$e_\infty = \left\{\epsilon_{ij}(r_n)\right\}. \qquad \text{(Eq. 6)}$$

Assuming there is a unique relationship between far-field strain tensor and the loading components Eq. 5 can be written as Eq. 7 [40].

$$\epsilon^{perturation}(r) = f(\gamma, e_\infty, r) - f_{healthy}(e_\infty, r). \qquad \text{(Eq. 7)}$$

If one repeats the same procedure for a set of points, $\{p_m\}$, in the vicinity of cracks in the structure where the perturbation due to the presence of uncertainty is dominant, the array $e = \left\{\epsilon_{ij}(r_m)\right\}$ can be derived. Since the stress-strain pattern of the healthy structure is assumed to be known ($f_{healthy}$), via finite element method/FEM simulations or experimental measurements, the corresponding values of the unperturbed stress field at the points near damaged areas is known (Eq. 8) [40].

$$e_{healthy} = \left\{\epsilon_{ij_{healthy}}(r_m)\right\} = \left\{f_{healthy}(e_\infty, r_m)\right\}. \qquad \text{(Eq. 8)}$$

Implementing Eq. 5 through Eq. 8 leads to the derivation of the perturbation strain field array ($\epsilon_{perturbation}$) given by Eq. 9 [40].

$$\begin{aligned}\epsilon_{perturbation} &= \left\{\epsilon_{ij_{perturbation}}(r_m)\right\} = \left\{\epsilon_{ij}(r_m) - \epsilon_{ij_{healthy}}(r_m)\right\} \\ &= \epsilon - \left\{f_{healthy}(\epsilon_\infty, r_m)\right\}.\end{aligned} \qquad \text{(Eq. 9)}$$

For convenience, this can be re-written as Eq. 10 [40]:

$$e_{perturbation} = F\ (e, e_\infty). \qquad \text{(Eq. 10)}$$

Assuming a unique relation between $\epsilon_{perturbation}$ and the defect described by the array $\gamma$, Eq. 11 can be derived [40].

$$\epsilon = G(e_p) = G\big(F(e, e_\infty)\big) = H(e, e_\infty). \qquad \text{(Eq. 11)}$$

According to Eq. 11, the physical characteristics of the defects, $\gamma$, can be estimated from the strain measurements at a set of suitably chosen points in the structure. Although the mathematical background of the provided equations is based on the principle of superposition and linear elastic behavior is assumed, the general implementation of this approach is valid if the structure diverts from the pure linear elastic behavior by going into nonlinear or plastic regions.

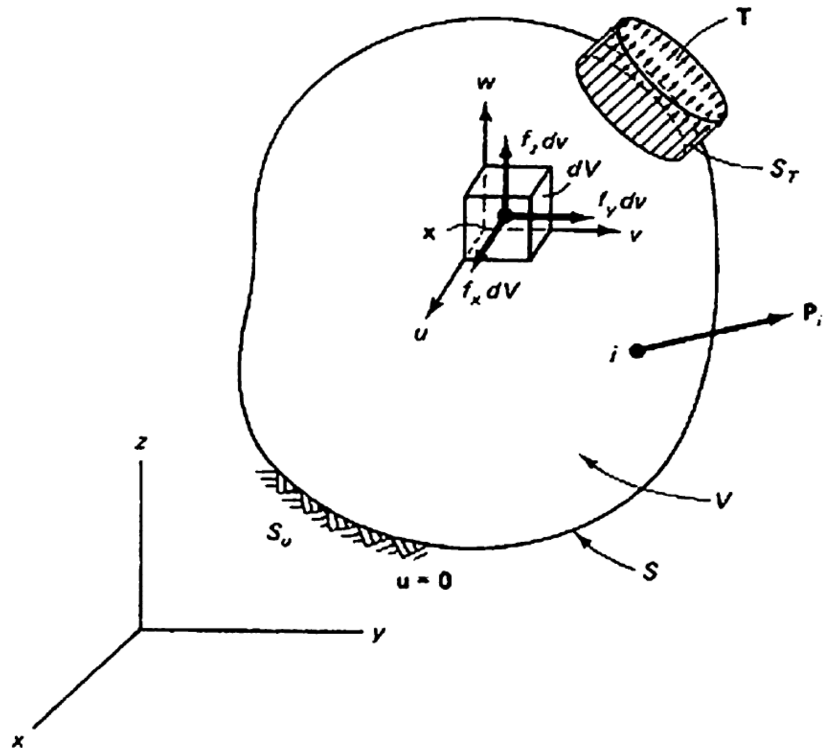


**Figure 2.16.** Schematic 3D loading [40]

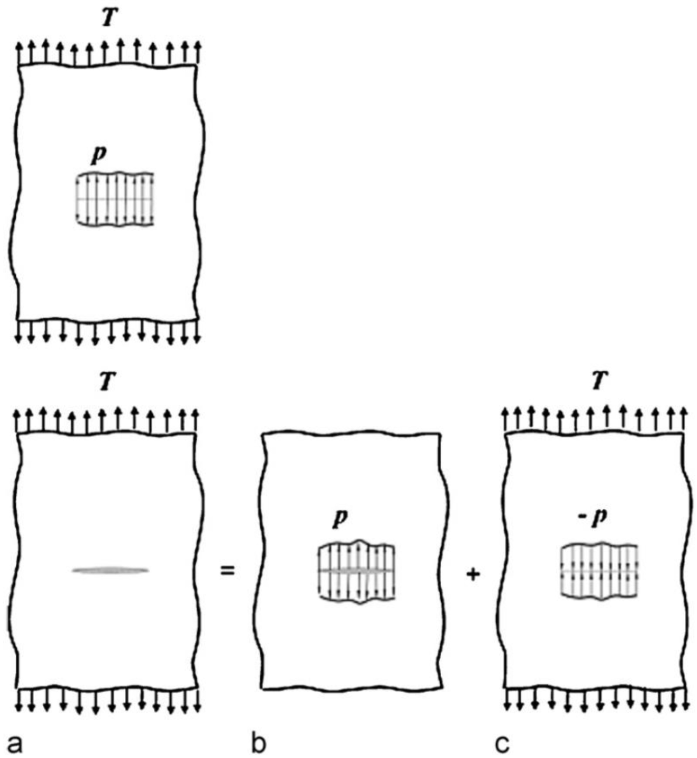


**Figure 2.17.** Separation of loading scenarios [40]

In essence, strain-based SHM systems are based on interrogation of strain field at the desired measurement points across the structure, using previously reviewed resistance strain gauges, OFs (Optical Fibers) or POFs (Polymer Optical Fibers) [40-56].

Gomez et al. [41] discussed the application of a POF system developed to measure the strain distribution in a rudder flap under different bending force scenarios (Figure 2.18). They compared the strain values measured by two adjacent polymer optical fibers, attached to the opposite sides of the structure, with the corresponding values obtained from Brag Grating sensors and strain gauges which offer good stability and repeatability of the proposed measurement system despite the lower cost of POFs compared to FBG sensors.

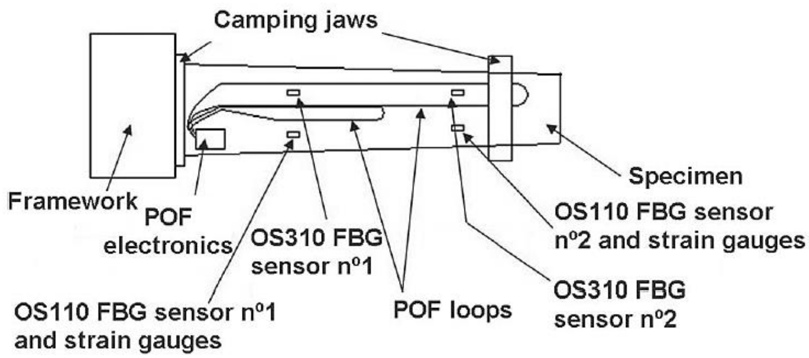


**Figure 2.18.** Schematic top view diagram of the location of the FBG (OS310 & OS110) and strain gauges sensors on the specimen (taken from [41])

Polymer Optical Fibers (POFs) have been the subject of many other researches in different industries, e.g. [42-47]. Polymer optical fibers have the capability to measure high strain values of up to 40% along the fiber direction using the OTDR (Optical Time-Domain Reflectometry) technique. The OTDR has been widely used to investigate the backscatter signal in optical fibers, made of both polymer and silica. POFs are available as Poly-Methyl Meth-Acrylat (PMMA) standard POF and Per-Fluorinated Graded-Index (PFGI) POF. Introduction of the polymer optical fibers greatly fills the industrial demand for high resolution, medium-range techniques with low cost. PMMA standard polymer optical fibers have similarly been reported to be able to measure strain of up to 40% of the fiber along 100m of the measurement length. PFGI fibers can be used to measure strain at lower resolutions up to 500m length.

Liehr et al. [47] used the local pattern of backscatter in the POFs at strained sections to develop a functionalized manufacturing lane of textile composites in order to be able to continuously monitor the structure at the textile reinforcement points. This work was conducted as part of the EU project POLYTECT (Polyfunctional technical textiles against natural hazards) for innovating technical textiles for SHM applications using geotextiles and architectural fabrics/ The final goal was providing textiles which already have the embedded capability for SHM (Figure 2.19) [47]. The two main advantages of the integrated optical strain measurement is that the fiber is already part of the structure and the load transmission is precise, and that the textile provides a protection for the optical fibers embedded in the structure.

**Figure 2.19.** Samples of geotextiles integrated with polymer optical sensors (taken from [91])

Multi-Side Damage (MSD) and Widespread Fatigue Damage (WFD) are two of the main concerns for aircraft structures, especially when the structure is close to or beyond its design life time. Most of the techniques to monitor the state of MSD and WFD are based on damping characteristics, natural frequencies and lamb waves analysis. The major drawback of the aforementioned techniques is their sensitivity to boundary/ambient conditions. Recently researchers have been interested in applying strain-based SHM techniques to monitor MSD and WFD in aeronautical structures [48, 49]. In the study [48], the fatigue cracks around lap joints were investigated using a dense distribution of FBG sensors in and around the vicinity of the cracked region. This technique was found rather insufficient for structures in service because the sensor architecture needs to be properly close to the crack tip which is not the case in real-time applications. Katsikeros studied the MSD in lap joint of aircraft using feed-forward back-propagation neural network [49]. The trained network was able to predict the location of cracks by 0.24mm error on average (0.06 Mean Square Error) which is quite good for the studied sample configuration. The time series strain measurement has been fed into the Fast Fourier Transformation (FFT) for the extraction of the Fourier Descriptors (FDs). In order to speed up the process for training scenario generation, the sub-model FE technique has been used. The main advantages of the proposed system were its accuracy and independency from external perturbations such as ambient noises and environmental variation.

Fatigue analysis of the wing of Hawk Mk.51 fleet of Finnish air force was the subject of a comprehensive study by Koski et al [50]. Structural response of the aircraft due to operational loading is determined by measuring flight parameters. The focus of that study was the milled wing skin which is under combined tension, compression and shear loading. The strain gauges were located on the upper skin of the wing along the front spar which carries the main loading and is the most vulnerable spot for fatigue cracking. The corner radius of the milled wing skin was the host of the majority of fatigue cracks which varied in length from 6 mm to 93 mm for 2,000 to 4,000 flight hours. The flight measurement combined with finite element simulation revealed the multi-axial stress state at the skin, which in turn resulted in applying an equivalent stress analysis. Eventually, the application of strain gauges combined with finite element simulation and mechanics of materials enabled the researchers to fix the fatigue cracks by attaching composite patches to the vulnerable spots.

The transmission of data has been a major difficulty in dealing with resistance based strain gauges, they have always been of interest in structural health monitoring system development because of their ease of installation and low cost. Strain gauges can be divided into two different categories of wired sensors and wireless networks. In the case of wired sensors, the whole sensor architecture is connected together with wires which will add to the weight and complexity of the final SHM system. On the other hand, conventional wireless networks usually suffer from problems in data transmission, because of ambient noise, and power management due to high power consuming adapters. Therefore, there has been a huge demand for designing low power, noise immune wireless networks. One of the main successful projects in this field is the Golden Gate Bridge [51]. However, this project is based on vibration analysis of the bridge components with accelerometers and differs from strain-based systems. Choi et al. [52] designed a sensor board using a MSP430 microcontroller [53] and an amplifier circuit using a low-pass filter designed by Fulford-Jones et al. [54] on a Mica2 mote with an ATMega 128 MCU to minimize the effect of ambient perturbation on low power strain signals. As a result, a low power, ambient immune, GUI based, strain-gauge oriented SHM system has been developed that can be extended to a wide range of structure types [52].

The development of composite joints as co-bonded and co-cured structures in aeronautical engineering has replaced the conventional bolted stiffener metallic structures. The debonding of skin and stiffener in composite structures is an internal defect that may happen due to impact or other in service loadings. In this regard, Kamath et al. [55] conducted several experiments on different types of composite test-boxes with bolted, co-cured and co-bolted skin-stiffener configurations focusing on strain abnormalities measured by FBG and resistance strain gauges under bending of the structure. An artificial neural network was used to learn from the strain profiles provided by different damage configurations. The skin-stiffener debonding was conventionally studied by lamb wave transducers, but since this approach requires a dense sensor distribution over the structure, and also noise filtering is very complex for composite materials, the strain based techniques was employed [55]. The test-boxes were made of prepreg glass fibers and carbon fibers in epoxy resin produced by Hexcel Composites. The composites were used as top and bottom skins, two adjacent center spars and two other spars at the right and left hand sides of the structure (Figure 2.20 shows the test-box with bolted joints). The damage scenarios were simulated by removing bolts or adhesive bonds from the structure. In the bucking failure the bonded joints exhibited higher and more abruptly buckling deformation. The developed strain-based SHM system was eventually able to reliably monitor damage status in co-bonded/cured composite structures.

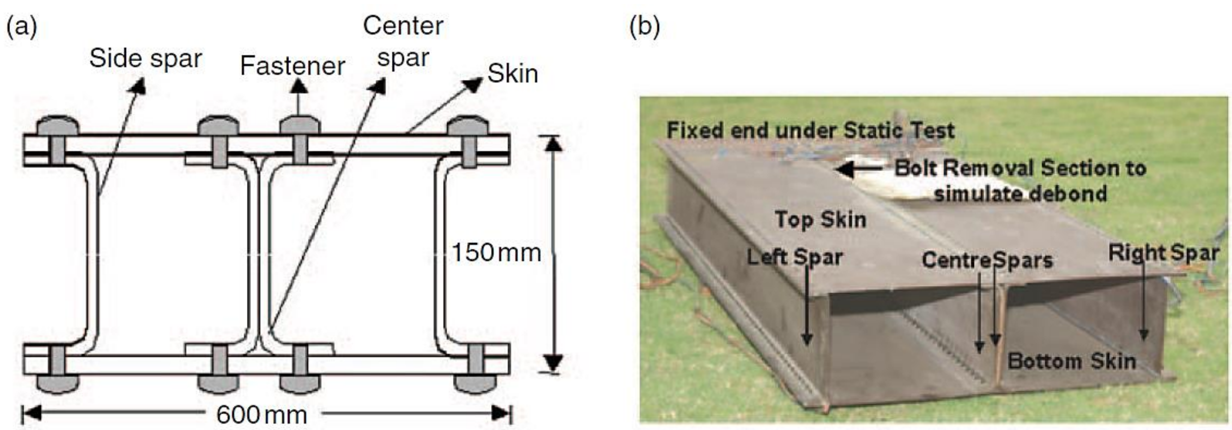


**Figure 2.20.** Schematic (a) and photograph (b) of composite testbox with bolted construction (taken from [55])

Recently more research has been devoted to the development of SHM systems combining acoustic ultrasonic transducers and optical fiber sensors as receivers. In addition to the well-established advantages of optical fiber sensing, their combination with lamb wave transducers can result in high resolution and high speed damage detection. Betz et al. [56] studied the ultrasonic part of the combined PZT-FBG structural health monitoring systems, both theoretically and in an experimental laboratory scale. To generate the lamb wave, piezoelectric transducer disks (PZT) were used in conjunction with a Function Generator and a Power Amplifier to produce a five-cycle sinusoidal tone burst at 150 kHz (Figure 2.21). The Perspex plates were used as samples. Figure 2.22 illustrates different architectures for PZT actuators and FBG sensors. The FBG sensors receive one dominant symmetric-mode lamb wave accompanied by an anti-symmetric signal and a reflection of the dominant mode from the edges. The signal-to-noise ratio analysis showed the same ratio of 26 dB for the PZT transducer and the FBG receiver. The best accuracy of detecting strain for the developed SHM system was 16 nano-strain with the resolution of 40 ftrain $(Hz)^{-1/2}$. The analysis of output signals from the FBG sensor showed its excellent capability for detecting deformation along the fiber direction, while for other forms of deformation the signal is contaminated by anti-symmetric mode and the reflected waves from the edges.

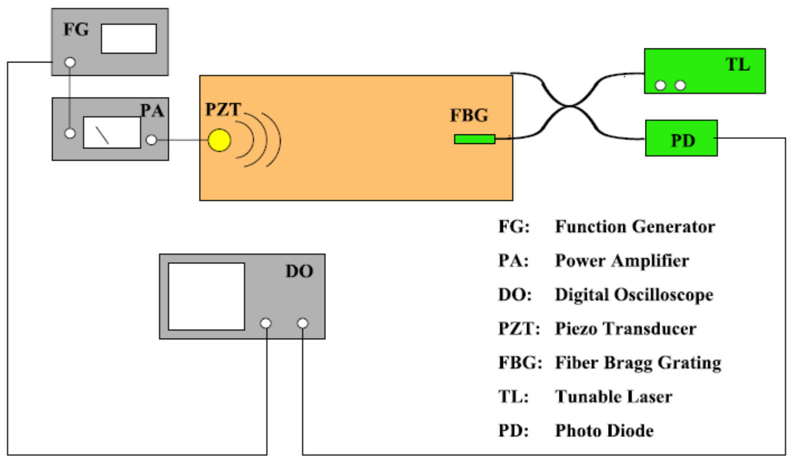


**Figure 2.21.** Measurement set-up for the detection of Lamb waves using a fiber Bragg grating (taken from [56])

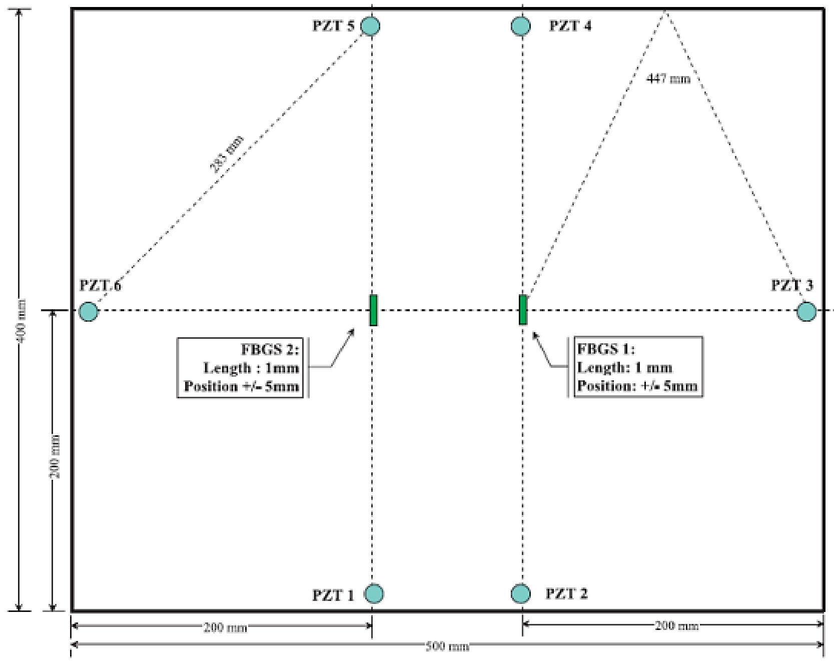


**Figure 2.22.** Dimensions of the Perspex plate and location of transducers and receivers (taken from [56])

As addressed earlier, vibration based damage detection is another well-known structural health monitoring technique based on the analysis of vibration characteristics of the structures such as natural frequencies, modal damping and mode shapes. Most of the vibration based SHM systems are based on capturing the elastic waves produced through deformation/strain under external loading or hammer impacts and measured by accelerometer transducers bonded on the structure. Recently an alternative technique has been studied to pick up the propagating waves in the structure using optical fibers. Cusano et al. [57] studied the application of FBG sensors for experimental modal analysis of an unmanned aircraft wing using the Frequency Response Function (FRF). The wing under study shown in Figure 2.23, is comprised of a sandwich composite consisting of a polystyrene core and two layers of woven glass fabrics (with the density of 80 gr/m$^2$) reinforced with two narrow strips of carbon fabrics at the spar location (with the density of 200 gr/m$^2$). Four fibers of FBG sensors (bandwidth of 0.2 nm centered at 1550 nm) are bonded on the structure at the C-shaped sections. A grid of 29 excitation points, with 5 cm spatial spacing, has been selected (Figure 2.24). Experimental results showed excellent agreement between the conventional accelerometer approach and the new FBG technique in picking up vibration characteristics of the wing by transforming the time-domain measurement using the FRF technique. The new FBG technique is capable of detecting modal properties in different loading scenarios; bending, torsional and normal.

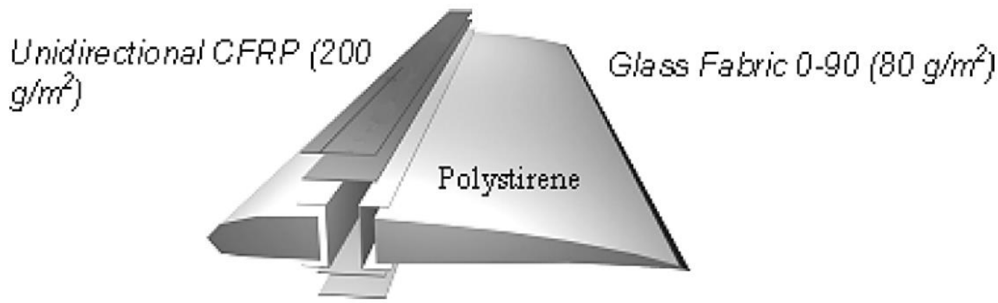


**Figure 2.23.** Schematic of the composite wing (taken from [57])

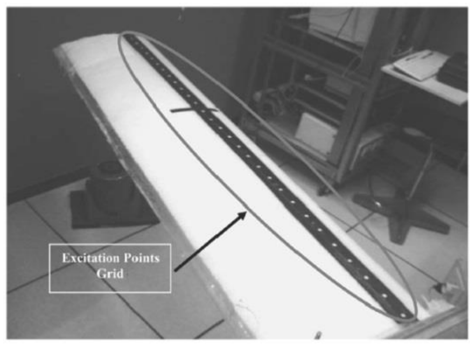


**Figure 2.24.** Excitation points along the spar (taken from [57])

Exploiting wind energy with wind turbines at complex sites in difficult-to-access remote locations require online SHM systems. Slender wind turbines are subjected to large vibration cycles which lead to fatigue cracking. Benedetti et al. [58] reported the project of designing an online strain-based SHM system developed for damage monitoring of the wind turbines located at the Trento Experimental Wind Farm (one three-bladed upwind, one two-bladed downwind, and one three-bladed micro-turbine). At first, the modal characteristics of the turbines were investigated using conventional accelerometer sensors and an instrumented shock hammer. The outcome of this phase was used to modify the finite element simulation of the turbine. The analysis of natural frequencies for turbines has some drawbacks such as insensitivity of lower natural frequencies (which are usually captured in the monitoring process) to the significant damages occurred in the structure and the change of natural frequencies due to change in ambient conditions like ice accretion and asynchronous power generation [58]. In an effort to overcome the aforementioned difficulties for wind turbines, the new SHM systems focused on techniques dealing with local changes in the structural behavior such as change in strain-stress field. Fiber optics played an important role in monitoring of these structures. Based on different loading configurations, and taking into account the possibility of change in wind direction, radial arrangement of FBG sensors around the tower circumference in the proximity of the base joint was considered. The abnormality in strain pattern between adjacent FBG nodes indicated the presence of cracks. In general, the Bayesian theory of probability can be used to identify the abnormal condition. The limiting factor is, however, the number of strain sensors depending on the budget devoted for the structural health monitoring system.

## 2.6. Summary of the literature review

A comprehensive literature review on different techniques for structural health monitoring was presented in this chapter. The uncertainty analysis and interpretation of data is a major concern for most of the SHM systems. In the majority of the developed systems the uncertainty analysis is a post-task after training the machine learning algorithms through neural networks or other algorithms. The sensitivity analysis has been performed in some SHM programs in the past using theories of uncertainty such as classical probability theory, evidence theory and convex models. The novelty of this dissertation is 'combining' the process of initial learning and the uncertainty analysis through the application of the Gaussian Processes. Next chapter represents the methodology for the techniques used in the dissertation, including the Neural Networks (NN), Gaussian Processes (GP) and the Signal-to-Noise (SN) ratio analysis.

# Chapter 3

# Background Theory and Literature Review on Selected Machine Learning Algorithms

## Chapter preview

In this chapter a methodological background is presented on the Artificial Neural Networks (ANNs), Signal-to-Noise (SN) ratio analysis and Gaussian Processes (GPs), which are the main statistical tools used in the subsequent chapters to develop a new robust SHM.

## 3.1. Computational aspects of SHM: Fundamentals

The concept of Structural Health Monitoring is essentially based on a comparison of the data measured over the damaged structure to the same information obtained from the healthy structure subjected to the same loading/testing conditions. The ultimate goal is seeking for abnormalities in the structure's behavior and trying to classify the obtained abnormalities and correlate them to the location and extent of the damage in the in-service structure. The first step of decision-making in this process would relate to data acquisition system which involves the sensor type selection, deciding on the number of sensors to be used, picking the most appropriate locations for installing or embedding the sensors, and defining the data acquisition/ recording/ transferring hardware. In this stage additional inquiries such as the way to improve quality of data (data cleansing), compressing the necessary data in a way that the least amount of memory is required, and how to alleviate undesirable features of the data including variations induced by operational/environmental noises should be dealt with [59].

The concept of Statistical Pattern Recognition (SPR) in SHM applications is mostly relevant to feature extraction/selection and machine learning processes. Feature extraction is the process of seeking for the features in the output signal which are best representing the input parameters and are the most sensitive to the variations induced by damage in the structure. Feature selection is closely related to the condensation of data especially for the cases that collection and analysis of massive data are required during the life time of the structure [59].

Machine learning is the process of simulating the learning ability of humans by using computer algorithms to analyze the input data and gain corresponding (output) knowledge and skills automatically. The purpose of machine learning algorithms is to design computer programs that can effectively find the inherent relations between the inputs and outputs, thus predicting the unknown data (e.g., the presence or absence of a critical crack in the current state of the structure) or judging their characteristics (e.g., the crack length). Generalization of the learning algorithm is of vital importance and requires the ability of the algorithm to predict the structure's response when confronted with input data outside of the training set. The learning theory can be classified into three main categorizes [60]:

1. **Classification**; which means associating the input datasets to class or set labels by defining a set or vector of measured quantities.
2. **Regression**; which means developing continuous mapping functions between a group of input variables and output responses.
3. **Density estimation**; which implies estimating the probability density function obtained from a sample of measured data.

Since Neural Networks are a great means for classification and, they are often applied to condition monitoring or fault diagnosis. Neural networks have been widely used in a variety of Structural Health Monitoring aspects like structural loads and usage predictions and damage diagnosis programs [61-67]. In fact neural networks are the basis of the most of the SHM programs developed to date.

Several articles have been published regarding the implementation of neural network training algorithms to predict stress-strain fields or operational loadings from the measured flight parameters. For instance, Smiths Aerospace, the UK Ministry of Defense and the BAE Systems [61-64] conducted a cooperating program to develop mathematical networks to predict stress-strain fields and monitoring loadings for aeronautical structures, which resulted in excellent correlation between the strain field measured onboard and the predicted field using flight parameters. The difference in cumulative fatigue damage using the predicted strain field and the actual strain distribution measured during 1,000 sorties (15 years of recording) over two wings, the fin and the taileron of the Tornado Combat aircraft, was reported to be 3.6%. Reed and Cole [65] reported the development of neural network based fatigue monitoring programs predicting strain fields from flight parameters for a wide range of critical spots for combat, trainer and commercial aircrafts. Escalonilla et al. [66] developed a parametric-based MLP artificial neural network training system to monitor fatigue damage in the Airbus A330-MRTT (Multi-Rule Tanker Transport) with minimum maintenance cost. The system was later extended to other product family members where real time data measured by flight monitoring sensors were used to generate the mapping functions between flight parameters and strain fields [66]. Levinski implemented Artificial Neural Networks to study the combination of buffet loads on the empennage of an F-18 combat aircraft using wind tunnel pressure data in high angle of attack configuration [67].

Even though Artificial Neural Networks (ANNs) are widely used for SHM, they are a poor tool for (probability) density estimations [68]. To include uncertainties in input and output data, in this research, for the first time, Gaussian Processes (GPs) are used for SHM and the performance of GPs is compared to that of different ANNs. In the following sections a brief discussion regarding the methodological considerations of different types of ANNs and GPs.

## 3.2. Artificial Neural Networks (ANNs)

Artificial Neural Networks (ANNs) are crude electronic models that have been inspired by neural structure of the brain. According to Gurney [69], Artificial Neural Networks "are interconnected assemblies of simple processing elements, units or nodes whose functionality is loosely based on the animal neuron. The processing ability of the network is stored in the inter-unit connection strengths, or weights, obtained by a process of adaption to, or learning from, a set of training patterns". ANNs can be supervised or unsupervised. In an unsupervised learning machine, the training is done using data from only one class. For SHM applications this class is considered to be the healthy status of the structure. Based on the pristine conditions of the structure, the statistical condition of the healthy case (base class) is assessed and once a new set of data becomes available, the SHM process can be investigated as two-class hypothesis testing:

$H_0$: the structure is undamaged → statistically the two classes are similar

$H_1$: the structure is damaged → statistically the two classes are not similar

In supervised learning, training points are provided from experimental/numerical simulations on *both* healthy and unhealthy (already damaged) samples. The ultimate purpose of supervised/unsupervised learning is to establish a functional relation (discrete/continuous) between a set of input variables and output variables using a training package. Figure 3.1 shows the nonlinear model of an artificial neuron. The purpose of learning process is finding the weighting coefficients ($W_{ij}$) and bias coefficients ($b_k$) by an iterative process in a way that the network output is the best approximation for the actual (measured) output.

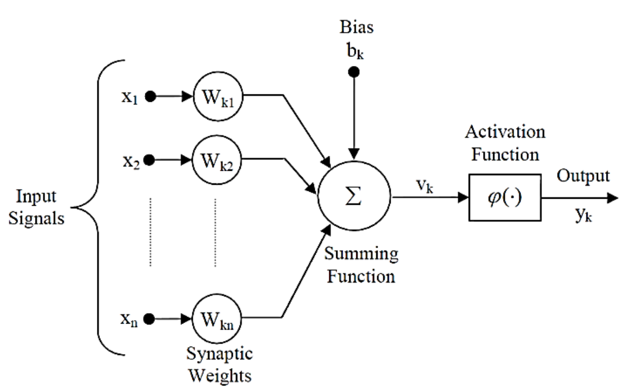


**Figure 3.1.** Simplified model of an Artificial Neural Network [70]

The basic elements of ANNs are the learning rule, the architecture, the learning algorithm and the activation functions. The learning rules deal with the updating process. There are four basic types of learning rules; error-correction, Boltzmann, Hebbian, and competitive. In error correction rule, an error signal based on the difference between the network output and the actual output will be propagated through the weights in order to minimize the root square error function. The perceptron learning network is based on the error correction rule (Figure 3.2) [70].

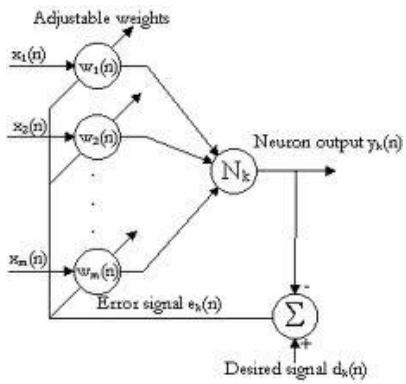


**Figure 3.2.** Error-correction learning rule [70]

In a Boltzmann network, the nodes are divided into two sets of visible and hidden nodes and the objective is to adjust the weight coefficients so that the hidden nodes satisfy a particular desired probability distribution. Boltzmann learning is similar to the error correction rule in that an error signal is used for the training process. But unlike the former learning rule, in Boltzmann learning the difference between the output probability distributions, not the actual difference, is taken into account. The artificial NNs using the Boltzmann learning rule are called the Boltzmann machines (Figure 3.3) [70].

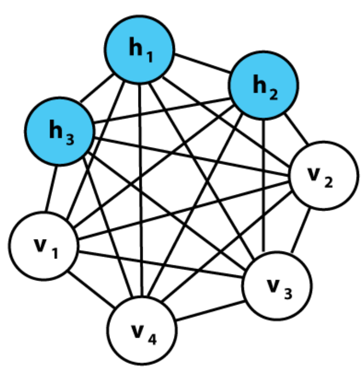


**Figure 3.3.** Boltzmann learning rule [70]

In the Hebbian learning rule, which is a type of unsupervised learning algorithm, the weights are updated based on the actual value of the nodes they are connected to (Figure 3.4)—which is somewhat similar to the concept of 'weighted regression'. The Hebbian learning rule in artificial NNs has been directly derived from the physiological observations. It is strongly suggested by physiological evidence that the Hebbian rule is the type of learning process which happens in the region of the brain known as hippocampus [70]. The neuropsychologist Donald Hebb [70] postulated how biological neurons learn by representing the Hebbian rule: "When an axon of cell A is near enough to excite a cell B and repeatedly or persistently takes part in firing it, some growth process or metabolic change takes place on one or both cells such that A's efficiency as one of the cells firing B, is increased." The original Hebbian rule has the tendency of divergence because the chance of coincidences will build up the connection strength in a way that the weights increase indefinitely. Therefore, the original Hebbian rule is often supplemented by a few modifications, like the one that weakens or eliminates the synapsis if the corresponding neurons on the either side are activated synchronously, or the weights are normalized between 0 and 1(Oja's learning rule) [70].

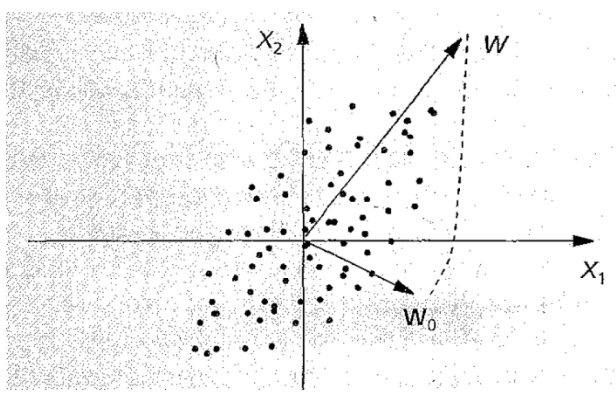


**Figure 3.4.** Hebbian learning rule [70]

In competitive learning rule, which is also a form of unsupervised learning, the output units compete among themselves for activation; the unit with largest (or smallest) net input will be the winner. The effect of competitive learning rule is that the stored weighting pattern in the winning unit will get a little closer to the input pattern in each iteration. Competitive NNs contain one hidden layer which is known as the 'competitive layer'. Every neuron in this layer is described by the vector of weights and calculates the similarity measure; the inverse of the Euclidean distance between the input data and the corresponding weight vector. Competitive neural network is well suited to finding clusters within data. For every input vector, the neurons in the hidden competitive layer compete among themselves to see which one of them has the most similarity to the provided input vector, and then the winner neuron sets its output to 1 while all the others set to 0 (Figure 3.5).

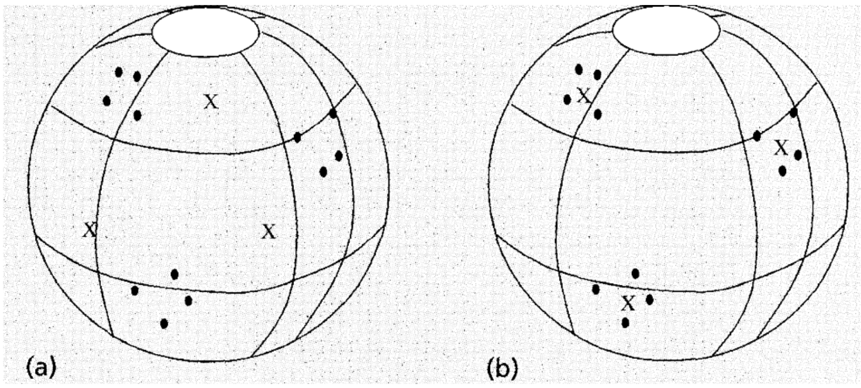


**Figure 3.5.** Competitive learning rule – (a) before learning (b) after learning [70]

Another element of ANNs is the architecture of the network (Figure 3.6). Many ANN architectures may be defined based on the feed-forward and recurrent networks (Figures 3.7 and 3.8). The majority of the published articles regarding development of ANNs for SHM or material characterization purposes have implemented the concept of feed-forward network. There are limited publications describing the application of recurrent networks for NDT testing, SHM and material property characterization of composites.

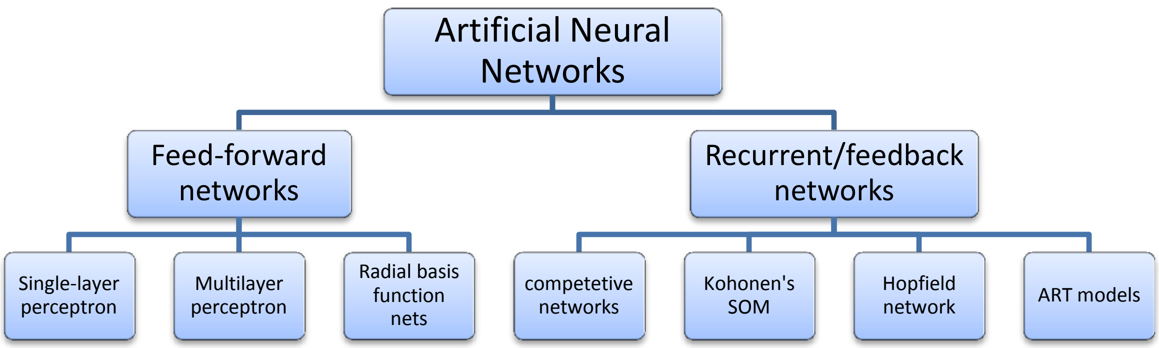


**Figure 3.6.** Different types of Artificial Neural Networks [70]

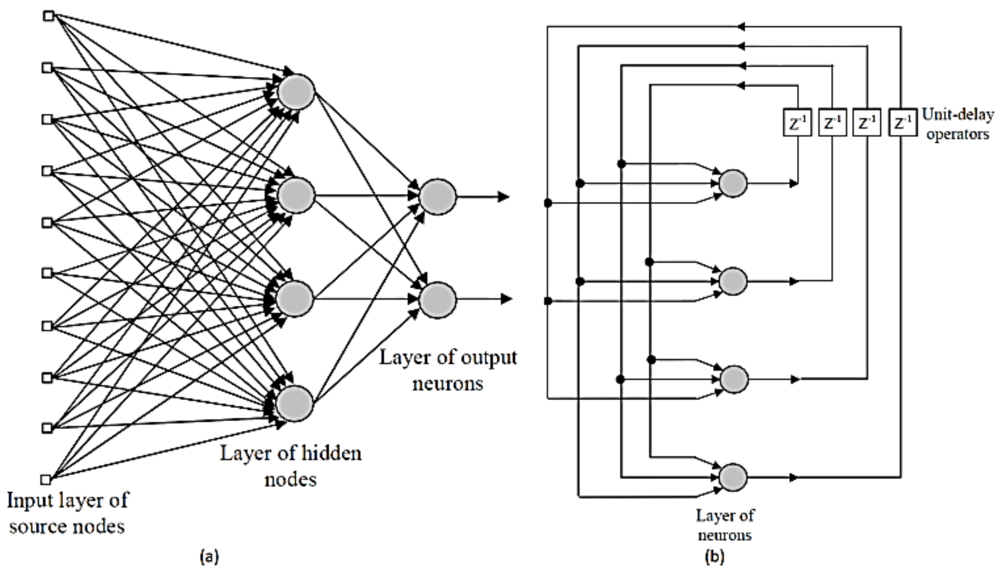


**Figure 3.7.** (a) A feed-forward network (b) recurrent network

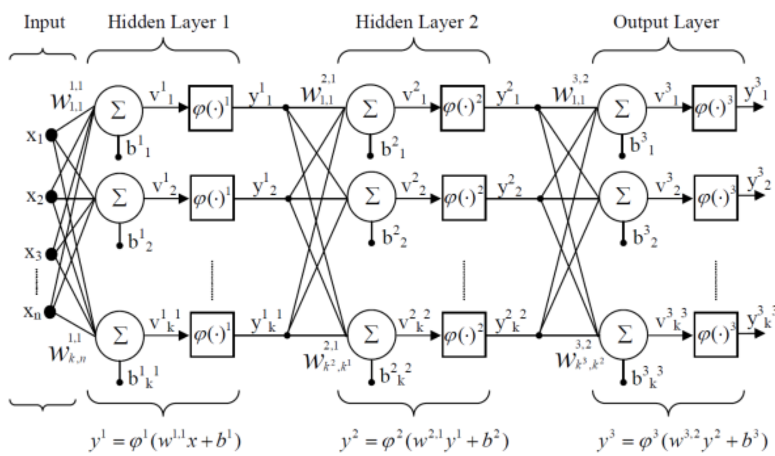


**Figure 3.8** (a). Multilayer perceptron ANN

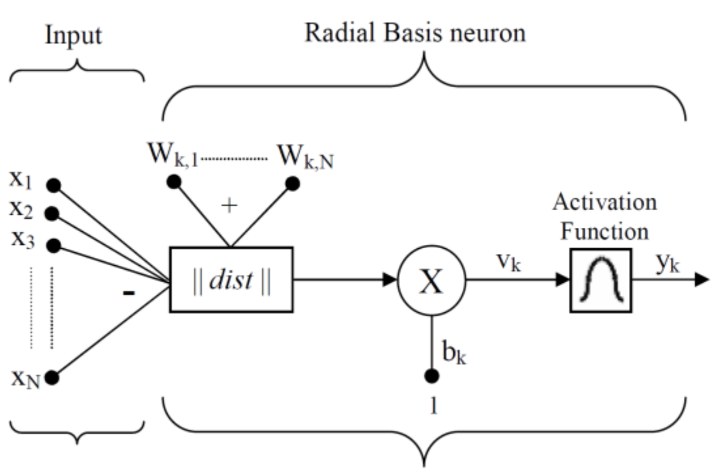


**Figure 3.8** (b). Radial basis function ANN

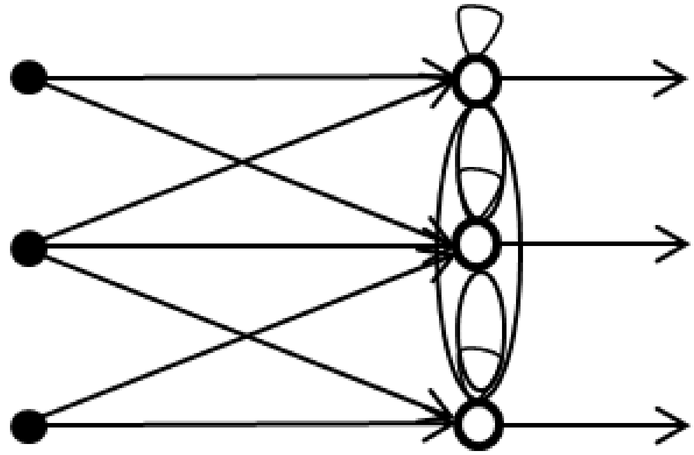

**Figure 3.8** (c). Competitive ANN

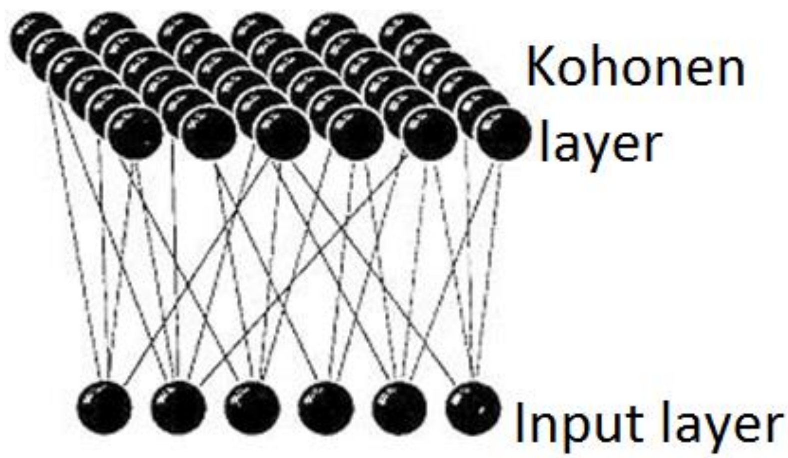


**Figure 3.8** (d). Kohonen ANN

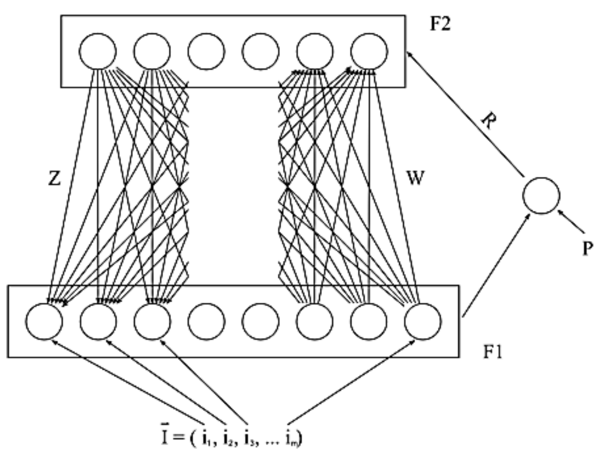


Figure 3.8 (e). ART ANN

**Figure 3.8.** Different ANN architectures (pictures have been taken from internet webpages)

Multi-Layer Perceptron (MLP; Figure 3.8(a)) has been widely used in the artificial neural network algorithms that deal with structural health monitoring or condition monitoring of structures and, because of its wide application in this field, was the subject of part of the current thesis work (Chapter 6). In chapter 6, the conventional MLPs consisting of two to four hidden layers will be used to predict the size and location of delamination in the models subjected to uncertainty of input parameters (such as manufacturing error during lamination of layered composites).

In the field of pattern recognition techniques, the radial basis function nets (Figure 3.8(b)) are artificial neural networks which implement radial basis functions (RBFs) as their activation functions between layers. Radial basis networks usually consist of three layers; one input, one hidden and the output layer. In the basic forms all the neurons in the adjacent layers are connected to each other and the radial function is the Gaussian function applied on the Euclidian distance of the neurons. Given the Gaussian function as the activation function, the RBFs are universal approximators on any subset of $\mathbb{R}$; which means if the RBF is provided with enough neurons in the hidden layer it can approximate any continuous function with arbitrary precision. RBF nets have been used in function approximation, classification (unsupervised learning) and system control [70].

Self-Organizing Maps (SOM; Kohonen – Figure 3.8(d)) are a type of unsupervised artificial networks designed to produce low dimensional representation of high dimensional input data in an unsupervised training algorithm. SOMs use neighborhood functions in order to preserve the topological properties of the input space and they do not use activation function or bias weights. Usually the nodes are arranged in two dimensional grids in the shape of rectangle or hexagon and the network operates in the training and mapping mode. In the training mode, like the competitive learning algorithms, the neurons compete among themselves in order to distinguish different clusters in the input data and in the mapping mode the new input vector is automatically classified [70].

ART artificial neural networks (Figure 3.8(e)) are based on the adaptive resonance theory developed by neuroscientists describing how the brain processes information. ART-1, ART-2, ART-3 and Fuzzy ART are different version of the adaptive resonance theory developed for unsupervised learning [70]. They were basically introduced to overcome the stability-plasticity dilemma which describes the general difficulty for any classification network when it is faced to fitting and 'non-fitting' new knowledge. If the new knowledge fits into the current clusters, the model only requires an adaptation/recalculation of the network weights; but if it doesn't fit into the existing classifiers, it requires modification to the structure of the new classification situation as well as the change in the fitting coefficients. The object identification in ART networks occurs as a result of the interaction between the top nodes, called 'observers', and the bottom nodes, called the 'sensors' (Figure 3.8 (e)). The network forms the memory or prototypes from the top-down expectations which is compared with the actual features of the object provided in the database. If the difference between sensation and expectation does not exceed a threshold parameter, called the 'vigilance parameter', the provided object will be considered a member of the expected cluster. The degree of change in the weights in the training process can be calculated by differential equations (slow ART) or the algebraic binary equations [70]. The slow learning ART provides a continuous calculation of the weight vector and is dependent on the length of time the input vector is presented, while the fast learning ART is more biologically admissible and can be used in time-dependent networks.

Activation functions are used to regulate the output of neurons. The most widely used activation functions are shown in Figure 3.9 and listed below.

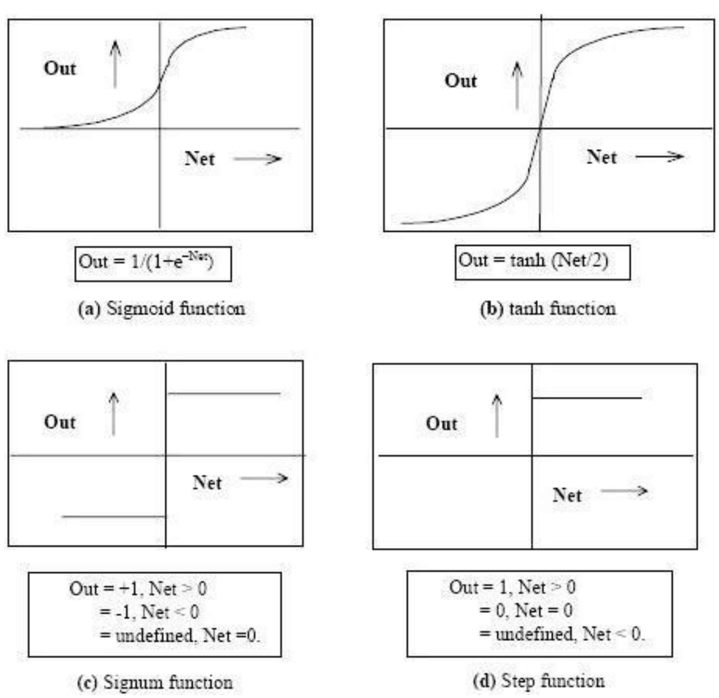


**Figure 3.9.** Activation functions for ANNs [70]

- Log-sigmoid function: $= \frac{1}{\left(1+e^{-input}\right)}$ .
- Tanh function: $output = \tanh\left(\frac{input}{2}\right)$ .
- Hard-limit (or step) function: $output = \begin{cases} 0 & if\ input < 0 \\ 1 & if\ input \geq 0 \end{cases}$ .
- Signum function: $output = \begin{cases} -1 & if\ input < 0 \\ 1 & if\ input \geq 0 \end{cases}$ .
- Linear (or identity) function: $= input$ .

The ultimate objective of all the ANN networks training algorithms is to adjust the synaptic weights in a way that the network is able to best predict unseen data. The following are the most known optimization algorithms used in different ANNs:

➢ *Gradient descent*

This algorithm updates the weights and biases in the opposite direction of the gradient of the error function. Fang et al. [71] used steepest descent algorithms to detect damage in composite laminates and cantilever beams.

➢ *Gradient descent with momentum*

This algorithm is like the gradient descent algorithm with an additional term which is the fraction of the last weight change.

➢ *Resilient back propagation*

This algorithm only considers the sign of the gradient to determine the direction of weight update, and the size of update will be determined by separate update equations. Kesavan et al. [72] used resilient back propagation multi-layer perceptron to detect delamination in composite beam and T-joint structures subjected to static loading using strain distributions.

➢ *Conjugate gradient*

This algorithm searches conjugate directions and usually results in faster convergence speed. On the first iteration search starts in the gradient direction, then a line optimization subroutine determines the optimum distance to move in the specified direction. The final solution will be a conjugate of the current optimal path and the former direction from previous iteration using an update value calculated by Fletcher-Reeves or Polak-Ribiere formulas. Al-Haik et al. [73] used scaled conjugate gradient to train neural networks capable of predicting stress relaxation behavior of carbon fiber composites.

- *Newton and quasi-newton*

  Newton's method approximates a function as a quadratic and then locates the stationary point of the quadratic approximation. Newton's algorithm determines the Hessian matrix of the error surface at the current values of weights and biases. The main drawback of this algorithm is the huge computational costs involved. In quasi-newton mode, which is a variation of Newton's method, an approximation of the Hessian matrix is updated in each iteration as a function of the gradient. Koker [74] used quasi-newton algorithm to find mechanical properties of metal matrix composites.

- *One-step secant*

  This algorithm is a combination of quasi-newton and conjugate gradient. Singh et al. [75] used different kind of algorithms including quasi-newton and one-step secant to fit static response characteristics of transducers to measured data.

Another important aspect in developing an artificial neural network for pattern recognition purposes is the selection of proper number of hidden layers, and the number of hidden neurons in each layer. This can be done through cross validation techniques [74]. In cross validation, the whole initial dataset is divided into two or three categories; training, validation and testing. The training set is used to train a selected neural network with the given hidden neurons and layers, where the objective is to find the best weighting and basis coefficients to minimize the sum of square errors between the actual outputs and the predicted outputs. The validation set acts as a stop criterion during the training process; it means if the performance function is increasing for the specified number of subsequent iterations in the validation set, then the training algorithm can stop. The testing set is the dataset reserved to estimate the performance of the final trained network in case of unseen information. The validation set and the testing set are not part of the training and are kept separate. In the current research, 70% of the original dataset is provided as the training set to the ANN networks and the rest as the testing and validation sets.

In order to determine the best level of model complexity (number of hidden layers, hidden neurons in each layer, and the activation function), the k-fold cross validation technique [75] is used in this research. In the k-fold cross validation technique the total dataset is divided into k number of subsets and for each architecture the training simulation is done k times; each time, k-1 subsets are part of the training while the last subset is kept for testing. This process continues until each one of the k-subsets has been used as the testing once and the model with the minimum average error is chosen to be the optimum network architecture.

Leave-one-out cross validation (LOUCV) is another possible technique [75] in which each time only one observation is assumed to be the testing and the rest are part of the training. This is repeated until each observation in the original dataset has been used once as the testing.

## 3.3. Gaussian Processes

As stated by Rasmussen and Williams [76], "A Gaussian Process is the generalization of the Gaussian probability distribution. Whereas probability distribution describes random variables which are scalars or vectors (for multivariable distributions), a stochastic process governs the properties of the functions". Gaussian processes (GPS) are powerful mathematical tools in analyzing and generating input-output mapping for supervised continuous and discrete networks. Supervised mapping is known as regression (also known as GPR; Gaussian Process Regression), while discrete mapping is called classification (also known as GPC; Gaussian Process Classification). GPC can be considered as a special case of GPR when the continuous output has been reduced onto a desired interval (depending on the number of class labels) using sigmoid functions applied on the latent function (describing the likelihood of one class versus the other encompassing the input data). For instance, in the case of two class-classification, the continuous output can be mapped onto [0, 1] interval using log-sigmoid function representing the probability of data points for belonging to the distinguished classes.

For illustration purposes, let's consider a simple one-dimensional (1D) regression problem which is mapping x-values to the corresponding f(x) outputs. Figure 3.10 shows a few sample prior smooth functions plotted in the specified input region. These functions represent our prior understanding of the current regression problem; in other words, the prior functions represent our beliefs of the kind of function/behavior we expect to observe before knowing any actual data from the system. In the absence of contrary information, it is usually assumed that the mean of the infinite set of prior functions is zero over the entire x-values or each x-value. The mean of the few random prior functions in Figure 3.10 is not zero, however, for every x value in the input interval because the illustrated functions are a specific random set of the infinite possible prior functions. The shaded region in Figure 3.10 illustrates twice the standard deviation. In Figure 3.10 it is assumed that the standard deviation does not depend on the input value, like the constant covariant function.

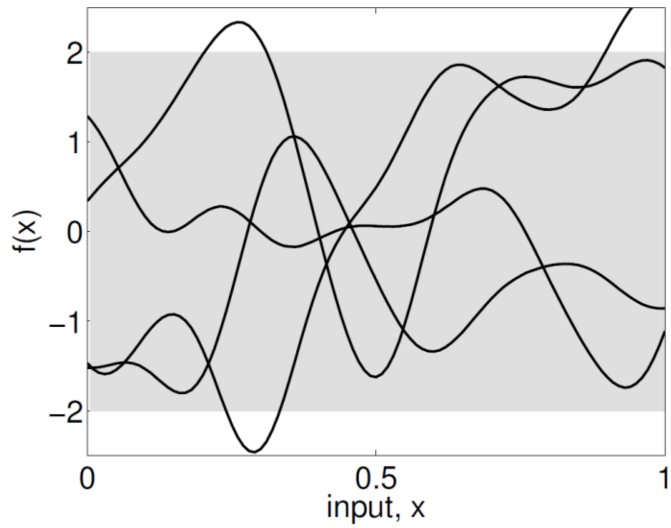


**Figure 3.10.** Schematic of sample prior functions during the GP process (source: [76])

Now assume that two datasets are provided as A($x_1$,$y_1$) and B($x_2$,$y_2$) and we wish to keep the functions that pass through these points by giving higher weighting to those functions that merely pass close to the given data points (Figure 3.11). The combination of priors (Figure 3.10) and data leads to the posterior (Figure 3.11) which provides the Gaussian estimation of the output response. An important aspect in GP regression is that since we are not fitting any particular/explicit model to the problem, we do not need to worry about model selection (unlike the case of standard regression and trying to fit a good model to a highly nonlinear data).

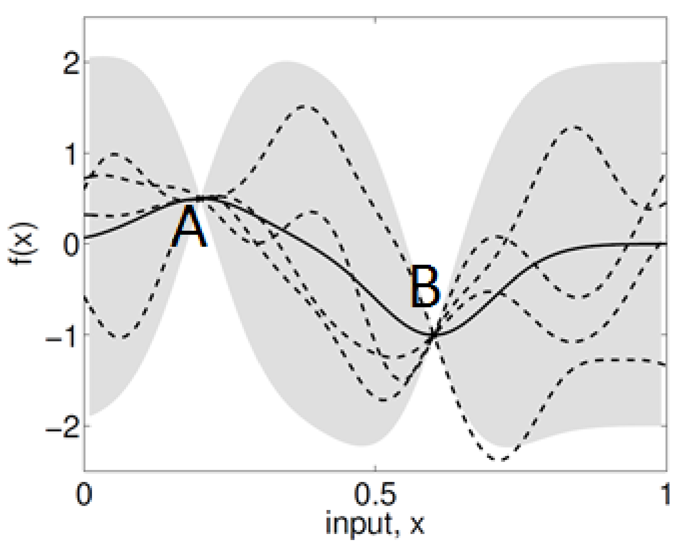


**Figure 3.11.** Posterior functions using data points A & B (adapted from [76])

The specification of the prior function is important as its characteristics are directly reflected in the output function. Many properties of the prior functions in a GP algorithm, like smoothness and being stationary (means the function variance is similar for all pair of points with the same distance; or in other worlds, it is invariant with respect to translations in the input space), are induced by the choice of covariance function of the Gaussian process. For example assume that for a specific application our prior about the output is that it varies so rapidly, therefore a covariance function with a shorter characteristic length seems more suitable. The learning process in a GP algorithm consists of finding a suitable covariance function and estimating the best properties for it; such as the function's coefficients and length scale. There are many covariant functions suggested in the literature [76], but only a few has been practically used in statistical problems. Table 3.1 shows the most frequently applicable covariance functions in GP processes.

**Table 3.1.** Different Covariance functions [76]

| Name | Characteristic | Covariance function |
|---|---|---|
| **Zero** | Mean vanishes always | $k(x,x') = 0$ |
| **Noise** | Additive measurement noise | $k(x,x') = \sigma_f^2\ \delta(x - x')$ |
| **Constant** | Covariance is always a constant | $k(x,x') = \sigma_f^2$ |
| **Linear** | Linear covariance function | $k(x,x') = x^T x'$ |
| **Linear ARD** | Linear with diagonal weighting | $k(x,x') = x^T\ \Gamma^{-2}\ x'$ |
| **Linear One** | Linear with bias | $k(x,x') = \dfrac{(x^T x' + I)}{l^2}$ |
| **Polynomial** | Polynomial covariance function | $k(x,x') = \sigma_f^2\ (x^T x' + C)^d$ |
| **SE ARD** | Full Squared Exponential (SE) | $k(x,x') = \sigma_f^2 \exp\left(-\frac{1}{2}\ (x - x')^T\ \Gamma^{-2}\ (x - x')\right)$ |
| **SE iso** | Isotropic Squared Exponential (SE) | $k(x,x') = \sigma_f^2 \exp\left(-\frac{1}{2l^2}\ (x - x')^T\ (x - x')\right)$ |
| **SE uniform** | Uniform Squared Exponential (SE) | $k(x,x') = \sigma_f^2 \exp\left(-\frac{1}{2l^2} x^T x'\right)$ |
| **RQ ARD** | Full Rational Quadratic (RQ) | $k(x,x') = \sigma_f^2\ \left(I + \frac{1}{2\alpha}\ (x - x')^T \Gamma^{-2} (x - x')\right)^{-\alpha}$ |
| **RQ iso** | Isotropic Rational Quadratic (RQ) | $k(x,x') = \sigma_f^2\ \left(I + \frac{1}{2\alpha l^2}\ (x - x')^T (x - x')\right)^{-\alpha}$ |
| **Matern iso** | Isotropic Matern covariance function<br>$f_d$ is the Matern function of degree $d$<br>$d$ can be 1, 3 or 5 | $k(x,x') = \sigma_f^2\ \frac{2^{1-v}}{\Gamma(v)} \left(\frac{\sqrt{2v}r}{l}\right)^v\ K_v \left(\frac{\sqrt{2v}r}{l}\right)$<br>$v: positive\ parameter$<br>$K_v: Bessel function; K_v is\ the\ answer\ of:$<br>$x^2 \frac{d^2y}{dx^2} + x \frac{dy}{dx} + (x^2 - v^2)y = 0$<br>$\Gamma(v): the\ gamma\ function$ |

| | | |
|---|---|---|
| | | $\Gamma(v) = \int_0^\infty x^{v-1} e^{-x} dx$ <br> $if\ v = p + \frac{1}{2}\ (p\ is\ integer)\ then:$ <br> $k(x,x') = \sigma_f^2\ f_d(r_d) \exp(-r_d)\ ;$ <br> $r_d = \sqrt{\frac{d}{l^2}\ (x-x')^T (x-x')}$ <br> $f_1(t) = 1;\ \ f_3(t) = 1 + t;\ \ f_5(t) = 1 + t + \frac{t^2}{3}$ |
| **NN one** | Neural Network Covariance function <br> $g(x) = 1 + x^T \Gamma^{-2} x$ | $k(x,x') = \sigma_f^2 \sin^{-1}\left(\frac{x^T \Gamma^{-2} x'}{\sqrt{g(x) g(x')}}\right)$ |
| **Periodic** | Periodic covariance function | $k(x,x') = \sigma_f^2 \exp\left(-\frac{2}{l^2} \sin^2\left(\frac{\omega}{2\pi}\ (x-x')\right)\right)$ |
| **PP iso** | Isotropic Piecewise Polynomial (PP) <br> Polynomial $f_v(r)$ | $k(x,x') = \sigma_f^2 \max(0\ , 1-r)\ \times f_v(r)$ <br> $r = \frac{\lVert x-x' \rVert}{l}$ |

In Table 3.1, the following terminologies have been used:

- ‘iso’ stands for isotropic
- ‘ARD’ stands for Automatic Relevance Determination
- ‘one’ means that the distance measurement parameterization has been done using one single parameter.

The SE (Squared Exponential) isotropic function (Table 3.1) is perhaps the most widely used kernel in the field of machine learning. This function is indefinitely differentiable which makes the corresponding GP to have mean square derivatives of all orders. Some statisticians [79] argue that such strong smoothness is unrealistic for modeling many physical processes, and therefore, the Matern covariance functions are recommended. In the Matern class of covariance functions the process is $v$ times differentiable and if $v$ is tending to infinity the Matern turns out to be the Squared Exponential covariance function. The Matern covariance function becomes very simple when $v$ is half integer; i.e. $v = p+1/2$ ($p$ is a positive integer). In this case Matern can be expressed as the product of a polynomial of order $p$ and an exponential (Table 3.1). The most common cases of this category happen when $p = 1$ or 2 ($v = 3/2$ or $5/2$) [76]. The special case obtained by setting $v$ to ½ in the Matern class of functions leads to the exponential covariance function $k(x,x') \propto \exp\left(-\frac{x-x'}{l}\right)$. In a one-dimensional space, this covariance function is called the Ornstein-Uhlenbeck function of the Ornstein-Uhlenbeck (OU) process [76].

### 3.3.1. Step by step implementation of the GP algorithm for a simple 1-D problem

In the present section the implementation of the GP algorithm for regression of a single input-output system is briefly described. Figure 3.12 provides an example of a prediction problem showing a noisy distribution of the output variable for specified inputs. The estimate for the output at the desired input (say the last point) needs to include both the mean and variance values.

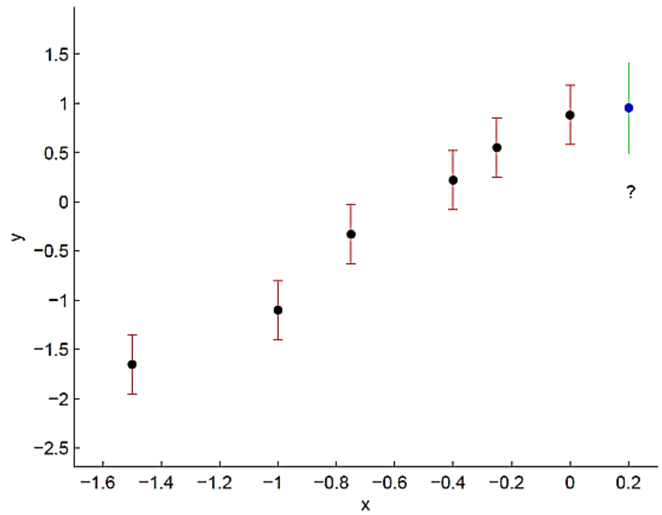


**Figure 3.12.** Example of a GP prediction problem: mean and variance of the output at the desired input are required.

Assume $\{x\}$ and $\{y\}$ indicate input and output vectors of $n$ dimension. The Square Exponential (SE) covariance function connecting two arbitrary data points $x$ and $x'$ is defined by Eq. 1 [76]:

$$k(x,x') = \sigma_f^2 \exp\left[\frac{-(x-x')^2}{2\,l^2}\right]. \qquad \text{(Eq. 1)}$$

$\sigma_f$ indicates the maximum allowable covariance. The covariance function is maximum for adjacent nodes and decreases as the distance between nodes increases. The length parameter at the denominator of the exponential power determines the region of impact of each node on others; i.e. for inputs with more distance between them compared to the length parameter, the interaction is negligible. Some researchers [76] add an extra term to (Eq. 1) to take the impact of noisy data into account as shown in (Eq. 2) [76].

$$k(x,x') = \sigma_f^2 \exp\left[\frac{-(x-x')^2}{2\,l^2}\right] + \sigma_n^2\,\delta(x,x'). \qquad \text{(Eq. 2)}$$

Where $\delta(x,x')$ is the Kronecker delta function and $\sigma_n$ is the noise level. To prepare for GP, the following $K$-variables (matrix, vector and scalar) should be computed (Eq. 3) where $x_*$ is the input value for which the output is desired [76].

$$\begin{aligned} K &= \begin{bmatrix} k(x_1,x_2) & \cdots & k(x_1,x_n) \\ \vdots & \ddots & \vdots \\ k(x_n,x_1) & \cdots & k(x_n,x_n) \end{bmatrix}. \\ K_* &= [k(x_*,x_1) \quad \cdots \quad k(x_*,x_n)]. \\ K_{**} &= k(x_*,x_*) = \sigma_f^2 + \sigma_n^2. \end{aligned} \qquad \text{(Eq. 3)}$$

Assuming a multivariable Gaussian distribution, the best estimate for output average $\overline{y_*}$ and the corresponding variance will be provided by (Eq. 4) [76] (here for simplicity it is assumed $\sigma_n \sim 0$; the more general solution will be presented later in the same section: Eq. 32) [76].

$$\begin{aligned} \overline{y_*} &= K_* K^{-1}\,y. \\ var\,(y\,*) &= K_{**} - K_* K^{-1} K_*^T. \end{aligned} \qquad \text{(Eq. 4)}$$

The vector $\theta = \{l, \sigma_f, \sigma_n\}$ contains the GP algorithm parameters. The reliability of the GP and the output values depends on the right choice of $\theta$. According to the Bayesian theorem [76], the best choice for $\theta$ occurs when the following parameter is maximized [76].

$$\left[-\frac{1}{2}\,y^T K^{-1} y - \frac{1}{2}\log|K| - \frac{n}{2}\log 2\,\pi\right]. \qquad \text{(Eq. 5)}$$

Equation (5) consists of three terms: the 1st term represents the data-fit measurement parameter; the 2nd term is the complexity or penalty term; and the last term is constant/independent of the data values, and hence not important for maximization. An important concern when seeking for an optimum $\theta$ is that the function in (Eq. 5) is not convex and local maxima points should be avoided [76, 77].

As stated earlier, the appropriate selection of the variance function is vital when dealing with different noise patterns. In practice, however, there is no limit on the selected complexity of the covariance function, provided that the resulting matrix is invertible. For instance, if the noise pattern in the input data is similar to Figure 3.13, then (Eq. 6) may be employed as an extended covariance function to represent both long term trends and local fluctuations [76].

$$k(x,x') = \sigma_{f_1}^2 \exp\left[\frac{-(x-x')^2}{2\,l_1^2}\right] + \sigma_{f_2}^2 \exp\left[\frac{-(x-x')^2}{2\,l_2^2}\right] + \sigma_n^2\,\delta(x,x'). \qquad \text{(Eq. 6)}$$

The first term in (Eq. 6) models the local vicissitudes of the output, while the second term represents the long term trend.

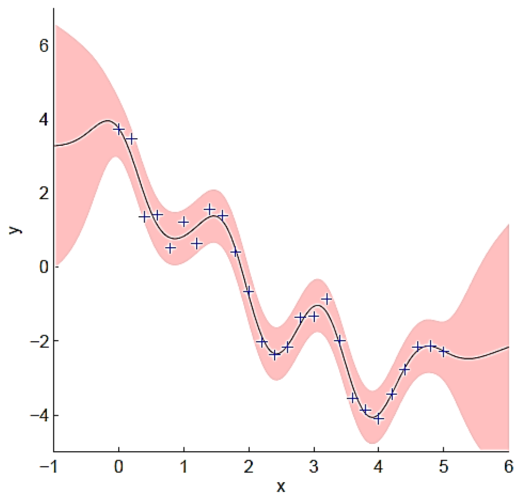


**Figure 3.13.** GP regression of ‘y’ values for short–term and long–term dynamics (taken from [76])

### 3.3.2. Step by step implementation of the GP algorithm for the general case

There are many ways to interpret the GP regression algorithm in a general case [76]. One can think of a function-space view and one a weight-space view. In the function space view, for a case of one-dimensional space, the GP is defined as a distribution over multiple random functions and the interference occurs in the space of functions. Function-space approach to a case of general GP is harder to comprehend, therefore, at first let us review the weight-space view.

Assume that a training set of $n$ observations, $D$ is provided as $D = \{(\boldsymbol{x}_i, y_i),\ i=1..n\}$ where $\boldsymbol{x}$ denotes an input vector and $y$ denotes the corresponding output value (here we assume to be scalar but it can be a vector of different output variables in general). The column vectors of all inputs are aggregated in the $D$ by $n$ design matrix $\boldsymbol{X}$ and the targets are collected in vector $\mathbf{y}$. The standard linear model is written as [76]:

$$f(x) = x^T\, W, \quad y = f(x) + \epsilon. \qquad \text{(Eq. 7)}$$

In Eq. 7 $W$ is the unknown weight vector, $f(x)$ is the linear model and $y$ is the observed output value. We assume the noise to follow a Gaussian pattern which can be written [76]:

$$\epsilon = N(0, \sigma_n^2). \qquad \text{(Eq. 8)}$$

Considering the Gaussian distribution of the input and noise functions, the likelihood/ probability density of the observations given the hyper-parameters is given by Eq. 9 [76].

$$p(y|X,w) = \prod_{i=1}^{n} p(y_i|x_i,w) \ = \ \prod_{i=1}^{n} \frac{1}{\sqrt{2\pi\sigma_n}} \exp\left(-\frac{(y_i - x_i^T w)^2}{2\sigma_n^2}\right).$$
$$p(y|X,w) = \frac{1}{(2\,\pi\,\sigma_n^2)^{\frac{n}{2}}} \exp\left(-\frac{1}{2\sigma_n^2}\ |\boldsymbol{y} - X^T\boldsymbol{w}|^2\right) = N(X^T\boldsymbol{w}, \sigma_n^2\boldsymbol{I}). \qquad \text{(Eq. 9)}$$

In the Gaussian process a prior over the parameters needs to be specified which can express our beliefs about the problem before any observed data is provided to the algorithm. Generally, a zero-mean Gaussian prior distribution with $\Sigma_p$ as the covariance matrix for the weights is assumed as in Eq. 10 [76].

$$\boldsymbol{w} = N(\boldsymbol{0}, \Sigma_P). \qquad \text{(Eq. 10)}$$

Inference in the Gaussian process is based on the posterior distribution over the weights, which is computed by the Bayes' rule [39]:

$$posterior = \frac{likelihood\ \times\ prior}{marginal\ likelihood}.$$
$$p(\boldsymbol{w}|\boldsymbol{y},X) = \frac{p(\boldsymbol{y}|X,\boldsymbol{w})\ p(\boldsymbol{w})}{p(\boldsymbol{y}|X)}. \qquad \text{(Eq. 11)}$$

Where the marginal likelihood, also known as the normalization constant which is the integral of posterior weighted by the probability of the corresponding weights, is given by [39]:

$$p(\boldsymbol{y}|X) = \int p(\boldsymbol{y}|X, \boldsymbol{w})\, p(\boldsymbol{w})\, d\boldsymbol{w}. \qquad \text{(Eq. 12)}$$

The posterior in Eq. 11 combines our prior beliefs and observed data (likelihoods). The numerator in Eq. 11 can be computed for the function provided by Eqs. 7-10 as [76]:

$$p(\boldsymbol{y}|X, \boldsymbol{w})\, p(\boldsymbol{w}) = \exp\left(-\frac{1}{2\sigma_n^2}\, (\boldsymbol{y} - X^T\boldsymbol{w})^T\, (\boldsymbol{y} - X^T\boldsymbol{w})\right) \times \exp\left(-\frac{1}{2}\, \boldsymbol{w}^T\Sigma_p^{-1}\boldsymbol{w}\right).$$
$$\Rightarrow p(\boldsymbol{y}|X, \boldsymbol{w})\, p(\boldsymbol{w}) = \exp\left(-\frac{1}{2\sigma_n^2}\, (\boldsymbol{w} - \bar{\boldsymbol{w}})^T \left(\frac{1}{\sigma_n^2}\, X\, X^T + \Sigma_p^{-1}\right)(\boldsymbol{w} - \bar{\boldsymbol{w}})\right). \qquad \text{(Eq. 13)}$$

Where $\bar{\boldsymbol{w}}$ is given by Eq. 14.

$$\bar{\boldsymbol{w}} = \frac{1}{\sigma_n^2}\left(\frac{1}{\sigma_n^2}\, X\, X^T + \Sigma_p^{-1}\right)^{-1} X\, \boldsymbol{y}. \qquad \text{(Eq. 14)}$$

If we define the covariance matrix $A$ to be given by [76]:

$$A = \frac{1}{\sigma_n^2}\, XX^T + \Sigma_p^{-1}, \qquad \text{(Eq. 15)}$$

then Eq. 13 can be rewritten as [76]:

$$prior\ \times likelihood = \ p(\boldsymbol{y}|X, \boldsymbol{w})\, p(\boldsymbol{w}) = N(\bar{\boldsymbol{w}}, A^{-1}).$$
$$\Rightarrow posterior\ \propto\ N(\bar{\boldsymbol{w}}, A^{-1}). \qquad \text{(Eq. 16)}$$

In non-Bayesian regression approaches the unknown parameters are chosen by some criterion like the ‘least square method’. However, in Gaussian processes, to make a prediction for an unseen test case, an integral over all possible parameters weighted by posterior probability is taken. Therefore the predictive distribution for $f(x^*)$ at the unseen test input $x^*$ is given by [76]:

$$p(f^*|x^*, X, \boldsymbol{y}) = \int p(f^*\backslash x^*, \boldsymbol{w})\, p(\boldsymbol{w}|X, \boldsymbol{y}) d\boldsymbol{w}$$
$$= N\left(\frac{1}{\sigma_n^2}\, x^{*T} A^{-1} X\boldsymbol{y}, x^{*T} A^{-1} x^*\right). \qquad \text{(Eq. 17)}$$

In the formulations above, the Bayesian linear model is assumed which may suffer from limited expressiveness (e.g., for highly non-linear systems). One simple idea to overcome this problem is to project the provided input into a high dimensional space of powers of *x*, basis functions such as $\phi(x) = \{1, x, x^2, x^3, \ldots\}^{\mathrm{T}}$, and then apply the former approach to come up with the predictive distribution. Since the projections are functions of input space and not the weighting coefficients, the model is still linear with respect to the weight parameters. Assume that $\Phi$ is the matrix aggregating all the input function for the *n* provided observations. Then the model is given by Eq. 18 [76].

$$f(x) = \Phi(x)^T \boldsymbol{w}. \qquad \text{(Eq. 18)}$$

The analysis of the model in Eq. 18 follows exactly the same steps and procedure as shown by Eq. 7 through Eq. 17 except that everywhere $\Phi(\mathrm{x})$ is substituted for *X*. Therefore the predictive distribution for the new model becomes [76]:

$$p(f^*|x^*, X, \boldsymbol{y}) = N\left(\frac{1}{\sigma_n^2}\ \phi(x^*)^T A^{-1}\Phi\boldsymbol{y}, \phi(x^*)^T A^{-1}\phi(x^*)\right), \qquad \text{(Eq. 19)}$$

where *A* is given by Eq. 20 [76].

$$A = \frac{1}{\sigma_n^2}\ \Phi\Phi^T + \Sigma_p^{-1}. \qquad \text{(Eq. 20)}$$

In Eq. 19 the inverse of matrix *A* which has the dimension of *N*×*N* is needed which might be time/memory consuming. However, we can rewrite Eq. 19 by defining $\mathrm{K} = \Phi^T\Sigma_p\Phi$ as Eq. 21 [76].

$$p(f^*|x^*, X, \boldsymbol{y}) = N\left(\phi^{*T}\Sigma_p\Phi\ (\mathrm{K} + \sigma_n^2 I)^{-1}\boldsymbol{y}\ , \phi^{*T}\Sigma_p\phi^* - \phi^{*T}\Sigma_P\Phi\ (\mathrm{K} + \sigma_n^2 I)^{-1}\Phi^T\Sigma_p\phi^*\right). \qquad \text{(Eq. 21)}$$

The K matrix in Eq. 21 is the covariance matrix. The definition of the covariant matrix, $\mathrm{K} = \Phi^T\Sigma_p\Phi$, is an inner product with respect to the positive definite $\Sigma_p$ matrix. The matrix $\Sigma_p^{\frac{1}{2}}$ exists such that $\Sigma_p = \Sigma_p^{\frac{1}{2}} \times \Sigma_p^{\frac{1}{2}}$. Hence, the covariant matrix can be written as $K = \left(\Sigma_p^{\frac{1}{2}}\phi\right)^T\left(\Sigma_p^{\frac{1}{2}}\ \phi\right)$. Therefore, a simple dot product representation of covariance function is given by Eq. 22 [76].

$$k(x,x') = \psi(x) \,.\, \psi(x'), \qquad where\ \psi(x) = \Sigma_p^{\frac{1}{2}}\ \phi(x). \tag{Eq. 22}$$

As mentioned at the beginning of this section, the weight space view is the more convenient approach to the concept of GP, while the more common approach to the Gaussian process formulation is through the function-space point of view. As stated earlier, “A Gaussian process is a collection of random variables, any finite number of which have a joint Gaussian distribution” [76]. A Gaussian process can be thoroughly specified by its mean function and the corresponding covariance function as Eq. 23 [76].

$$\begin{aligned} &f(x) \approx\ GP\big(m(x), k(x,x')\big). \\ &m(x) = \mathbb{E}\,[f(x)]. \\ &k(x,x') = \mathbb{E}\,\big[\big(f(x) - m(x)\big) \times\ \big(f(x') - m(x')\big)\big]. \end{aligned} \tag{Eq. 23}$$

Although, for ease of understanding, the mean function is assumed to be zero most of the time, this assumption does not change the results. The Gaussian process has been defined as a collection of random variables. Therefore, the consistency of the parameters is implied. In another word, if two random variables are defined through a GP process as $(y_1, y_2) = N(\mu, \Sigma)$, then there are $\mu_1, \mu_2, \Sigma_1$ and $\Sigma_2$ such that $y_1 = N(\mu_1, \Sigma_1)$ and $y_2 = N(\mu_2, \Sigma_2)$.

Now assume the basic Bayesian linear model provided by $f(x) = \phi(x)^T\boldsymbol{w}$ where we assume the prior distribution for the weights to be $\boldsymbol{w} = N\big(0, \Sigma_p\big)$. Then the corresponding mean and covariance function will be given by Eq. 24. This equation shows that the output distribution at any two given points is a joint Gaussian distribution with zero mean and covariance given by $\phi(x)^T\Sigma_P\phi(x)$.

$$\begin{aligned} &m(x) =\ \mathbb{E}[f(x)] = \phi(x)\mathbb{E}[\boldsymbol{w}] = 0. \\ &k(x,x') = \mathbb{E}\big[\big(f(x) - m(x)\big) \times\ \big(f(x') - m(x')\big)\big] =\ \mathbb{E}[f(x) \times f(x')]. \\ &\to k(x,x') = \phi(x)^T\mathbb{E}[\boldsymbol{w}\boldsymbol{w}^T]\phi(x') = \phi(x)\Sigma_P\phi(x'). \end{aligned} \tag{Eq. 24}$$

Now consider the case of noise-free observations. The joint distribution of the target values used as the training set and the test set can be written as Eq. 25 [76].

$$\begin{bmatrix} f \\ f^* \end{bmatrix} \approx N\left(0\,, \begin{bmatrix} K(X,X) & K(X,X^*) \\ K(X,X^*) & K(X^*,X^*) \end{bmatrix}\right). \tag{Eq. 25}$$

In Eq. 25, the term $K(X, X^*)$ is the matrix of covariance evaluated at the *n*, training observations, and *n**, testing points. The predictive distribution of the target function is given by Eq. 26 [76].

$$f^*|X^*, X, f \approx N\left(K(X, X^*)K(X, X)^{-1}f\,, K(X^*, X^*) - K(X^*, X)K(X, X)^{-1}K(X, X^*)\right). \qquad \text{(Eq. 26)}$$

Eq. 26 follows from Eq. 25 because according to Von Mises [81] if *x* and *y* are jointly Gaussian random vectors as in (Eq. 27) [76],

$$\begin{bmatrix} x \\ y \end{bmatrix} \approx N\left(\begin{bmatrix} \mu_x \\ \mu_y \end{bmatrix}, \begin{bmatrix} A & C \\ C^T & B \end{bmatrix}\right) = N\left(\begin{bmatrix} \mu_x \\ \mu_y \end{bmatrix}, \begin{bmatrix} \tilde{A} & \tilde{C} \\ \tilde{C}^T & \tilde{B} \end{bmatrix}^{-1}\right), \qquad \text{(Eq. 27)}$$

then the corresponding marginal and conditional distribution of *x* given *y* are given by Eq. 28 or Eq. 29, respectively [76].

$$x \approx N(\mu_x, A) \; and \; x|y \approx N\left(\mu_x + CB^{-1}\left(y - \mu_y\right), A - CB^{-1}C^T\right). \qquad \text{(Eq. 28)}$$

$$x|y \approx N\left(\mu_x - \tilde{A}^{-1}\tilde{C}\left(y - \mu_y\right), \tilde{A}^{-1}\right). \qquad \text{(Eq. 29)}$$

In real practical cases we do not usually have access to the exact target values; therefore, it is assumed that the target has an additive distributed noise term, $\epsilon$, with the variance of $\sigma_n^2$. The joint distribution of the target values and the test set will be given by Eq. 30 [76].

$$\begin{bmatrix} y \\ f^* \end{bmatrix} \approx N\left(0\,, \begin{bmatrix} K(X, X) + \sigma_n^2\,\mathrm{I} & K(X, X^*) \\ K(X, X^*) & K(X^*, X^*) \end{bmatrix}\right). \qquad \text{(Eq. 30)}$$

The conditional distribution corresponding to the prior given by Eq. 30 is given by Eq. 31 [76].

$$f^*|X, y, X^* \approx N\left(\bar{f}^*, cov(f^*)\right), \qquad \text{(Eq. 31)}$$

where the mean and covariance are given by Eq. 32 (which is the generalized solution of Eq. 4) [76].

$$\begin{aligned} \bar{f}^* &= K(X, X^*)(K(X, X) + \sigma_n^2\,\mathrm{I})^{-1}y\,. \\ cov(f^*) &= K(X^*, X^*) - K(X^*, X)(K(X, X) + \sigma_n^2\,\mathrm{I})^{-1}K(X, X^*). \end{aligned} \qquad \text{(Eq. 32)}$$

The marginal likelihood is the integral of the likelihood probability distribution times the prior distribution over all the possible function values *f* given by [76]:

$$p(y|X) = \int p(y|f, X)\, p(f|X)\, df. \qquad \text{(Eq. 33)}$$

Under the Gaussian process the prior is assumed to be Gaussian distribution of zero-mean and the covariance of $K$; thus its logarithm becomes [76]:

$$\log p(f|X) = -\frac{1}{2} f^T K^{-1} f - \frac{1}{2}\log|K| - \frac{n}{2}\log 2\pi. \qquad \text{(Eq. 34)}$$

It can be shown that the product of two Gaussians is an un-normalized Gaussian given by Eq. 35 [81].

$$\begin{aligned} &N(x|a,A)\, N(x|b,B) = Z^{-1}\, N(x|c,C). \\ &C = (A^{-1}+B^{-1})^{-1} \quad \& \quad c = C(A^{-1}a + B^{-1}b)\,. \\ &Z^{-1} = (2\pi)^{-D/2}\, |A+B|^{-1/2} \exp\left(-\frac{1}{2}\,(a-b)^T (A+B)^{-1}(a-b)\right). \end{aligned} \qquad \text{(Eq. 35)}$$

Therefore the log of the marginal likelihood becomes [76]:

$$\log p(y|X) = -\frac{1}{2}\, y^T (K + \sigma_n^2\, \mathrm{I})^{-1} y - \frac{1}{2}\log|K + \sigma_n^2\, \mathrm{I}_{\mathrm{n\times n}}| - \frac{n}{2}\log 2\pi. \qquad \text{(Eq. 36)}$$

In the discussions above, the zero-mean GP algorithm was considered, but using a deterministic mean function, $m(x)$, is trivial. In order to consider a nonzero-mean GP, one can simply apply the usual zero-mean solution to the difference between the observations and the given mean function (with $\sigma_n = 0$) [76, 82]:

$$\begin{aligned} &\bar{f}^* = m(X^*) + K(X^*,X)\big(K(X,X)\big)^{-1}\big(y - m(x)\big). \\ &cov(f^*) = K(X^*,X^*) - K(X^*,X)(K(X,X))^{-1}K(X,X^*). \end{aligned} \qquad \text{(Eq. 37)}$$

### 3.3.3. Gaussian Processes in engineering applications

Gaussian Processes have been used in engineering applications such as in geostatistics, engine modeling, robotics and control [83-94]. The fact that the GP is based on an infinite number of random variables makes explicit solutions available for engineering problems (specially the inverse problems) with random input variables.

In the field of geostatistics, GP is known as the kriging process [83]. The French mathematician, Georges Matheron is the pioneer scientist who formulated the Gaussian Process with his work on estimating the spatial distribution of gold in boreholes based on a few samples collected from a mine in South Africa. The kriging technique was originally developed for geostatistics, but since then has been used in other fields such as environmental sciences, natural resource management and real estate appraisal [83].

Another field which has widely investigated the application of Gaussian Processes for machine learning is robotics and control. As stated earlier, conventional model-based methods suffer from improper model selection as well as the error propagation through the system simulation algorithms because of the initial model errors. The GP algorithm is a non-model based approach for machine learning and regression and this property has created a lot of interest in the field of control and robotics. Deisenroth et al. [84] describe the process of adopting GP in conventional model-based techniques for data-efficient learning in the simulation and control of a robotic arm. The application of Bayesian GP improved the accuracy and efficiency of the learning algorithm dramatically; for instance, the learning success jumps up from 0% in deterministic non-parametric models to ~94% when the GP is applied to simulate the swing up action of a cart-pole [84].

Uncertainty modeling in robotics and adaptive control field has also been studied in the literature [85-89] for both linear and nonlinear systems. Most of these studies focus on parametric model-based techniques, which are challenging (problem specific) and require expert's knowledge of the system elements and its behavior. On the other hand, nonparametric Bayesian techniques provide automatic feature extraction ability from the latent physical/dynamic problem. Different approaches have been taken in the literature to deal with the uncertainty of input parameters in the Bayesian framework; such as sampling the model parameters from the posteriors [90] or treating uncertainty as a noise factor [91].

The performance and accuracy of model-based techniques for engine calibration has been of interest by researchers and industries for many years. Due to the increasing number of structural/design sub elements, emission reducing technologies, legislative directions and customer desires, there is a need to optimize and automate the engine calibration processes [92]. The performance of engine calibration, on the other hand, is highly dependent on the type of modeling process and the accuracy of the training data. The outliers are the main concerns in this field. The purpose of developing calibration models is to deal with the outlier measurements when the actual system is in service. However, the occurrence of outliers in the training process put the accuracy and efficiency of the model-based approaches at high risk. This is one of the main drawbacks of implementing a conventional model-based calibration technique in noise-sensitive fields such as engines. In the case of outliers in the training data, either manual interaction is required or the automatic detection of outliers is not robust. Common types of modeling methods used for engine calibration can be categorized into polynomial regression, tree-based models and machine learning algorithms [92, 93]. In the category of machine learning approaches, MLP Neural Networks, Support Vector Machines, Relevance Vector Machines and the Gaussian Processes have been used to automate the calibration process. Berger [94] implemented the GP algorithm to calibrate a diesel engine for the NOx production and soot measurement using normal noise assumption and compared the results to the student's noise assumption. A five dimensional input space consisting of quantity of exhaust gas, quantity and time of pre-injection and the pressure and time of the main injection at a single operating point is considered. From 279 measurements, 35 were randomly chosen and kept aside for testing the accuracy of the developed algorithms and the rest were part of the training process. The implementation of the GP resulted in high accuracy predictions for both the NOx and the soot measurements by ~97% for t-student's noise distribution and ~90% for the normal noise distribution.

In this thesis, for the first time in the field of composite materials, equations 32 & 36 will be programmed in MATLAB and applied to the airfoil SHM case study of chapter 6 in order to develop a robust SHM system. The results are presented in chapter 8.

## 3.4. Signal-to-Noise (SN) ratio analysis

Signal-to-noise ratio analysis (often called SN or SNR) is a way for comparing the level (amplitude) of the desired signal to the corresponding level of the background noise (fluctuations/variations) in the measurement. This concept is widely used in electrical and electromagnetics engineering where the log function of the ratio of the signal to noise is defined as the SN or SNR factor. There are two main approaches for measuring the SN ratios, namely static SN and dynamic SN. In turn, there are three formulas to define a SN ratio in the static mode which includes [95]:

- The larger the better static SN
- The nominal the best static SN
- The smaller the better static SN

Assume $y_{ij}$ indicates the signals measured by the instruments at each sensor point (*m* number of sensors) for each repeat (*n* experiments) and the $\bar{y}_i$ indicates the average value for each node calculated from all different experimental date; the above mentioned static SN ratios can be estimated by [95]:

- Larger-the-best static SN ratio: $-10\log_{10}\left(\frac{1}{m}\sum\frac{1}{y_{ij}^2}\right)$.
- Smaller-the-best static SN ratio: $-10\log_{10}\left(\frac{1}{m}\sum y_{ij}^2\right)$.
- Nominal-the-best static SN ratio: $10\ \log_{10}\left(\frac{\bar{y}_i{}^2}{s_i^2}\right)$ where $\ln s_i^2 = \ln\frac{\sum\left(y_{ij}-\bar{y}_i\right)^2}{m-1}$.

In the dynamic signal-to-noise ratio analysis, all the measured data are plotted in the x-y plane and the slope of the linear regression line passing through them is calculated; if *MSE* indicates the mean square error, then the dynamic SN ratio is defined as the following equation [96]:

- Dynamic SN ratio: $10\ \log_{10}\frac{slope^2}{MSE}$.

The concept of signal-to-noise ratio has been widely used in engineering and medical applications. Welvaert [97] studied the signal to noise ratio of MRI (Magnetic Resonance Imaging) data under fluctuations of background noise (called fMRI) for different SN formulas. That study showed the high importance of SN definitions and the corresponding activation functions. Griffanti et al. [98] implemented seven estimates for SN ratios on a uniform phantom Diffusion Weighted (DW) image to arrive at an optimized spinal cord DW procedure. The optimized procedure successfully enhanced the previous studies on the MRI on phantoms.

Poungponsri and Yu [99] implemented multilayer neural networks to filter out the noise in Electrocardiogram (ECG) results in order to detect heart diseases. They combined the discrete wavelet transformers (for their multi-resolution properties) and neural networks (for their ability to adapt) to detect a variety of noises and increase the SN ratio significantly.

Liu et al. [100] investigated a feed-forward back-propagation neural network for enhancing the SN ratio of ultrasonic signals used for nondestructive testing of highly scattering materials. They studied noisy ultrasonic waves in composite and metallic structures in spite of the conventional techniques such as Wiener filtering, maximum likelihood estimation and adaptive filtering. The performance of the NN filtering technique developed was superior compared to conventional adaptive filter.

The idea of weighting the input layer of the neural network to demonstrate the importance of individual measurement points has been studied in the literature in different fields of science and engineering. Zou et al. [101] used back-propagation neural networks with a Levenberg-Marquardt learning algorithm to study the protein combinations of both amino acid and amino pairs. The overall accuracy of prediction reached 88.4%, which is an enhancement compared to conventional neural networks with the accuracies as low as 66.1%.

Chen et al. [102] applied the weighted input layer (taken from the information entropy theory) to the Elman NN to predict gas turbine performance. The application of the entropy theory to the conventional Elman neural network resulted in decreased mean square error of the training/prediction process by ~29% for real-time predictions.

In this thesis, in the field of composite materials, S/N equations will be programmed in MATLAB and for the first time applied to the airfoil SHM case study of in chapter 5 in order to develop a robust SHM system. The results are presented in chapter 6.

## 3.5. Summary of the background theory on the selected machine learning algorithms

In this chapter the theoretical background on the computational aspects of the structural health monitoring system under development was presented. Namely, the well-known machine learning algorithms of Artificial Neural Networks and Gaussian Processes were discussed. The concept of Signal-to-Noise ratio analysis was introduced and will be applied to the conventional MLP networks to improve their prediction capabilities.

# Chapter 4

# Proof of Concept Study 1: Effect of Fabrication and Testing Uncertainties in SHM of a T-joint Structure

## Chapter preview

In this chapter a preliminary feasibility study is conducted on a composite T-joint structure to show the impact of misalignment/change in loading direction on the strain measurements from the strain gauge sensors embedded in the structure. Two approaches are considered, the first (point-to-point analysis) approach analyzes the data gathered from only three strain gauges; while, the other approach (integral analysis) deals with continuous strain measurement (over 400 nodes). The results show that the misalignment of fibers or deviation in static tensile loading only by $5^o$ can lead to abnormalities in the strain measurement which are comparable to the case of damaged structure. It will also be shown that adding more sensors to the analysis do not necessarily eliminate the effect of uncertainty, which means for more practical SHM systems/statistical pattern recognition algorithms capable of handling the uncertainty should be developed.

## 4.1. Introduction to case study 1

The review of literature in Chapter 2 showed an increasing number of SHM research programs devoted to the development of damage identification systems to address problems such as cost-effective methods for optimal numbering and positioning of sensors; identification of features of structures that are sensitive to small damage levels; the ability to discriminate changes caused by damage from those due to the change of environmental and testing conditions; clustering and classification algorithms for discrimination of damaged and undamaged states; and comparative studies on different damage identification methods applied to common datasets [1, 2]. These topics are currently the focus of various groups in major industries including aeronautical [3, 4], civil infrastructure [5], oil [6, 7], railways [8], condition monitoring of machinery [9, 10], automotive and semiconductor manufacturing [2]. In particular, new multi-disciplinary approaches are increasingly developed and used to advance the capabilities of current SHM techniques.

## 4.2. Motivation of this case study

As reviewed in Chapter 2, a standard SHM technique for a given structure compares its damaged and healthy behaviors (by contrasting signals extracted from sensors embedded at specific points of the structure) to the database pre-trained from simulating/testing the behavior of the structure under different damage scenarios. Ideally, the change in the vibration spectra/stress-strain patterns can be related to damage induced in the structure, but it is possible at the same time that these deviations from a healthy pattern are caused by imperfect manufacturing processes like uncertainty in material properties or misplacement of fibers inside the matrix (in the case of composite structures), an offset of an external loading applied to the structure during testing, etc. Based on a strained-based SHM, this article addresses the important effect of manufacturing/testing uncertainties on the reliability of damage predictions. To this end, a benchmark problem from the literature is used as a case study along with a finite element analysis and design of experiments (DOE) method. Among several existing DOE experimental designs (e.g., [11-16]) the well-known full factorial design (FFD) is used.

## 4.3. Case study description

The structure under investigation is a composite T-joint introduced in [17], where a strain-based structural health monitoring program, GNAISPIN (Global Neural network Algorithm for Sequential Processing of Internal sub Networks), was developed using MATLAB and NASTRAN-PATRAN. The T-joint structure, shown in Figure 4.1, consists of four major segments including the bulkhead, hull, over-laminates and the filler section. The finite element model of the structure is assumed to be two-dimensional (2D) and strain patterns are considered to be identical in the thickness direction of the structure. The geometrical constraints and applied load are also shown in Figure 4.1. The left-hand side constraint only permits rotation about the z-axis and prevents all other rotational and translational degrees of freedom. The right-hand side constraint permits translation along the x-axis (horizontal direction) and rotation about the z-axis. The displacement constraints are positioned 120mm away from the corresponding edges of the hull. The structure is subjected to a tensile pull-off force of 5 kN. In [17], several artificial delaminations were embedded in different locations of the structure, but in this study only a single artificial delamination case is considered between hull and the left overlaminate. The artificial delaminations were created during the production process by inserting a waxed piece of Teflon between composite plies. In this way, the corresponding plies will stay detached after the curing and there will not be high stress concentration on the starting/ending nodes of the delamination. The strain distribution is then obtained for nodes along the bond-line (the top line of the hull between the right- and left-hand constraints), which are the nodes most affected by the presence of embedded delamination.

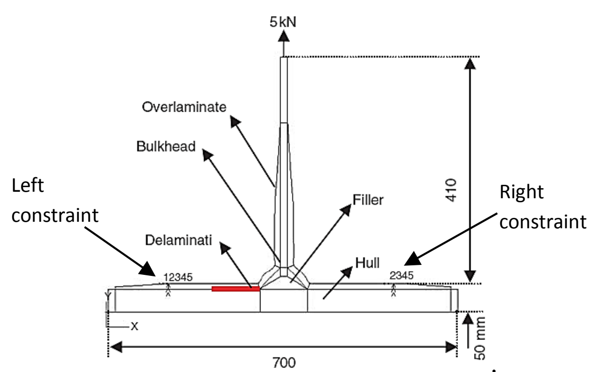


**Figure 4.1.** Geometry of the T-joint considered in the case study [17]

Using ABAQUS software, two dimensional orthotropic elements were used to mesh surfaces of the bulkhead, hull, and overlaminates, whereas isotropic elements were used to model the filler section. The properties of the hull, bulkhead, and the overlaminates [17], corresponded to 800 grams-per-square of plain weave E-glass fabric in a vinylester resin matrix (Dow Derakane 411-350). The properties of the filler corresponded to chopped glass fibers in the same vinylester resin matrix.

**Table 4.1.** Elastic properties of the T-joint components

| Elastic Properties | Hull and Bulkhead | Overlaminate | Filler (quais-isotropic) |
|---|---|---|---|
| E1 (GPa) | 26.1 | 23.5 | 2.0 |
| E2 (GPa) | 3.0 | 3.0 | |
| E3 (GPa) | 24.1 | 19.5 | |
| v12=v23 | 0.17 | 0.17 | 0.3 |
| v13 | 0.10 | 0.14 | |
| G12=G23 (GPa) | 1.5 | 1.5 | 0.8 |
| G13 (GPa) | 3.3 | 2.9 | |

In order to verify the developed base ABAQUS model, strain distributions along the bond-line for the two cases of healthy structure and that with an embedded delamination are compared to the corresponding distributions presented in [17]. Figures 4.2.a and 4.2.b show a good accordance between the current simulation model and the one presented in [17] using NASTRAN-PATRAN. The only significant difference between the two models is found at the middle of the T-joint where results in [17] show a significant strain drop compared to the ABAQUS simulation. Figure 4.3 also illustrates the 2D strain distribution obtained by the ABAQUS model for the healthy structure case.

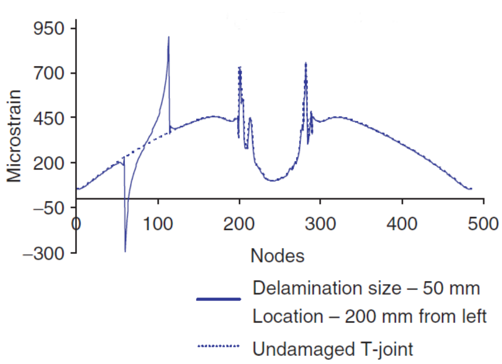


a) Strain patterns in [17] via NASTRAN-PATRAN model

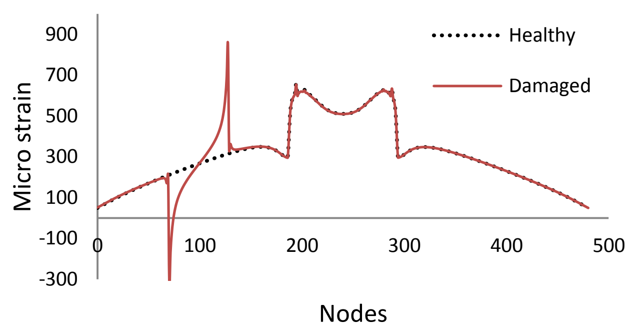


b) The strain pattern obtained via ABAQUS model (the delamination size and location were identical to the NASTRAN-PATRAN model)

**Figure 4.2.** Comparison of strain distributions along the bond-line of the T-joint for different cases

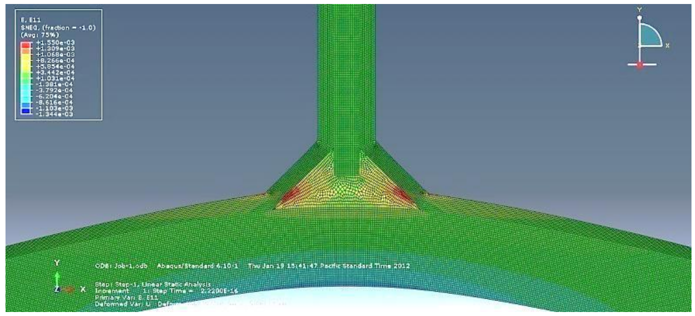

**Figure 4.3.** Strain field in the healthy T-joint via ABAQUS model (notice the symmetrical pattern)

Next, using the ABAQUS model for the DOE study, fiber orientations in the bulkhead, hull and overlaminate as well as the pull-off loading offset were considered as four main factors via a full factorial design, which resulted in sixteen runs for each of the health states (healthy vs. damaged structure). Two levels for each factor were considered: 0 or +5 degrees counter-clockwise with respect to the x-axis (Figure 4.4). Table 4.2 shows the assignment of considered factors and their corresponding levels. Table 4.3 represents the full factorial design for the two structural health cases.

**Table 4.2.** Factors and the corresponding levels considered in the DOE study

| | Factors | Coding | Levels (in degrees) |
|---|---|---|---|
| Regions of fiber angle error (misalignment) | Overlaminate | A | 0 or 5 |
| | Bulkhead | B | 0 or 5 |
| | Hull | C | 0 or 5 |
| Loading offset | Loading angle | D | 0 or 5 |

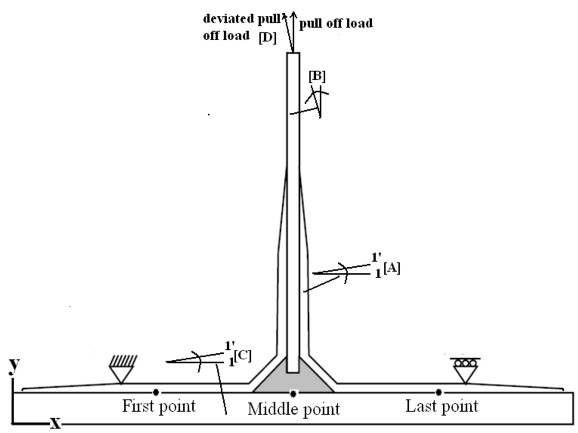


**Figure 4.4.** Schematic of study factors along with the position of the first, middle and the last nodes considered during the first DOE analysis

**Table 4.3.** Full factorial design resulting in a total of 32 simulations ($2^4$ for the healthy structure and $2^4$ for the damaged structure)

| | Factors (all angles in degrees) | | | | |
|---|---|---|---|---|---|
| run # | A | B | C | D | Case |
| 1 | 0 | 0 | 0 | 0 | No Delamination |
| 2 | 5 | 0 | 0 | 0 | |
| 3 | 0 | 0 | 5 | 0 | |
| 4 | 5 | 0 | 5 | 0 | |
| 5 | 0 | 5 | 5 | 0 | |
| 6 | 5 | 5 | 5 | 0 | |
| 7 | 0 | 5 | 0 | 5 | |
| 8 | 5 | 5 | 0 | 5 | |
| 9 | 0 | 0 | 0 | 5 | |
| 10 | 5 | 0 | 0 | 5 | |
| 11 | 0 | 0 | 5 | 5 | |
| 12 | 5 | 0 | 5 | 5 | |
| 13 | 0 | 5 | 5 | 5 | |
| 14 | 5 | 5 | 5 | 5 | |
| 15 | 0 | 5 | 0 | 0 | |
| 16 | 5 | 5 | 0 | 0 | |
| 17 | 0 | 0 | 0 | 0 | Delamination of 50mm long at 200mm from left edge |
| 18 | 5 | 0 | 0 | 0 | |
| 19 | 0 | 0 | 5 | 0 | |
| 20 | 5 | 0 | 5 | 0 | |
| 21 | 0 | 5 | 5 | 0 | |
| 22 | 5 | 5 | 5 | 0 | |
| 23 | 0 | 5 | 0 | 0 | |
| 24 | 5 | 5 | 0 | 0 | |
| 25 | 0 | 0 | 0 | 5 | |
| 26 | 5 | 0 | 0 | 5 | |
| 27 | 0 | 0 | 5 | 5 | |
| 28 | 5 | 0 | 5 | 5 | |
| 29 | 0 | 5 | 5 | 5 | |
| 30 | 5 | 5 | 5 | 5 | |
| 31 | 0 | 5 | 0 | 5 | |
| 32 | 5 | 5 | 0 | 5 | |

In order to illustrate the importance of the effect of uncertainty in fiber misalignment (e.g., during manufacturing of the structure's components), one can readily compare the difference between the strain distributions obtained for a case containing, e.g., $5^o$ misalignment in the overlaminate (i.e., run # 2 in Table 4.3) and that for the perfectly manufactured healthy case (run # 1). A similar difference can be plotted between the case without any misalignment but in the presence of delamination (damage)-- which corresponds to run # 17 – and the perfectly manufactured healthy case (run # 1). These differences are shown in Figure 4.5.

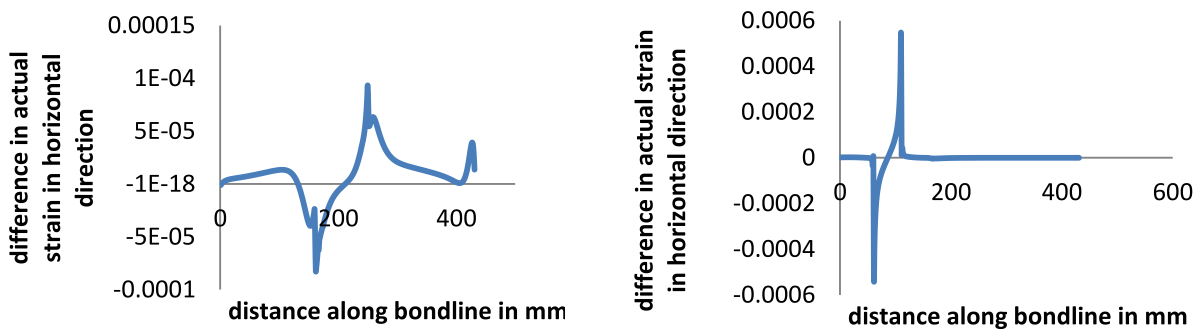


(a) Run # 2 – Run # 1 (b) Run # 17 – Run # 1

**Figure 4.5.** Differences in strain distributions of sample runs in Table 4.3

By comparing the strain distributions in Figures 4.5.a and 4.5.b one can conclude that 5 degrees misalignment of fibers in the overlaminate (run # 2) has resulted in a significant deviation from the base model (run # 1) compared to the same deviations caused by the presence of delamination (run # 17); and hence, emphasizing the importance of considering fiber misalignment in real SHM applications and database developments. The next section is dedicated to perform a more detailed factorial analysis of results and obtain relative effects of the four alignment factors A, B, C, and D as samples of uncertainty sources in practice.

## 4.4. DOE effects analysis

Two different approaches are considered in the effects analysis; a point-to-point and an integral analysis. In the point-to-point approach, the difference between the horizontal strain ($\epsilon_x$) values at three locations along the bond-line (first, middle and the last node in Figure 4.4) and those of the ideal case are considered as three output variables. On the other hand, the integral approach continuously evaluates the strain along the bond line where the number of considered points (sensors) tends to infinity. In fact the strain values obtained from the FE analysis would correspond to the strain data extracted from sensors embedded in the T-joint. The integral analysis for each given run, calculates the area under the strain distribution along the bond line, minus the similar area in the ideal case. The comparison of the two approaches, hence, provides an opportunity to assess the impact of increasing the number of sensors on the performance of SHM in the presence of manufacturing errors (here misalignments). For each approach, the most dominant factors are identified via comparing their relative percentage contributions on the output variables as well as the corresponding half-normal probability plots and ANOVA analysis (see [16] for more theoretical details). Subsequently, ANOVA analysis will be performed to statistically determine the significance (F-value) of key factors.

**Point-to-point analysis results:**

Figure 4.4 shows the position of nodes assigned for the point-to-point analysis strategy. The first and last points are considered to be 50mm away from the nearest constraint on the contact surface of hull and overlaminate. The middle point is located below the pull-off load point. Table 4.4 shows the results of FE runs based on the factor combination introduced in Table 4.3. As addressed before, the presented data for the first group of runs (i.e., for healthy structures – runs 1 to 16) are the difference between strain values of each run and run 1; while the corresponding data for the second group (damaged T-joint – runs 17 to 32) represent the difference between strain values for each run and run 17. Table 4.5 represents the ensuing percentage contributions factors and their interactions at each node for the two cases of healthy and delaminated T-joint. For the first node, which is close to the most rigid constraint on the left hand side of the structure, the only important factors are the misalignment of fibers in the hull (factor C) and its interaction with the loading angle offset (CD). This can be explained by the type of constraints imposed on the structure which is free horizontal translation of the opposite constraint on the right side (along the x-direction). Figure 4.6 shows the half normal probability plot of the factor effects for the 1$^{st}$ node, confirming that factors C and CD as the distinctly dominant parameters affecting the strain response at this node.

One would expect that the mid node response would be strongly influenced by any loading angle offset as it can produce a horizontal force component and magnify the effect of the free translation boundary condition on the neighboring constraint; therefore, for the middle point response, the misalignment of fibers in the hull (C) and the loading angle error (D) and their interactions (CD) are the most significant factors, as also shown from the corresponding half normal probability plot in Figure 4.7. Finally, due to the short distance of the last (3$^{rd}$) measuring node to the right constraint point and the strong influence of the large hull section beneath this measuring node, the parameter C was found to be the most dominant factor, followed by D, CD, AC, AD, and ACD (Figure 4.8).

**Table 4.4.** Results of the DOE runs for the point-to-point analysis (A: Overlaminate – B: Bulkhead – C: Hull– D: Loading angle)

| Run# | Factors | | | | Response | | | Structure's health status |
|---|---|---|---|---|---|---|---|---|
| | A | B | C | D | @1st node | @middle node | @end node | |
| 1 | 0 | 0 | 0 | 0 | 0 | 0 | 0 | No Delamination (Healthy) |
| 2 | 5 | 0 | 0 | 0 | 1.0979E-06 | 2.273E-06 | 0.000013536 | |
| 3 | 0 | 0 | 5 | 0 | 4.23422E-05 | 3.0625E-05 | 4.04549E-05 | |
| 4 | 5 | 0 | 5 | 0 | 4.4637E-05 | 0.000029522 | 5.78129E-05 | |
| 5 | 0 | 5 | 5 | 0 | 4.23426E-05 | 0.000032361 | 4.04549E-05 | |
| 6 | 5 | 5 | 5 | 0 | 4.46377E-05 | 3.1389E-05 | 5.78129E-05 | |
| 7 | 0 | 5 | 0 | 5 | 2.58877E-05 | 0.000040385 | 1.21364E-05 | |
| 8 | 5 | 5 | 0 | 5 | 2.71377E-05 | 0.000038519 | 5.23E-07 | |
| 9 | 0 | 0 | 0 | 5 | 2.58911E-05 | 0.000036949 | 0.000012135 | |
| 10 | 5 | 0 | 0 | 5 | 2.71419E-05 | 0.000034988 | 5.219E-07 | |
| 11 | 0 | 0 | 5 | 5 | 2.17078E-05 | 0.000111352 | 2.26219E-05 | |
| 12 | 5 | 0 | 5 | 5 | 2.16311E-05 | 0.000105259 | 3.74989E-05 | |
| 13 | 0 | 5 | 5 | 5 | 2.17102E-05 | 0.000115452 | 2.26229E-05 | |
| 14 | 5 | 5 | 5 | 5 | 0.000021634 | 0.000109486 | 3.74999E-05 | |
| 15 | 0 | 5 | 0 | 0 | 5E-10 | 1.445E-06 | 0 | |
| 16 | 5 | 5 | 0 | 0 | 1.0987E-06 | 3.83E-06 | 1.35358E-05 | |
| | A | B | C | D | @1st node | @middle node | @end node | |
| 17 | 0 | 0 | 0 | 0 | 0 | 0 | 0 | Delamination of size 50mm at 210mm from left |
| 18 | 5 | 0 | 0 | 0 | 8.428E-07 | 1.744E-06 | 1.35359E-05 | |
| 19 | 0 | 0 | 5 | 0 | 4.22965E-05 | 0.000030471 | 4.04562E-05 | |
| 20 | 5 | 0 | 5 | 0 | 4.43366E-05 | 0.000028817 | 5.78142E-05 | |
| 21 | 0 | 5 | 5 | 0 | 4.22971E-05 | 0.000032214 | 4.04562E-05 | |
| 22 | 5 | 5 | 5 | 0 | 4.43376E-05 | 0.00003069 | 5.78142E-05 | |
| 23 | 0 | 5 | 0 | 0 | 8E-10 | 1.416E-06 | 1E-10 | |
| 24 | 5 | 5 | 0 | 0 | 8.44E-07 | 3.272E-06 | 1.35357E-05 | |
| 25 | 0 | 0 | 0 | 5 | 2.61841E-05 | 0.000035177 | 1.21353E-05 | |
| 26 | 5 | 0 | 0 | 5 | 0.000027744 | 3.2725E-05 | 5.221E-07 | |
| 27 | 0 | 0 | 5 | 5 | 2.61841E-05 | 0.000035177 | 1.21353E-05 | |
| 28 | 5 | 0 | 5 | 5 | 2.09678E-05 | 0.000103816 | 3.75002E-05 | |
| 29 | 0 | 5 | 5 | 5 | 2.13567E-05 | 0.000114459 | 2.26242E-05 | |
| 30 | 5 | 5 | 5 | 5 | 2.09723E-05 | 0.000107997 | 3.75012E-05 | |
| 31 | 0 | 5 | 0 | 5 | 2.61794E-05 | 0.000038553 | 1.21366E-05 | |
| 32 | 5 | 5 | 0 | 5 | 0.000027738 | 0.000036197 | 5.233E-07 | |

**Table 4.5.** Percentage contributions of the factors from the point-to-point analysis results in Table 4.4; all values are in %; the bold numbers refer to the high contributions

| Factors | @first node | | @middle node | | @last node | |
|---|---|---|---|---|---|---|
| | Healthy | Damaged | Healthy | Damaged | Healthy | Damaged |
| A | 0.13868 | 0.017835 | 0.043177 | 1.01244 | 4.91255 | 6.414703 |
| B | 8.15E-12 | 0.03857 | 0.117004 | 2.8447 | 1.95E-08 | 0.113719 |
| C | **38.60064** | **38.8124** | **40.42626** | **33.93042** | **73.58083** | **66.59797** |
| D | 0.457217 | 0.827449 | **51.83837** | **42.73814** | **6.411934** | **8.096834** |
| AB | 8.79E-11 | 0.038593 | 5.28E-05 | 1.694425 | 2.63E-10 | 0.113632 |
| AC | 0.000112 | 0.066135 | 0.054639 | 1.098861 | 3.868746 | 5.223829 |
| AD | 0.032741 | 0.112498 | 0.083222 | 0.983084 | 3.214382 | 2.070652 |
| BC | 2.67E-07 | 0.038292 | 0.000938 | 1.810764 | 9.47E-11 | 0.113615 |
| BD | 3.63E-08 | 0.038687 | 0.01842 | 2.126322 | 2.33E-08 | 0.113723 |
| CD | **60.72826** | **59.65124** | **7.417231** | **3.218366** | **5.848022** | **7.467763** |
| ABC | 2.51E-09 | 0.038622 | 6.35E-07 | 1.713334 | 2.63E-10 | 0.113615 |
| ABD | 1.15E-09 | 0.038568 | 1.08E-07 | 1.716435 | 1.05E-11 | 0.113619 |
| ACD | 0.04235 | 0.204216 | 0.000548 | 1.6494 | 2.163531 | 3.219085 |
| BCD | 2.87E-07 | 0.038282 | 0.000141 | 1.748334 | 5.16E-10 | 0.113611 |
| ABCD | 3.12E-09 | 0.038622 | 4.12E-08 | 1.714975 | 1.05E-11 | 0.113628 |

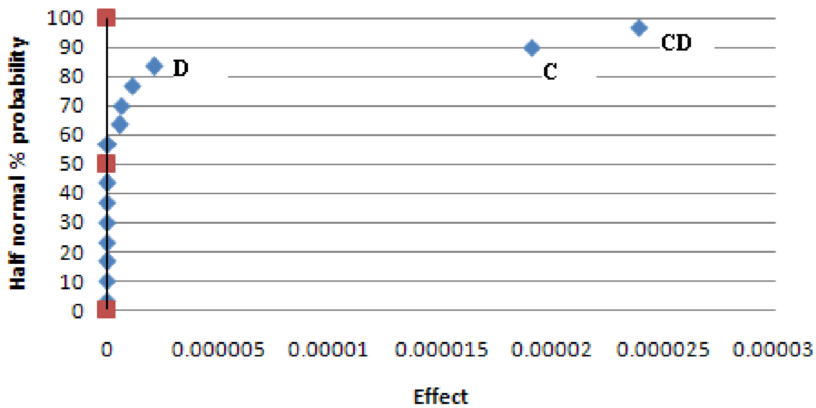


**Figure 4.6.** Half normal probability plot using the response at the 1st node during point-to-point analysis (for healthy structure)

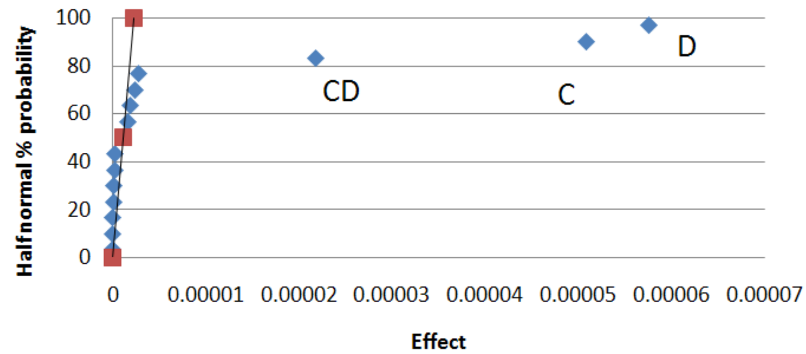


**Figure 4.7.** Half normal probability plot using the response at the 2nd node during the point-to-point analysis (for healthy structure)

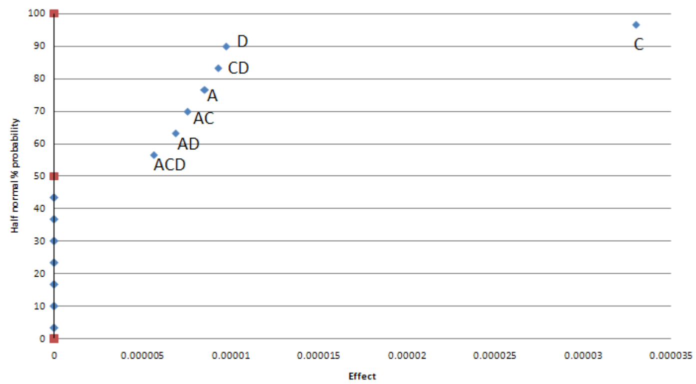


**Figure 4.8.** Half normal probability plot using the response at the 3$^{rd}$ sensor point during point-to-point analysis (for healthy structure)

Next, based on the identified significant factors from the above results for the 3$^{rd}$ node, an ANOVA analysis (Table 4.6) was performed considering the rest of insignificant effects embedded in the error term. As expected, the p-value for the factor C is zero and the corresponding values for factors D and CD are 0.001. The p-value for all other factors is greater than 0.001. Therefore, assuming a significance level of 1%, for the 3$^{rd}$ node response, much like the 1$^{st}$ and middle nodes, factors C, D and their interaction CD can be reliably considered as most significant. Table 4.7 shows the ANOVA results for all the three nodes when only these three factors were included.

**Table 4.6.** Results of ANOVA for the 3$^{rd}$ node response, considering the identified factors from Figure 4.8 for the block of healthy runs (by Minitab statistical software).

| Source | DF | Seq SS | Adj SS | Adj MS | F | P |
|---|---|---|---|---|---|---|
| A | 1 | 291.69 | 291.69 | 291.69 | 20.44 | 0.002 |
| C | 1 | 4368.92 | 4368.92 | 4368.92 | 306.09 | 0.000 |
| D | 1 | 380.71 | 380.71 | 380.71 | 26.67 | 0.001 |
| A*C | 1 | 229.71 | 229.71 | 229.71 | 16.09 | 0.003 |
| A*D | 1 | 190.86 | 190.86 | 190.86 | 13.37 | 0.005 |
| C*D | 1 | 347.23 | 347.23 | 347.23 | 24.33 | 0.001 |
| Error | 9 | 128.46 | 128.46 | 14.27 | | |
| Total | 15 | 5937.57 | | | | |

One very interesting observation during the above analysis was that we found no significant deviation of main results when we repeated the analysis for the block of runs with delamination (compare the corresponding values under each node in Table 4.5 for the two healthy and damage cases). This indicated that *the effects of misalignment (manufacturing and testing error) factors between the healthy and damaged structures at each specific node are generally identical*, in the present case study.

Figures 4.9.a – 4.9.f represent the main factor and interaction plots for the point-to-point analysis. For the first and last points, the lines for interaction of fiber misalignment and the loading angle offset are crossed, which indicates a high interaction between those parameters at the corresponding node. This interaction indication agrees well with the high F-value provided by the ANOVA analysis for CD in Table 4.7 for the first node. For the middle node, the individual lines for C and D in the main plots are in the same direction but with a small difference in their slopes. For the last ($3^{rd}$) node, the main factor plots for parameters C and D have slopes with opposing signs, suggesting that for this node, the fiber misalignment angle and loading angle offset have opposite influences on the strain response. This again could be explained by the imposed type of constraint on the right side of the T-joint.

**Table 4.7.** Results of ANOVA analysis for factors C, D and CD – point-to-point analysis approach (by Minitab statistical software).

@$1^{st}$ node

| Source | DF | Seq SS | Adj SS | Adj MS | F | **P** |
|---|---|---|---|---|---|---|
| C | 1 | 1451.4 | 1451.4 | 1451.4 | 2165.69 | **0.000** |
| D | 1 | 17.2 | 17.2 | 17.2 | 25.65 | **0.000** |
| C*D | 1 | 2283.4 | 2283.4 | 2283.4 | 3407.16 | **0.000** |
| Error | 12 | 8.0 | 8.0 | 0.7 | | |
| Total | 15 | 3759.9 | | | | |

@Middle node

| Source | DF | Seq SS | Adj SS | Adj MS | F | **P** |
|---|---|---|---|---|---|---|
| C | 1 | 10356.0 | 10356.0 | 10356.0 | 1524.83 | **0.000** |
| D | 1 | 13279.4 | 13279.4 | 13279.4 | 1955.28 | **0.000** |
| C*D | 1 | 1900.1 | 1900.1 | 1900.1 | 279.77 | **0.000** |
| Error | 12 | 81.5 | 81.5 | 6.8 | | |
| Total | 15 | 25616.9 | | | | |

@Last node

| Source | DF | Seq SS | Adj SS | Adj MS | F | **P** |
|---|---|---|---|---|---|---|
| C | 1 | 4368.9 | 4368.9 | 4368.9 | 62.36 | **0.000** |
| D | 1 | 380.7 | 380.7 | 380.7 | 5.43 | **0.038** |
| C*D | 1 | 347.2 | 347.2 | 347.2 | 4.96 | **0.046** |
| Error | 12 | 840.7 | 840.7 | 70.1 | | |
| Total | 15 | 5937.6 | | | | |

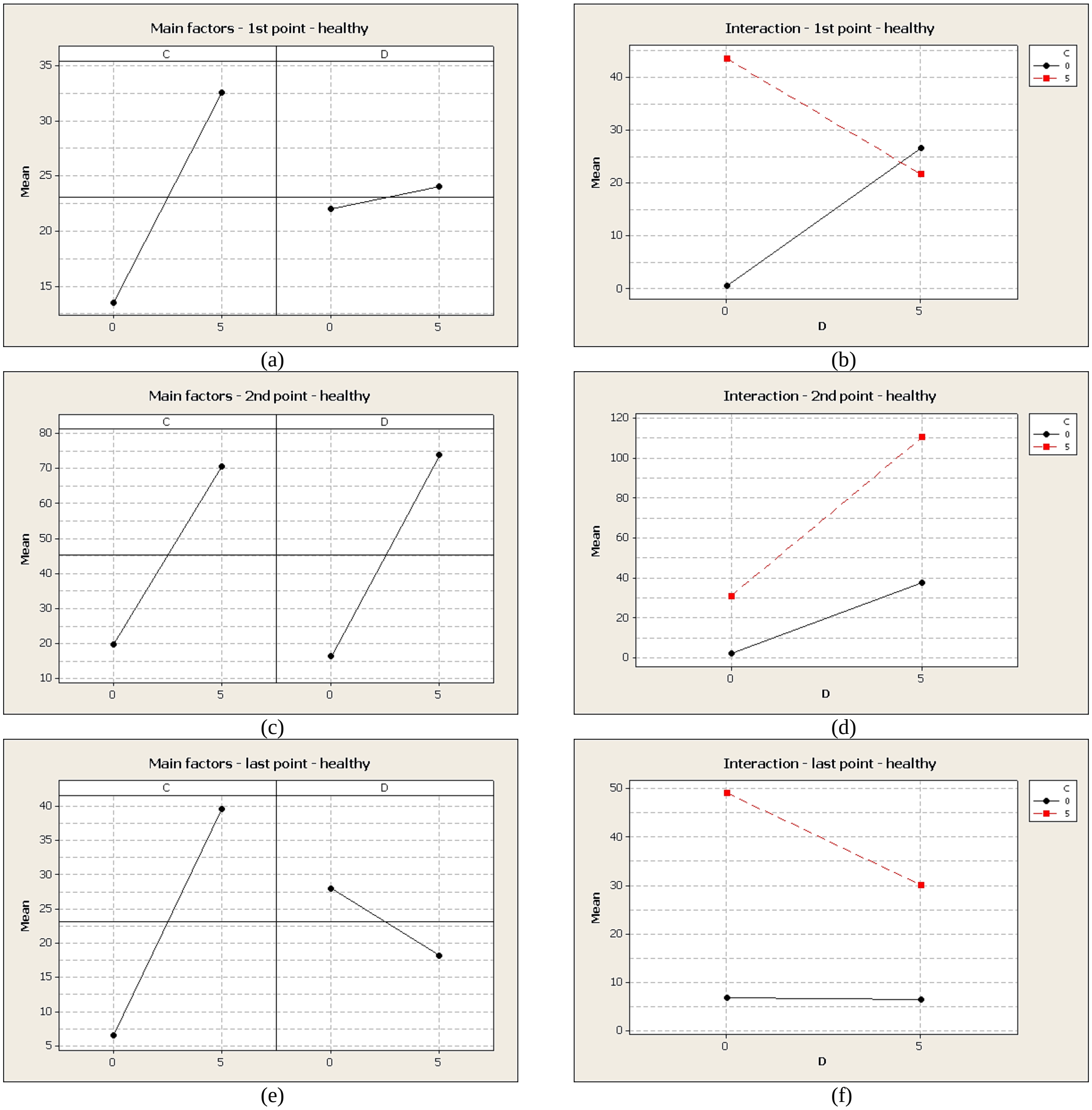


**Figure 4.9.** The main factor and interaction plots for the point-to-point analysis considering C, D and CD factors.

**Integral analysis results:**

In this approach the objective function for each run was considered as the area between the curve representing the strain distribution of the nodes lying on the bond line and that of the base case. For the first group of runs (healthy structure, run#1-16), the first run is the base curve, whereas for the second group (embedded delamination case, run # 17 – 32) the 17$^{th}$ run (i.e., only delamination and no other fiber misalignment or loading angle error) is considered as the base. Table 4.8 lists the objective values for each run during this analysis. Table 4.9 represents the obtained percentage contributions of each factor. The parameters C and CD again play the main role on the strain distribution, but to be more accurate one may also consider other factors such as A, D, AD, and AC.

**Table 4.8.** Results of the DOE runs for the integral analysis (A: Overlaminate – B: Bulkhead – C: Hull– D: Loading angle).

| Run # | A | B | C | D | Integral method response | Structure's state |
|---|---|---|---|---|---|---|
| 1 | 0 | 0 | 0 | 0 | 0 | No Delamination |
| 2 | 5 | 0 | 0 | 0 | 1.79E-05 | |
| 3 | 0 | 0 | 5 | 0 | 4.34E-05 | |
| 4 | 5 | 0 | 5 | 0 | 5.60E-05 | |
| 5 | 0 | 5 | 5 | 0 | 4.34E-05 | |
| 6 | 5 | 5 | 5 | 0 | 5.60E-05 | |
| 7 | 0 | 5 | 0 | 5 | 3.74E-05 | |
| 8 | 5 | 5 | 0 | 5 | 3.15E-05 | |
| 9 | 0 | 0 | 0 | 5 | 3.72E-05 | |
| 10 | 5 | 0 | 0 | 5 | 3.15E-05 | |
| 11 | 0 | 0 | 5 | 5 | 3.01E-05 | |
| 12 | 5 | 0 | 5 | 5 | 3.77E-05 | |
| 13 | 0 | 5 | 5 | 5 | 3.05E-05 | |
| 14 | 5 | 5 | 5 | 5 | 3.81E-05 | |
| 15 | 0 | 5 | 0 | 0 | 1.32E-07 | |
| 16 | 5 | 5 | 0 | 0 | 1.79E-05 | |
| 17 | 0 | 0 | 0 | 0 | 0 | Delamination of size 50mm at 210mm from left |
| 18 | 5 | 0 | 0 | 0 | 1.80E-05 | |
| 19 | 0 | 0 | 5 | 0 | 4.36E-05 | |
| 20 | 5 | 0 | 5 | 0 | 5.66E-05 | |
| 21 | 0 | 5 | 5 | 0 | 4.36E-05 | |
| 22 | 5 | 5 | 5 | 0 | 5.66E-05 | |
| 23 | 0 | 5 | 0 | 0 | 1.33E-07 | |
| 24 | 5 | 5 | 0 | 0 | 1.80E-05 | |
| 25 | 0 | 0 | 0 | 5 | 3.74E-05 | |
| 26 | 5 | 0 | 0 | 5 | 3.16E-05 | |
| 27 | 0 | 0 | 5 | 5 | 3.74E-05 | |
| 28 | 5 | 0 | 5 | 5 | 3.95E-05 | |
| 29 | 0 | 5 | 5 | 5 | 3.29E-05 | |
| 30 | 5 | 5 | 5 | 5 | 3.98E-05 | |
| 31 | 0 | 5 | 0 | 5 | 3.76E-05 | |
| 32 | 5 | 5 | 0 | 5 | 3.16E-05 | |

In order to show the dominant factors graphically, the corresponding half normal probability plot (Figure 4.10) was constructed; Figure 4.10 recommends considering AC as the last dominant factor. Next, a standard ANOVA analysis was performed (Table 4.10) and results suggested ignoring the effect of factor AC and D with a statistical significance level of $\alpha$=0.01. Nevertheless, recalling the percentage contributions in Table 4.9 it is clear that the top two main factors are C and CD, as was the case for the point-to-point analysis. However in the point-to-point analysis, D was also highly significant at the selected nodes, whereas in the integral method it shows much less overall contribution. This would mean that *the number and locations of sensors during SHM can vary the sensitivity of the prediction results to particular noise/uncertainty factors*, such as D (the loading angle offset). Figure 4.11 illustrates the main and interaction plots for the factors A, C, and D. From Figure 4.11.a, unlike in the point-to-point analysis (Figure 4.9), the slope of every main factor, including D, is positive in the current analysis. This indicates that increasing each noise factor magnitude also increases the deviation of the structure's overall response from the base model. The interaction plot for C and D in Figure 4.11.b confirms an overall high interference of these two main factors; which is interesting because according to Figures 4.9 (d-f) the lines of these factors cross each other mainly at the first node. This suggests that only for a few number of points near the left constraint point the interactive effect of noise factors (here C and D) may be notable; A potential hypothesis from these results for a future work would be: *the more dispersed the positions of the sensors, perhaps the less likelihood of imposing interactive effects of noise (uncertainty) factors on the overall prediction results*.

**Table 4.9.** Percentage contributions of the factors from the integral analysis in Table 4.8; all values are in %; the bold numbers refer to the high contributions.

| Factors | Structure's health state | |
|---|---|---|
| | Healthy | Damaged |
| A | **6.55** | **5.32** |
| B | 0.00 | 0.02 |
| C | **41.03** | **46.99** |
| D | **2.39** | **4.02** |
| AB | 0.00 | 0.03 |
| AC | 0.42 | 0.19 |
| AD | **5.20** | **6.35** |
| BC | 0.00 | 0.03 |
| BD | 0.00 | 0.03 |
| CD | **42.21** | **35.46** |
| ABC | 0.00 | 0.04 |
| ABD | 0.00 | 0.04 |
| ACD | 2.19 | 1.43 |
| BCD | 0.00 | 0.03 |
| ABCD | 0.00 | 0.04 |

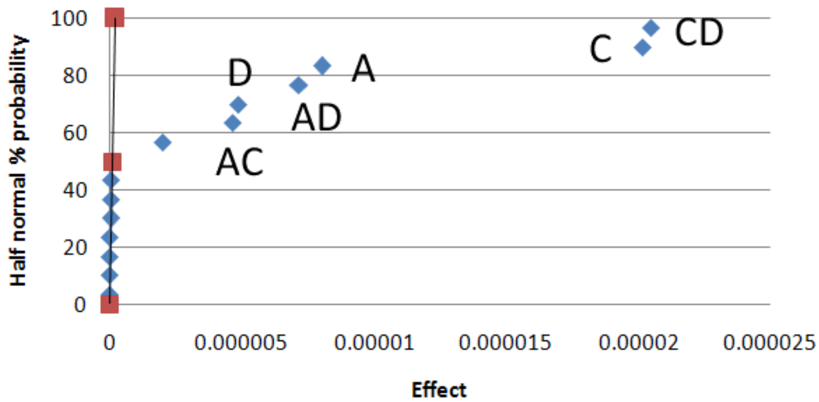


**Figure 4.10.** Half normal probability plot – integral approach (Healthy structure).

**Table 4.10.** Results of ANOVA analysis based on dominant factors in Figure 4.10 for the integral approach (by Minitab statistical software).

| Source | DF | Seq SS | Adj SS | Adj MS | F | P |
|---|---|---|---|---|---|---|
| A | 1 | 260.75 | 260.75 | 260.75 | 26.90 | 0.001 |
| C | 1 | 1632.87 | 1632.87 | 1632.87 | 168.43 | 0.000 |
| D | 1 | 95.06 | 95.06 | 95.06 | 9.81 | 0.012 |
| A*C | 1 | 16.87 | 16.87 | 16.87 | 1.74 | 0.220 |
| A*D | 1 | 206.82 | 206.82 | 206.82 | 21.33 | 0.001 |
| C*D | 1 | 1679.97 | 1679.97 | 1679.97 | 173.28 | 0.000 |
| Error | 9 | 87.25 | 87.25 | 9.69 | | |
| Total | 15 | 3979.60 | | | | |

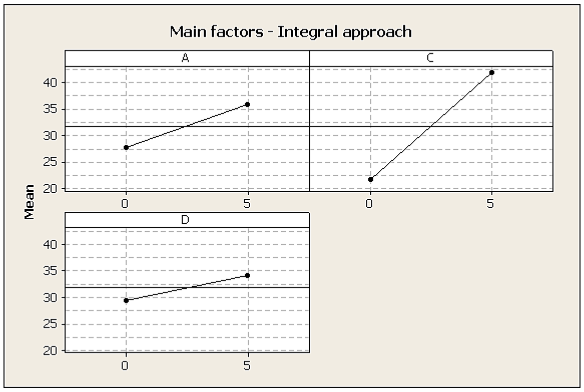


(a)

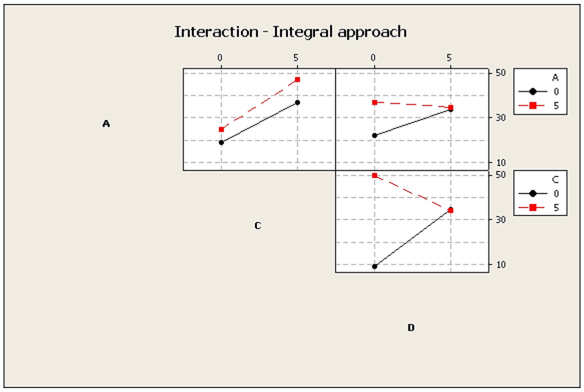

(b)

**Figure 4.11.** Main factor and interaction plots for the integral analysis approach (considering factors A, C, D and their interactions).

## 4.5. Summary of case study 1

Two different approaches, a point-to-point analysis and an integral analysis, were considered in a case study on the potential effect of uncertainty factors on SHM predictability in composite structures. The point–to-point (discrete) analysis is more similar to real application where the number of sensors is normally limited and the SHM investigators can only rely on the data extracted at specific sensor locations. The integral approach, on the other hand, calculates the area of a continuous strain distribution and, hence, simulates an ideal situation where there are a very large number of sensors embedded inside the structure. The comparison of the two approaches showed the impact of increasing the number of strain measurement points on the behavior of the prediction model and the associated statistical results. Namely, for all sensor positions considered in the point-to-point (discrete) analysis, the main factors were the misalignment of fibers in the hull and the loading angle offset, but for the integral (continuous) approach, the aggregation of smaller factors over the bond line resulted in increasing significance of other parameters such as overlaminate misalignment angle and its interaction with existing dominant factors. However the top contributing factors remained the same between the two analyses, indicating that increasing the number of sensors does not eliminate the noise effects from fabrication such as misalignment of fibers and loading angle offset. Another conclusion from this case study was that, statistically, there was no sign of significant deviation in contribution patterns of factors between the healthy and damaged structure. This suggests that different sensor positioning scenarios may change the sensitivity of the response to noise factors but the deviation would be regardless of the absence or presence of delamination. In other words the relative importance of studied noise factors would be nearly identical in the healthy and damaged structure.

In summary, results suggested that that the absolute effect of individual manufacturing uncertainty factors in deviating the structure’s response can be as high as that caused by the presence of delamination itself when compared to the response of the healthy case, even in the absence of misalignment errors. Hence, a basic SHM damage prediction system under the presence of pre-existing manufacturing/testing errors may lead to wrong decisions or false alarms. A remedy to this problem is the development of new stochastic SHM tools, as is the main motivation of the current research and will be fulfilled in Chapters 6-7.

# Chapter 5

# Proof of Concept Study 2: Effect of Uncertainty in SHM of a Multi-layer Composite Airfoil

## Chapter preview

In this chapter, as a second case study which will also be the basis for the rest of this thesis, a composite symmetric airfoil is statistically investigated to analyze the impact of manufacturing uncertainty *in the form of ply thickness variation* on the SHM system robustness under tensile loading (to mimic the loading condition of the upper half of an aircraft wing). First, only a few damage scenarios (damages at leading edge, trailing edge and quarter chord) are considered next to the undamaged (healthy) structure scenario. For each of these four scenarios, five random variations of ply thickness are imposed in a FE model. Then, variations of strain measurements at sensor locations are investigated to statistically determine the impact of thickness variation compared to the presence of damage itself. Results will indicate that at only for 4 sensors the abnormalities in strain measurement may be directly correlated to the damage and the rest of the sensors are unable to report damage at the presence of (manufacturing) thickness variation. Next, a more comprehensive damage database is established by running 162 damage scenarios (i.e., several damage locations and sizes). This time the DOE analysis will surprisingly indicate that no sensor is able to distinguish between the presence of damage and thickness variation, owing to the very large amount of noise scenarios. This, in turn, proves the outmost importance of ensuring the universality of a given damage database (representativeness of reality) for SHM training purposes.

## 5.1. Introduction to case study 2

As discussed earlier in the dissertation, the performance and robustness of the SHM system [1-4] in any field should be examined in the presence of noise and uncertainty of input parameters. The earlier study [5] (Chapter 4) using numerical simulations of a composite T-joint [6] showed that the inclusion of sources of uncertainty in a SHM can be crucial, specifically since the variation caused in the response of a structure due to uncertainty sources could be as large as those by the damage itself. Another conclusion in that study was that, statistically, the relative significance of noise factors could be nearly identical in the healthy and damaged structures.

The aim of the present chapter is to investigate the importance of considering uncertainty due to materials/manufacturing errors in another benchmark composite structure and loading condition: NACA-0012 airfoil under tensile loading (Figure 5.1). This airfoil is a sandwich structure containing a 3 mm thick PVC foam, reinforced with E-glass and carbon woven fabrics (Table 5.1). The prototype is wet hand laid up and vacuum bagged and elastic material properties of its components were estimated based on [7-9] (Table 5.2). The structure was first tested under a pre-defined set of different delamination scenarios (more details in Section 5.3) under static tensile loading. Then, a finite element (FE) model of the test was established, validated, and used for further analysis as a virtual experimental tool to create more damage scenarios with varying ply thicknesses (mimicking a manufacturing error). Eventually, via ANOVA analyses, statistical significances of the uncertainty factor on SHM predictions have been captured. An advantage of this study, compared to earlier modeling works such as [5] (Chapter 4), is that the range of uncertainty was directly estimated based on random repeats of actual/physical tests. In this study we assumed that all the uncertainties have been caused by thickness variation. This assumption is not valid for all real applications, but since hand lay-up process was used herein, and to reduce the complexity of the problem, the assumption would be reasonable.

**Table 5.1.** Stacking sequence of the airfoil and nominal ply thicknesses

| Layer no. | Type | Density (gr/m$^{2}$) | ~ Thickness (mm) |
|---|---|---|---|
| 1 | E-glass (woven) | 50 | 0.06 |
| 2 | E-glass (woven) | 200 | 0.2 |
| 3 | E-glass (woven) | 200 | 0.2 |
| 4 | Carbon (woven) | 200 | 0.2 |
| 5 | PVC foam | 80 | 3.0 |
| 6 | Carbon (woven) | 200 | 0.2 |
| 7 | E-glass (woven) | 200 | 0.2 |
| 8 | E-glass (woven) | 200 | 0.2 |
| 9 | E-glass (woven) | 50 | 0.06 |

**Table 5.2.** The material properties used for modeling the airfoil plies (x- index refers to the main fiber direction; woven fabrics in FE simulations were modeled as a cross-ply laminate)

| | Young's Modulus (MPa) | Poisson's Ratio | Shear Modulus (MPa) |
|---|---|---|---|
| CFRP | $E_x = 62000$<br>$E_y = 4800$<br>$E_z = 4800$ | $\nu_{xy} = 0.22$<br>$\nu_{xz} = 0.22$<br>$\nu_{yz} = 0.30$ | $G_{xy} = 3270$<br>$G_{xz} = 3270$<br>$G_{yz} = 1860$ |
| GFRP | $E_x = 21000$<br>$E_y = 7000$<br>$E_z = 7000$ | $\nu_{xy} = 0.26$<br>$\nu_{xz} = 0.26$<br>$\nu_{yz} = 0.30$ | $G_{xy} = 1520$<br>$G_{xz} = 1520$<br>$G_{yz} = 2650$ |


**Figure 5.1.** The composite airfoil sample under tension at 1 mm/min rate (no pre-stress)

Before proceeding with the finite element and statistical analysis, the production process of the test samples is briefly presented here. As mentioned earlier, the considered airfoil is NACA0012 which is the most common symmetric profile in aviation industry. A 9 layer sandwich panel with one middle PVC foam of 3mm thickness, two layers of 200 gr/m$^2$ woven carbon and 4 layers of 200 gr/m$^2$ and two layers of 50 gr/m$^2$ woven glass are used to reinforce the middle foam. Epolam 2015 has been used as the matrix (Figure 5.2). The step-by-step process used for sample fabrication is as follows:

- Make the mold.
  The airfoil profile is cut off from a piece of balsa wood, and then attached to the yonolit foam to cut the profile out of the original cube (Figure 5.2(a-b)). Five layers of 200 gr/m$^2$ woven glass were used to reinforce the mold and make sure that vacuum pressure will not distort the desired shape of the mold (Figure 5.2(c-d)).
- Form the PVC foam to fit to the airfoil geometry (Figure 5.2(e)).
- Lay up the layers of the airfoil (Figure 5.2(f)) and put the sample covered by dacron and breather in vacuum bag (Figure 5.2(g)).
- Make the load transmitter laminate. Five layers of 200 gr/m$^2$ woven glass were used as the basis for the load transmission. Take the mold out of the airfoil sample (Figure 5.2(h)).
- Cut off the airfoil geometry from the laminate and attach them by aerozil powder in epoxy resin (Figure 5.2(i)).
- Layup supporting glass layers. 6 layers of 200 gr/m$^2$ woven glass were used to support the aerozil adhesive and make sure uniform load transmission to the airfoil.

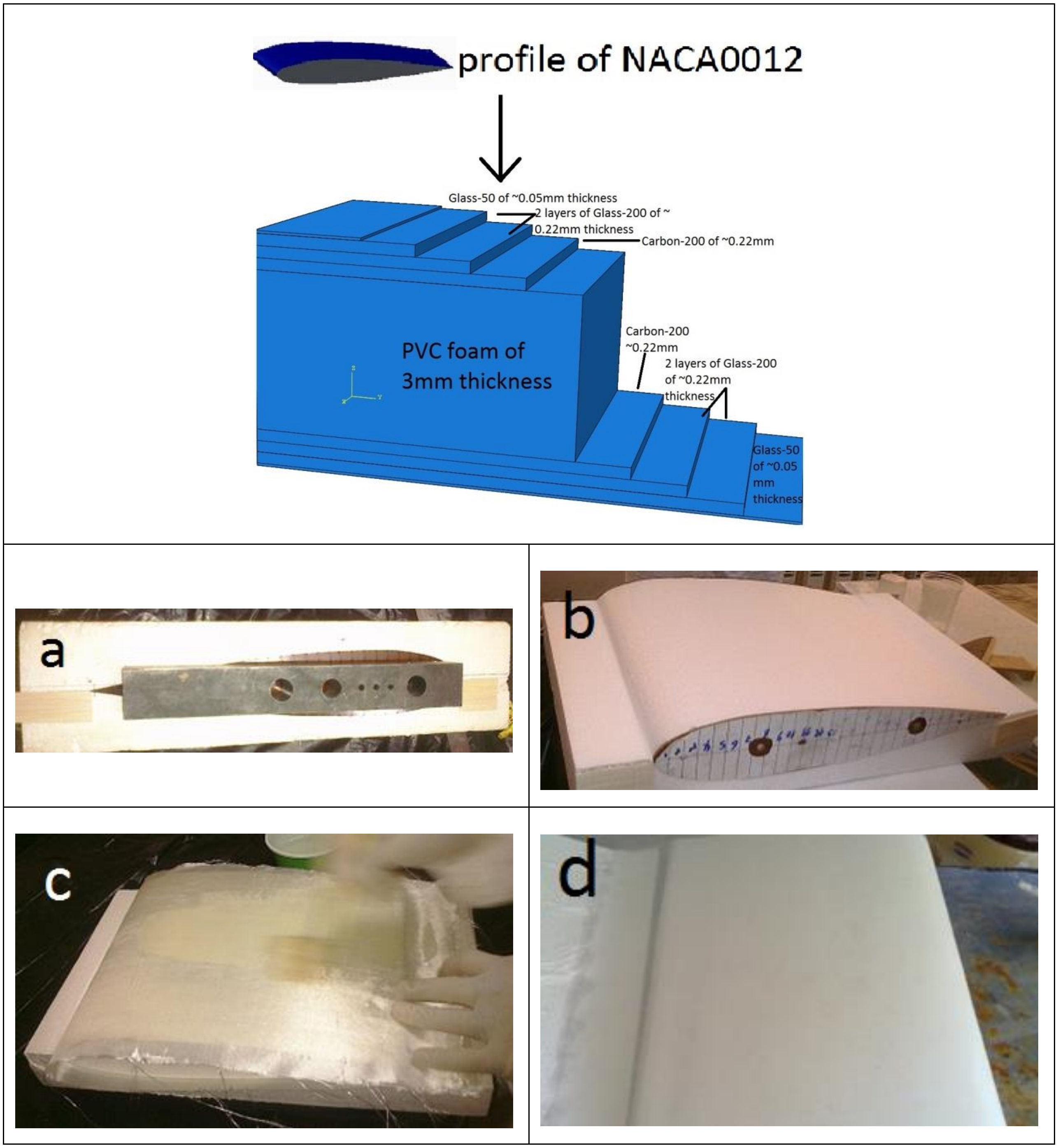
profile of NACA0012
Glass-50 of ~0.05mm thickness
2 layers of Glass-200 of ~
0.22mm thickness
Carbon-200 of ~0.22mm
PVC foam of
3mm thickness
Carbon-200
~0.22mm
2 layers of Glass-200
of ~0.22mm
thickness
Glass-50
of ~0.05
mm
thickness
a
b
c
d

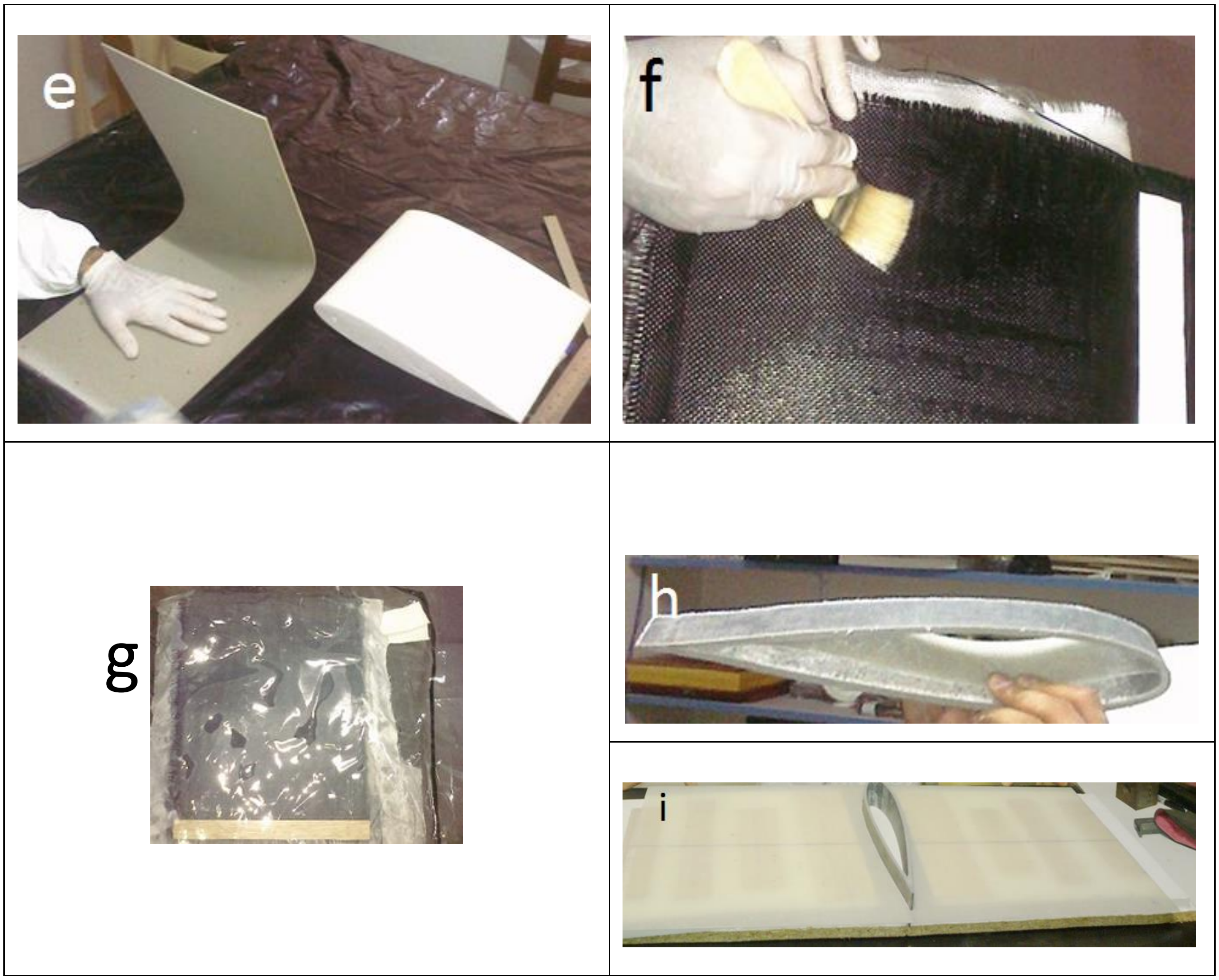


**Figure 5.2.** Stacking sequence of the airfoil and its nominal ply thicknesses, along with the step by step procedure used for making the airfoil samples

## 5.2. Tension experiments and finite element model development for a few number of damage scenarios

Over twenty different types of defect have been reported in the literature for composite structures [10-18]. Here, the focus is on the most common defect mode in sandwich structures which is delamination. Delamination itself, considering the origin of its initiation, may be caused by low energy impact, stress concentration at free surfaces, stress concentration due to tabbed joints, machining, poor curing process, etc. In this work, artificial delaminations were embedded into the test samples by inserting a waxed thin plate between the corresponding plies during the airfoil prototyping process, regardless of the cause of such damage mode. Five different damage scenarios (delamination location/configuration) were initially considered as illustrated in Figure 5.3. Figures 5.4, 5.5, and 5.6, respectively, the force-displacement behavior of the airfoils with no damage, damage at the leading edge versus that at the trailing edge, damage at the quarter chord up to the PVC foam versus damage at the quarter chord down to the PVC foam. Figure 5.4 indicates a lack of performance reputability of the structure under the same manufacturing process (which can be attributed to uncontrollable factors/noise during fabrication; here thickness non-uniformity due to applying resin rich or starvation regions during manual lay-up). Also from Figure 5.5 it is evident that the structure's stiffness in the presence of damage closer to the trailing edge (with a sharp geometrical corner) is reduced.

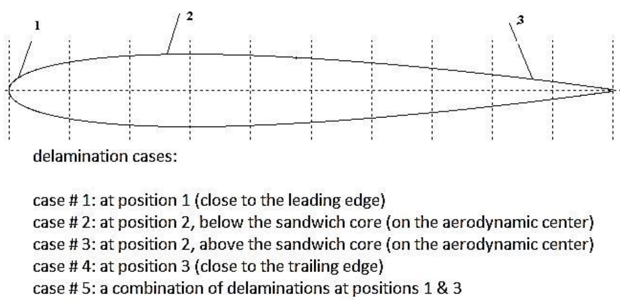


**Figure 5.3.** The embedded damage scenarios during prototyping of the airfoil

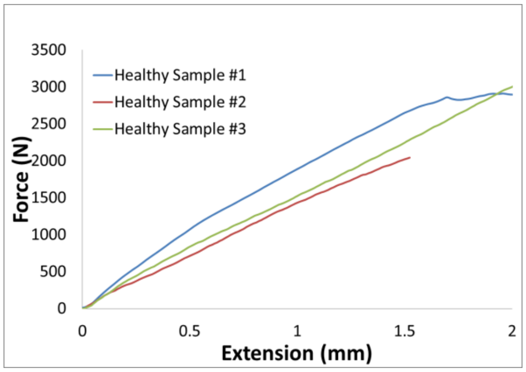


**Figure 5.4.** Repeats of the tensile test for three different airfoil samples with no embedded delamination (healthy case)

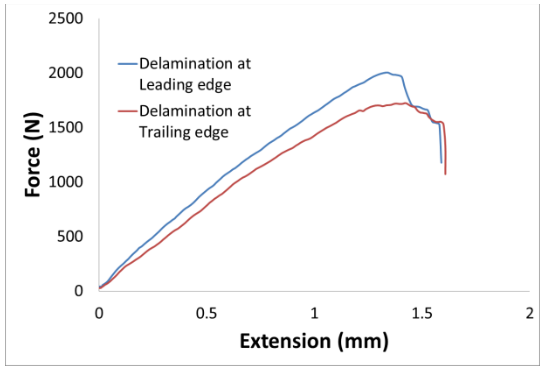


**Figure 5.5.** Mean force-displacement response for two damage scenarios: damage at the leading edge versus damage at the trailing edge

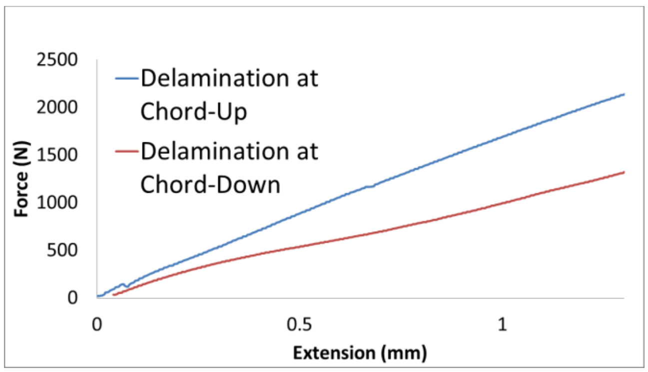


**Figure 5.6.** Mean force-displacement response for two damage scenarios: damage at the quarter chord up to the PVC foam versus damage at quarter chord down to the PVC foam

The tensile test results were then employed to establish and validate a FE model of the structure (Figure 5.7). Figures 5.8 and 5.9 compare the force-displacement curves corresponding to the samples with no damage (healthy scenario) and delamination at the trailing edge based on the average data obtained from the experiments and the finite element model. Good agreement (with a mean residual error of 6%) between the experiments and numerical simulations was obtained and allowed the further use of the developed FE code in subsequent sections as a virtual experimental tool to create more damage scenarios and uncertainty simulations. It should be mentioned that in Figure 5.8 experimental curves correspond to the average behavior observed for different samples subjected to the same loading. It will be shown later (Figure 5.10) that with embedding the uncertainty in the FE model, the upper and lower limits of the scatter in the experimental data (i.e., the three repeats of the test) can also be captured.

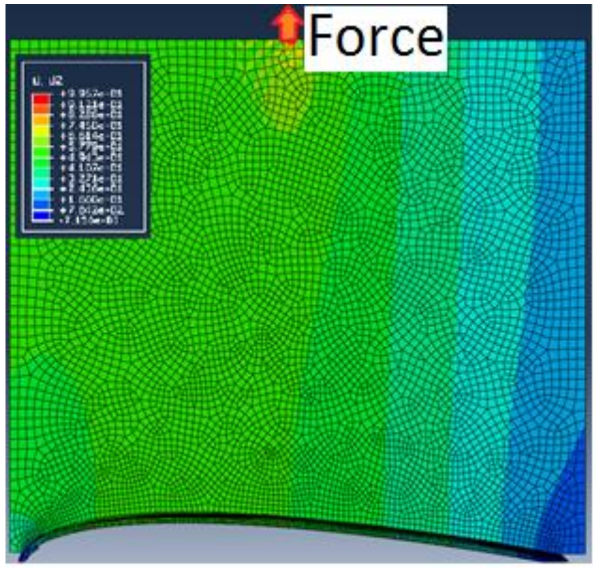


**Figure 5.7.** Sample result from the finite element simulation of the structure under tensile loading

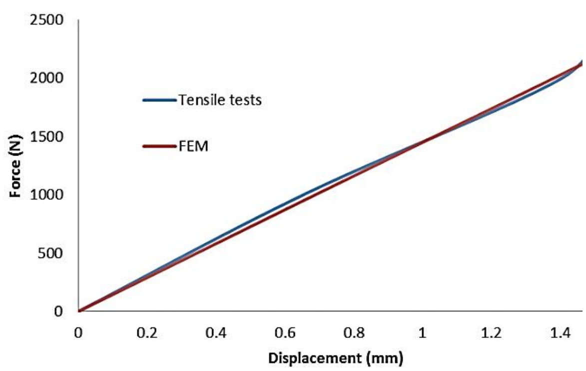


**Figure 5.8.** Comparing the average experimental and numerical force-displacement curves for the airfoil with no damage

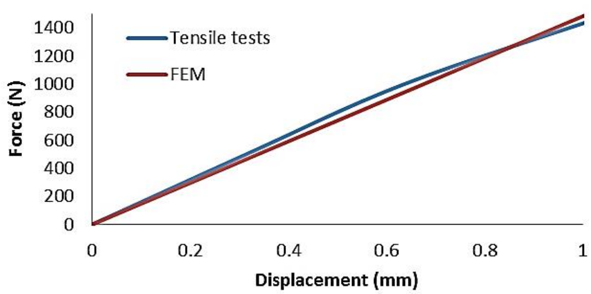


**Figure 5.9.** Comparing the average experimental and numerical force-displacement curves for the airfoil with delamination at the trailing edge (position # 3 as shown in Figure 5.3)

Table 5.3 shows the displacement variations at different loading values for the tested airfoils with no delamination (i.e., using data in Figure 5.4). We assume that these variations in the structure's global response have been equivalently caused by variations in thickness of different plies (carbon 200 gr/m$^3$ and glass 200 gr/m$^3$; both below and above the PVC foam), which is common during hand lay-up processes. Subsequently, the FE code was used with an inverse method to determine a reasonable thickness range for each of the above- mentioned plies to cover at least 60% of experimental data scatter (Table 5.4). The lower and upper thickness limits provided in Table 5.4 were then used to generate random values (assuming a uniform distribution) for each ply thicknesses in the subsequent stochastic simulations. Figure 5.10 shows the example of simulated response variation via the randomness in ply-2 thicknesses versus that of the actual tensile tests on the healthy structure. At first, the proposed thickness variation range might seem too high, but comparing these values with the thickness measurements conducted on flat laminates under same 'hand lay-up' production process suggested the reasonability of the proposed upper and lower bounds for numerical analysis.

**Table 5.3.** Variation of displacement observed at different load magnitudes for different samples using experimental data in Figure 5.5

| Load | min Disp. | max Disp. | Difference % | Mean (mm) |
|---|---|---|---|---|
| 500 | 0.222 | 0.349 | 36.3 | 0.285 |
| 1000 | 0.465 | 0.692 | 32.8 | 0.579 |
| 1500 | 0.757 | 1.058 | 28.4 | 0.907 |
| 2000 | 1.072 | 1.479 | 27.5 | 1.275 |
| 2500 | 1.403 | 1.668 | 15.9 | 1.535 |

**Table 5.4.** Calculated thickness ranges (in cm) of different composite layers to cover about 60% of the variation observed in the experiments in Figure 6.5.

| | **t2 - Glass200 - below the PVC foam - other thickness values are assumed to be nominal values** | | | |
|---|---|---|---|---|
| | t2 - min | Displacement (t2 - min) | t2 - max | Displacement (t2 - max) |
| Load | | | | |
| 500 | 0.18 | 0.3442 | 0.4 | 0.2812 |
| 1000 | 0.18 | 0.6885 | 0.4 | 0.5625 |
| 1500 | 0.18 | 1.033 | 0.4 | 0.8437 |
| 2000 | 0.18 | 1.377 | 0.4 | 1.125 |
| 2500 | 0.18 | 1.511 | 0.4 | 1.406 |
| | **t3 - Carbon200 - below the PVC foam - other thickness values are assumed to be nominal values** | | | |
| | t3 - min | Displacement (t3 - min) | t3 - max | Displacement (t3 - max) |
| Load | | | | |
| 500 | 0.2 | 0.3441 | 0.4 | 0.2807 |
| 1000 | 0.2 | 0.6883 | 0.4 | 0.5614 |
| 1500 | 0.2 | 1.033 | 0.4 | 0.8421 |
| 2000 | 0.2 | 1.378 | 0.4 | 1.123 |
| 2500 | 0.2 | 1.59 | 0.4 | 1.403 |
| | **t4 - Carbon200 - above the PVC foam - other thickness values are assumed to be nominal values** | | | |
| | t4 - min | Displacement (t4 - min) | t4 - max | Displacement (t4 - max) |
| Load | | | | |
| 500 | 0.16 | 0.3455 | 0.28 | 0.2808 |
| 1000 | 0.17 | 0.6919 | 0.28 | 0.5616 |
| 1500 | 0.17 | 1.038 | 0.28 | 0.8424 |
| 2000 | 0.17 | 1.384 | 0.28 | 1.123 |
| 2500 | 0.2 | 1.59 | 0.28 | 1.404 |
| | **t5 - Glass200 - above the PVC foam - other thickness values are assumed to be nominal values** | | | |
| | t5 - min | Displacement (t5 - min) | t5 - max | Displacement (t5 - max) |
| Load | | | | |
| 500 | 0.16 | 0.3466 | 0.3 | 0.2803 |
| 1000 | 0.16 | 0.6932 | 0.3 | 0.5605 |
| 1500 | 0.16 | 1.04 | 0.3 | 0.8408 |
| 2000 | 0.16 | 1.386 | 0.3 | 1.121 |
| 2500 | 0.2 | 1.59 | 0.3 | 1.401 |

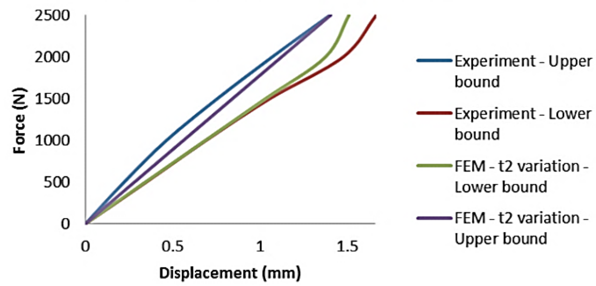


**Figure 5.10.** Upper and lower limits of the scatter in the experimental data vs. those captured by the stochastic FE model using t2-tickness variation

## 5.3. Sensitivity analysis of damage vs. uncertainty for a few number of damage scenarios

As addressed in Section 5.2, the main purpose of this case study was to systematically determine the importance of manufacturing uncertainty sources, here in the form of ply thickness variations, on the reliability of the damage signature database (DSB) that can be used in future chapters to develop a robust strain-based SHM tool for the NACA0012 airfoil. In this regard, using the identified ply thickness variations in Table 5.4 (as input), the corresponding variations of the strain distribution (as output) on the lower surface of the airfoil was statistically analysed to determine the exact amount of disturbance caused by the thickness variation compared to that caused by the presence of delamination at different locations (delamination length in all cases was taken to be 2 cm). Four different cases were considered: model with no delamination (healthy) and models with single delamination at the leading edge, quarter chord below the PVC foam and the trailing edge.  The internal chord of the 3D airfoil is 31cm and the external chord is 33.5cm. Fifteen positions along the lower surface of the airfoil were considered as sensing points to estimate an accurate (continuous) strain distribution pattern. Figure 5.11 shows the corresponding sensor points at which the horizontal strain values have been collected in each FE simulation. Table 5.5 shows randomly selected thickness values used for different plies in the stochastic FE simulations (note that each ply thickness has an upper and lower bound as indicated in Table 5.4). For each damage scenario, these stochastic repeats (R1 to R5) were simulated and strain values for sensors 1-15 were collected (e.g., Figure 5.12) and used for statistical analysis.

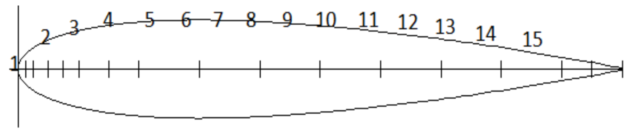


**Figure 5.11.** The position of virtual sensors 1-15 (i.e., the strain measurement nodes in the FE model)

**Table 5.5.** Randomly selected thickness values for different plies

| | Glass 200 below PVC foam | Carbon 200 below PVC foam | Glass 200 above PVC foam | Carbon 200 above PVC foam |
|---|---|---|---|---|
| Repeats | t2 (cm) | t3 (cm) | t4 (cm) | t5 (cm) |
| R1 | 0.31 | 0.29 | 0.21 | 0.29 |
| R2 | 0.38 | 0.21 | 0.20 | 0.21 |
| R3 | 0.23 | 0.26 | 0.19 | 0.20 |
| R4 | 0.38 | 0.31 | 0.24 | 0.27 |
| R5 | 0.23 | 0.39 | 0.21 | 0.26 |

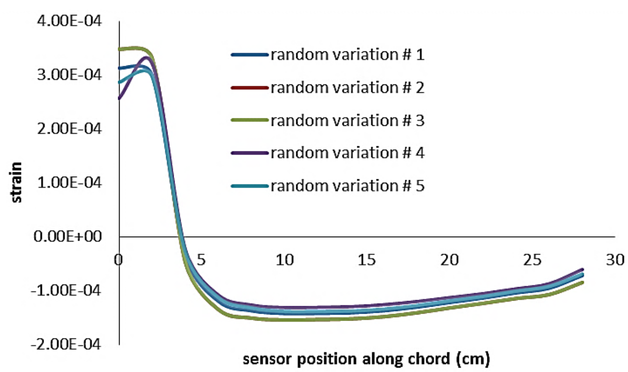


**Figure 5.12.** Strain distribution along the lower surface of the healthy airfoil for the five random repeats using thickness values in Table 5.5

Table 5.6 shows the ensuing strain values at sensor 1, followed by the corresponding two-way analysis of variance (ANOVA). The mean sum of squares (variance) of the strain response due to damage scenarios at this sensor location is 2.448E-09 which is about 1 order of magnitude less than the corresponding variance caused by thickness variation (1.975E-08). Therefore, the ANOVA analysis here suggests that for this sensor point the effect of variation of the ply thickness (manufacturing uncertainty) is at least one order of magnitude more significant compared to the variation caused by the presence or the position of delamination. This conclusion can be further proven according to the p-values for the damage and thickness variation treatments in Table 5.6: the p-value for thickness variation is close to zero (0.003167), while the p-value for damage scenarios is 0.466137. Hence, with a statistical significance level of $\alpha$=5% (or a 95% confidence level), it can be inferred that only thickness variation is the significant factor for this sensor and it is not sensitive to damage variation.

**Table 5.6.** Strain values and the corresponding ANOVA analysis at sensor 1 under different damage scenarios and random repeats according to Table 5.5 (by Minitab statistical software).

| Damage scenario | Repeat#1 | Repeat#2 | Repeat#3 | Repeat#4 | Repeat#5 |
|---|---|---|---|---|---|
| Healthy | 3.13E-04 | 3.48E-04 | 3.48E-04 | 2.57E-04 | 2.87E-04 |
| Leading edge | 3.04E-04 | 5.57E-04 | 4.28E-04 | 2.49E-04 | 2.77E-04 |
| Chord Down | 3.13E-04 | 3.44E-04 | 4.39E-04 | 2.57E-04 | 2.86E-04 |
| Trailing edge | 3.13E-04 | 3.44E-04 | 4.39E-04 | 2.57E-04 | 2.86E-04 |
| **ANOVA for Sensor 1** | | | | | |
| **Source** | SS | Df | MS | F | **P-value** |
| **Damage** | 7.345E-09 | 3 | 2.448E-09 | 0.90762061 | **0.466137** |
| **Thickness** | 7.901E-08 | 4 | 1.975E-08 | 7.32279813 | **0.003167** |
| Error | 3.237E-08 | 12 | 2.697E-09 | | |
| Total | 1.187E-07 | 19 | | | |

Next, the above statistical analysis was repeated for all the 15 sensors. For some sensors such as sensors 2 to 5, the analysis resulted in an opposite conclusion to that of sensor 1: the damage in these sensors was statistically significant and the thickness variation acts as an insignificant manufacturing noise with a p-value greater than 5%. For instance, from Table 5.7, at sensor 2 the p-value calculated with respect to the variance caused by the damage scenarios is 0.0004 which indicates a very significant sensitivity of this sensor location to damage factor (even more than sensor 1), while the high p-value of 0.1129 observed for the thickness variation effect shows that this sensor location may be reliably used for DSB training sets during a robust SHM development.

**Table 5.7.** Strain values and the corresponding ANOVA analysis at sensor 2 under different damage scenarios and random repeats according to Table 5.5 (by Minitab statistical software).

| Damage scenario | Repeat#1 | Repeat#2 | Repeat#3 | Repeat#4 | Repeat#5 |
|---|---|---|---|---|---|
| Healthy | 3.00E-04 | 3.31E-04 | 3.31E-04 | 3.21E-04 | 2.97E-04 |
| Leading edge | 1.72E-04 | 3.35E-04 | 1.34E-04 | 2.14E-04 | 1.55E-04 |
| Chord Down | 3.08E-04 | 3.37E-04 | 3.30E-04 | 3.28E-04 | 3.05E-04 |
| Trailing edge | 3.08E-04 | 3.37E-04 | 3.30E-04 | 3.28E-04 | 3.05E-04 |
| **ANOVA for Sensor 2** | | | | | |
| **Source of Variation** | SS | df | MS | F | **P-value** |
| **Damage** | 5.19E-08 | 3 | 1.73E-08 | 13.10 | **0.00** |
| **Thickness** | 1.24E-08 | 4 | 3.104E-09 | 2.35 | **0.11** |
| Error | 1.58E-08 | 12 | 1.32E-09 | | |
| Total | 8.02E-08 | 19 | | | |

From the summary of all sensitivity analyses for the few number of scenarios tested in Table 5.8, it can be seen that sensors 3 and 5 are similarly robust against thickness variation and most sensitive to the presence and location of damage. At sensor 4, the damage and thickness factors are comparably of the same statistical significance which would make the weight of this sensing point less (but still acceptable) for damage identification. Sensors 6-15 show a very high p-value with respect to the damage factor and hence may receive less weight during SHM training.

**Table 5.8.** Summary of all sensitivity analyses for sensors 1-15 against the damage and thickness variation factors (by Minitab statistical software).

| | Sources of Variation | F | P-values | Sensor is MORE sensitive to |
|---|---|---|---|---|
| **Sensor 1** | Damage status | **0.9076** | **0.4661** | Thickness variation |
| | Thickness variation | **7.3228** | 0.0032 | |
| **Sensor 2** | **Damage status** | **13.1039** | **0.0004** | **Damage** |
| | Thickness variation | **2.3508** | 0.1129 | |
| **Sensor 3** | **Damage status** | **33.4626** | **0.0000** | **Damage** |
| | Thickness variation | **3.7305** | 0.0339 | |
| **Sensor 4** | **Damage status** | **4.6204** | **0.0227** | **Damage** |
| | Thickness variation | **4.6260** | 0.0172 | |
| **Sensor 5** | **Damage status** | **44.8866** | **0.0000** | **Damage** |
| | Thickness variation | **2.6817** | 0.0830 | |
| **Sensor 6** | Damage status | **0.9286** | 0.4567 | Thickness variation |
| | Thickness variation | **3.1116** | 0.0567 | |
| **Sensor 7** | Damage status | **1.0118** | 0.4214 | Thickness variation |
| | Thickness variation | **3.0952** | 0.0575 | |
| **Sensor 8** | Damage status | **1.0291** | 0.4144 | Thickness variation |
| | Thickness variation | **3.1273** | 0.0560 | |
| **Sensor 9** | Damage status | **1.0403** | 0.4099 | Thickness variation |
| | Thickness variation | **3.1583** | 0.0545 | |
| **Sensor 10** | Damage status | **1.0316** | 0.4134 | Thickness variation |
| | Thickness variation | **3.1322** | 0.0557 | |
| **Sensor 11** | Damage status | **1.0091** | 0.4225 | Thickness variation |

| | | | | |
|---|---|---|---|---|
| | Thickness variation | **3.0732** | 0.0586 | |
| **Sensor 12** | Damage status | **0.9971** | 0.4274 | Thickness variation |
| | Thickness variation | **3.0782** | 0.0584 | |
| **Sensor 13** | Damage status | **1.0767** | 0.3958 | Thickness variation |
| | Thickness variation | **3.3397** | 0.0467 | |
| **Sensor 14** | Damage status | **1.1128** | 0.3822 | Thickness variation |
| | Thickness variation | **4.0818** | 0.0258 | |
| **Sensor 15** | Damage status | **0.8883** | 0.4750 | Thickness variation |
| | Thickness variation | **7.2305** | 0.0033 | |

## 5.4. ANOVA analysis for a comprehensive Damage Signature Database (DSD)

This section is devoted to a more comprehensive investigation into the effect of ply thickness variation on the robustness of strain readings from the airfoil samples introduced earlier in this chapter. Similar to Section 5.3, the technique of Analysis of Variance (ANOVA) has been adopted to compare the noises caused from different sources; namely, the thickness variation and the damage location and size variation.

ANOVA analysis in Section 5.3 concluded that among the 15 distributed sensors on the lower surface of the airfoil only sensors 2 through 5 are capable of detecting damage and all the other sensors are disturbed by the changes in thickness of corresponding plies from one simulation to the next one. However, the fact that this conclusion was only based on a few number of damage scenarios (namely one healthy airfoil and three damaged airfoils with a defect of constant size at leading edge, trailing edge and quarter chord) necessitates further validation. Therefore, in this section, a much larger number (166) of damage scenarios were developed considering delaminations with different lengths, starting from ~1.5cm to ~4.5cm, and at different locations all between the lower carbon ply and the middle PVC foam for the same NACA0012 profile airfoil with internal chord of 31cm and the external chord of 33.5cm. Figures 5.13 (a) to (d) illustrates a general schematic of example delaminations of different lengths and locations as used in the damage signature database (DSD) of size 166. It is to note that in each individual damaged airfoil scenario in the DSD, only one delamination (e.g., one size, one location from Figure 5.14) has been implemented).

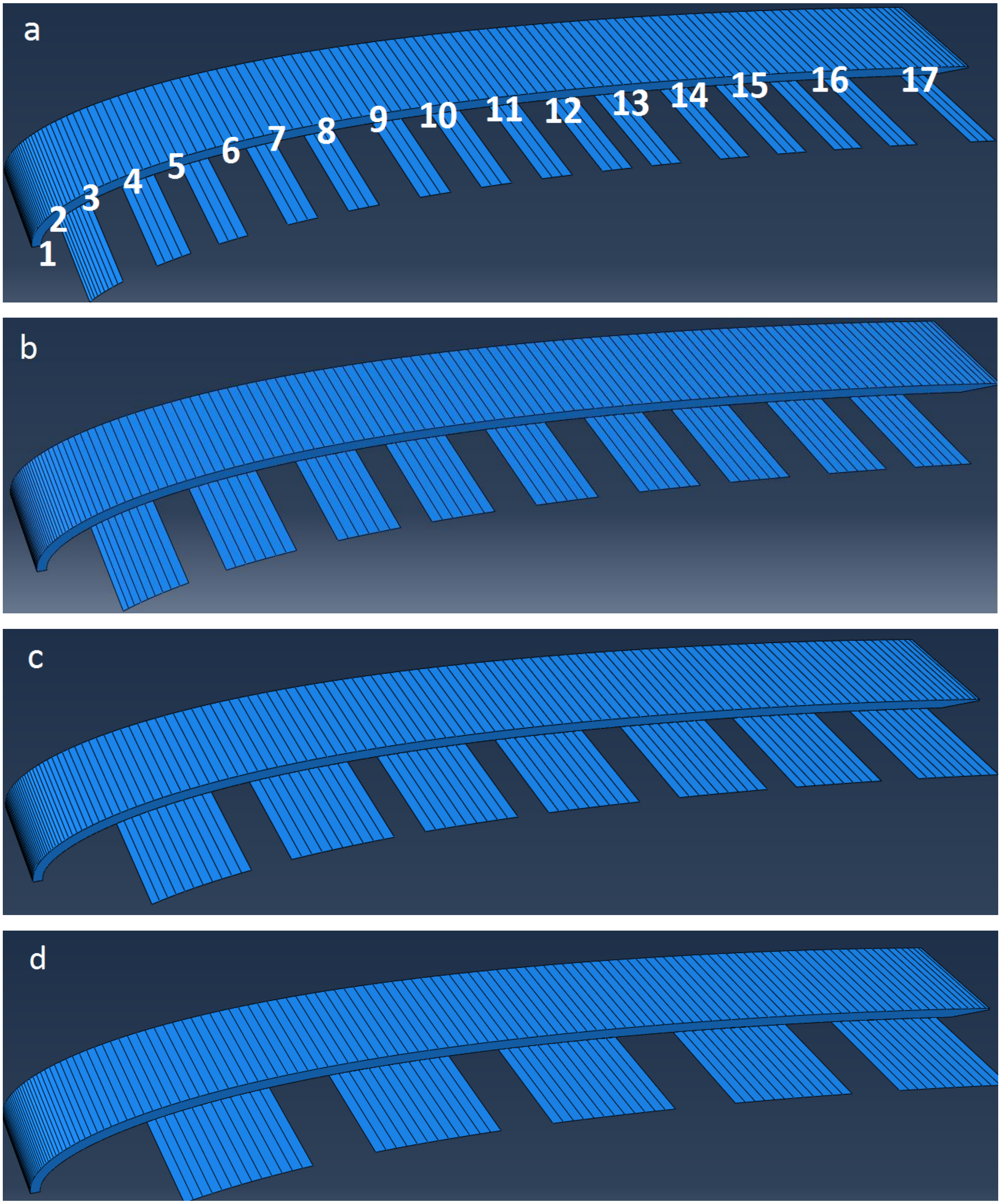


**Figure 5.13.** Sample delamination with different lengths plotted adjacent to the PVC foam in ABAQUS model of the airfoil: (a) ~1cm delamination, (b) ~2cm delamination, (c) ~3cm delamination and (d) ~4cm delamination

The material properties used for FE simulations are the same as those in Table 5.2. Also Table 5.9 shows the calculated thickness ranges for different composite plies to mimic the variation observed in actual tensile experiments (Figure 5.10). Unlike the FE stochastic model presented earlier in Section 5.3 where the random thickness values were picked in 60% of the full range (i.e., Table 4-4), in this section the randomness was decided to be further limited to half of this range (in order to mimic a more realistic variation of ply thickness, e.g., when a manufacturer with a more controlled lay-up process is assumed). Also it is noteworthy that here the ply thickness is used as one of the sources of manufacturing noises, where as in practice several other noises (e.g., geometry non-conformities, different operator skills, void content, etc) may be present collectively. Finally, for more accurate strain field predictions, instead of 15 sensor positions (Figure 5.11) that were used in Section 5.3, here 17 sensor positions (Figure 5.13(a)) have been considered. Namely, sensors 1 through 15 have the same position as the ones earlier in Chapter 5 and sensors 16 and 17 were added to have a better insight into the trailing edge behavior of the airfoil. Table 5.10 shows the summary of ANOVA analysis of all these 17 sensors, after running the FE model for the entire (168) scenarios of the DSB. The resulting p-values clearly show that no sensor is now able to merely focus on the damage status as the accuracy of all sensor predictions have been affected by the presence of uncertainty. Also by comparing magnitudes of F-values in Tables 5.8 and 5.10, say for a same sensor 2, it appears that the damage size effect which was included in the second case has caused much higher strain variation than the damage location. As we will see in the subsequent chapters, this observation will in fact render a challenge for some of the proposed SHM methods to predict the damage size as accurately as the damage location.

**Table 5.9.** Calculated thickness ranges (in cm) of different composite layers to cover about 60% of the half the variation observed in the experiments

| Glass 200 below PVC foam | | | | |
|---|---|---|---|---|
| **Load (N)** | Minimum thickness | Displacement at max loading (corresponding to minimum thickness) | Maximum thickness | Displacement at max loading (corresponding to maximum thickness) |
| **1500** | 0.16 | 1.03 | 0.39 | 0.844 |
| **Carbon 200 below PVC foam** | | | | |
| **Load (N)** | Minimum thickness | Displacement at max loading (corresponding to minimum thickness) | Maximum thickness | Displacement at max loading (corresponding to maximum thickness) |
| **1500** | 0.18 | 1.03 | 0.36 | 0.84 |
| **Glass 200 above PVC foam** | | | | |
| **Load (N)** | Minimum thickness | Displacement at max loading (corresponding to minimum thickness) | Maximum thickness | Displacement at max loading (corresponding to maximum thickness) |
| **1500** | 0.17 | 1.038 | 0.28 | 0.84 |
| **Carbon 200 above PVC foam** | | | | |
| **Load (N)** | Minimum thickness | Displacement at max loading (corresponding to minimum thickness) | Maximum thickness | Displacement at max loading (corresponding to maximum thickness) |
| **1500** | 0.15 | 1.04 | 0.3 | 0.84 |

**Table 5.10.** Summary of ANOVA analysis for the comprehensive database (by Minitab statistical software).

| **Sensor 1** | | | | | | |
|---|---|---|---|---|---|---|
| **Source of variation** | SS | df | MS | F | P-value | F crit |
| **Damage size/position** | 865077 | 165 | 8318 | 115 | 0 | 1.28 |
| **Thickness variation** | 779133 | 4 | 194783 | 2713 | 0 | 2.39 |
| **Error** | 29858 | 660 | 71 | | | |
| **Total** | 1674069 | 829 | | | | |
| **Sensor 2** | | | | | | |
| **Source of variation** | SS | df | MS | F | P-value | F crit |
| **Damage size/position** | 4472108 | 165 | 43001 | 1161 | 0 | 1.28 |
| **Thickness variation** | 17495 | 4 | 4373 | 118 | 0 | 2.39 |
| **Error** | 15405 | 660 | 37 | | | |
| **Total** | 4505010 | 829 | | | | |
| **Sensor 3** | | | | | | |
| **Source of variation** | SS | df | MS | F | P-value | F crit |
| **Damage size/position** | 11370306 | 165 | 109329 | 436 | 0 | 1.28 |
| **Thickness variation** | 7636 | 4 | 1909 | 7 | 6.E-06 | 2.39 |
| **Error** | 104200 | 660 | 250 | | | |
| **Total** | 11482144 | 829 | | | | |

**Sensor 4**

| Source of variation | SS | df | MS | F | P-value | F crit |
|---|---|---|---|---|---|---|
| **Damage size/position** | 9377200 | 165 | 90165 | 747 | 0 | 1.28 |
| **Thickness variation** | 10661 | 4 | 2665 | 22 | 0 | 2.39 |
| **Error** | 50177 | 660 | 120 | | | |
| **Total** | 9438039 | 829 | | | | |

**Sensor 5**

| Source of variation | SS | df | MS | F | P-value | F crit |
|---|---|---|---|---|---|---|
| **Damage size/position** | 3250375 | 165 | 31253 | 564 | 0 | 1.28 |
| **Thickness variation** | 9095 | 4 | 2273 | 41 | 0 | 2.39 |
| **Error** | 23039 | 660 | 55 | | | |
| **Total** | 3282510 | 829 | | | | |

**Sensor 6**

| Source of variation | SS | df | MS | F | P-value | F crit |
|---|---|---|---|---|---|---|
| **Damage size/position** | 2196479 | 165 | 21119 | 379 | 0 | 1.28 |
| **Thickness variation** | 11622 | 4 | 2905 | 52 | 0 | 2.39 |
| **Error** | 23126 | 660 | 55 | | | |
| **Total** | 2231228 | 829 | | | | |

**Sensor 7**

| Source of variation | SS | df | MS | F | P-value | F crit |
|---|---|---|---|---|---|---|
| **Damage size/position** | 1372512 | 165 | 13197 | 414 | 0 | 1.28 |
| **Thickness variation** | 8418 | 4 | 2104 | 66 | 0 | 2.39 |
| **Error** | 13245 | 660 | 31 | | | |
| **Total** | 1394176 | 829 | | | | |

**Sensor 8**

| Source of variation | SS | df | MS | F | P-value | F crit |
|---|---|---|---|---|---|---|
| **Damage size/position** | 864235 | 165 | 8309 | 288 | 0 | 1.28 |
| **Thickness variation** | 11253 | 4 | 2813 | 97 | 0 | 2.39 |
| **Error** | 11980 | 660 | 28 | | | |
| **Total** | 887469 | 829 | | | | |

**Sensor 9**

| Source of variation | SS | df | MS | F | P-value | F crit |
|---|---|---|---|---|---|---|
| **Damage size/position** | 399287 | 165 | 3839 | 430 | 0 | 1.28 |
| **Thickness variation** | 8686 | 4 | 2171 | 243 | 0 | 2.39 |
| **Error** | 3708 | 660 | 8 | | | |
| **Total** | 411682 | 829 | | | | |

**Sensor 10**

| Source of variation | SS | df | MS | F | P-value | F crit |
|---|---|---|---|---|---|---|
| **Damage size/position** | 351588 | 165 | 3380 | 417 | 0 | 1.28 |
| **Thickness variation** | 8557 | 4 | 2139 | 264 | 0 | 2.39 |
| **Error** | 3370 | 660 | 8 | | | |
| **Total** | 363516 | 829 | | | | |

**Sensor 11**

| Source of variation | SS | df | MS | F | P-value | F crit |
|---|---|---|---|---|---|---|
| **Damage size/position** | 206701 | 165 | 1987 | 424 | 0 | 1.28 |
| **Thickness variation** | 6976 | 4 | 1744 | 372 | 0 | 2.39 |
| **Error** | 1946 | 660 | 4 | | | |
| **Total** | 215623 | 829 | | | | |

**Sensor 12**

| Source of variation | SS | df | MS | F | P-value | F crit |
|---|---|---|---|---|---|---|
| **Damage size/position** | 134266 | 165 | 1291 | 502 | 0 | 1.28 |
| **Thickness variation** | 5118 | 4 | 1279 | 497 | 0 | 2.39 |
| **Error** | 1069 | 660 | 2 | | | |
| **Total** | 140454 | 829 | | | | |

| | | | Sensor 13 | | | |
|---|---|---|---|---|---|---|
| **Source of variation** | SS | df | MS | F | P-value | F crit |
| **Damage size/position** | 130148 | 165 | 1251 | 842 | 0 | 1.28 |
| **Thickness variation** | 4121 | 4 | 1030 | 693 | 0 | 2.39 |
| **Error** | 617 | 660 | 1 | | | |
| **Total** | 134888 | 829 | | | | |
| | | | **Sensor 14** | | | |
| **Source of variation** | SS | df | MS | F | P-value | F crit |
| **Damage size/position** | 111839 | 165 | 1075 | 544 | 0 | 1.28 |
| **Thickness variation** | 4255 | 4 | 1063 | 538 | 0 | 2.39 |
| **Error** | 821 | 660 | 1 | | | |
| **Total** | 116916 | 829 | | | | |
| | | | **Sensor 15** | | | |
| **Source of variation** | SS | df | MS | F | P-value | F crit |
| **Damage size/position** | 318842 | 165 | 3065 | 1453 | 0 | 1.28 |
| **Thickness variation** | 4725 | 4 | 1181 | 560 | 0 | 2.39 |
| **Error** | 877 | 660 | 2 | | | |
| **Total** | 324445 | 829 | | | | |
| | | | **Sensor 16** | | | |
| **Source of variation** | SS | df | MS | F | P-value | F crit |
| **Damage size/position** | 304479 | 165 | 2927 | 406 | 0 | 1.28 |
| **Thickness variation** | 41060 | 4 | 10265 | 1426 | 0 | 2.39 |
| **Error** | 2993 | 660 | 7 | | | |
| **Total** | 348533 | 829 | | | | |
| | | | **Sensor 17** | | | |
| **Source of variation** | SS | df | MS | F | P-value | F crit |
| **Damage size/position** | 1238033 | 165 | 11904 | 2471 | 0 | 1.28 |
| **Thickness variation** | 94707 | 4 | 23676 | 4915 | 0 | 2.39 |
| **Error** | 2003 | 660 | 4 | | | |
| **Total** | 1334744 | 829 | | | | |

## 5.5. Summary of case study 2

The main purpose of this chapter was to statistically investigate the importance of potential manufacturing uncertainty, e.g., material ply thickness variations, on the reliability of a given damage signature database (DSD). A hand laid-up and vacuumed bagged composite airfoil was chosen as the basis of case study. The established FE model under quasi-static tensile loading was used as a virtual experimental tool to perform more detailed statistical analysis on the effect of thickness variation as a representative manufacturing error. During statistical analysis, first the case was limited only to 4 damage scenarios, which led to the identification of 4 out of 15 sensor points capable of showing abnormalities due to damage regardless of the presence of ply thickness uncertainty. Next, when a more comprehensive DSD (with 168 scenarios) was implemented, all the sensors exhibited almost the same damage detection sensitivity as the uncertainty effect, even though the range of noise had been reduced to half. This, in turn, suggests the importance of (1) relying on larger DSDs for more realistic representation of the complex behavior of structures under uncertainty, and (2) the need for a SHM that can be trained via a reasonably sized DSD and be less sensitive to uncertainty and more to the damage. This is the main goal of Chapters 6 and 7 as follows.

# Chapter 6

# Conventional and Signal-to-Noise (SN) Ratio Modified Artificial Neural Networks (ANN) Structural Health Monitoring Systems

## Chapter preview

In this chapter, a conventional multi-layer perceptron neural network is first trained using the airfoil data in Chapter 5 with only the original ply thickness cases and varying damage size and location. Then the ability of the trained network is investigated against predicting the damage in all the composite airfoils including those with varying ply thicknesses (i.e., under uncertainty). Results will show that the conventional network which is commonly used in the literature cannot accurately predict the damage in the current case study, especially the damage size as was hypothesized in Chapter 5. One suggestion to deal with this problem is to extend the Damage Signature Database (DSD) in the training stage to cover the majority of uncertainty scenarios. This solution works theoretically well but is not practical, as it will involve a considerable amount of time and cost for a manufacturer/designer to develop such a giant DSD. Another suggestion that is explored in this thesis is the implementation of a Signal-to-Noise (SN) ratio to weigh the input layer of the network. It will be shown that this strategy notably outperforms the conventional neural network, but again, estimating the precise SN weights in practice requires an immense expert knowledge of the structure or testing of a large number of scenarios with uncertainty and identifying random strain distributions at different sensor locations. This will then take the work to Chapter 7 to address these shortcomings.

## 6.1. Introduction to conventional pattern recognition techniques in SHM

As briefly reviewed in Chapter 3, Artificial Neural Networks (ANNs) are powerful techniques widely used for pattern recognition in structural health monitoring applications. ANNs are provided with the measured sensory information such as displacement, acceleration, stress/strain state, damping ratio, mode shapes, etc. in time or frequency domains and are expected to correlate these data to the state of damage (location and size of defect) in the structure. In order to get the most accurate and reliable outcome from ANNs, their architectures should be carefully chosen and verified using the provided training/testing sets. The architecture optimization of the ANN consists of deciding on the number of hidden layers, number of neurons in each hidden layer, activation function, learning algorithm and learning rule. Unfortunately, there is no exact solution for finding the perfect combination of these parameters for the given input sets and they should be found by iterative algorithms. Usually, the technique of k-fold cross validation is used to come up with the most appropriate ANN architectures. As discussed in chapter 3, in this technique the overall input space is randomly divided up to the k-number of sub-spaces; each one called a fold. At each iteration, one of these folds is chosen as the testing and the other folds are considered to be part of the training for the corresponding ANN. This process keeps repeating until each fold has been considered for testing once. The network which shows minimum deviation between the predicted values and the actual testing targets is chosen as the best ANN [70].

This chapter represents the process of finding the optimum ANN subjected to training via damage scenarios of nominal airfoils (in which all ply thicknesses have been assumed to be 0.22mm) (also called 'nominal DSD' hereafter). Then its accuracy in predicting the 'total DSD' (i.e., containing all samples with and without varying ply thicknesses) has been evaluated. Next, another ANN has been trained this time with both nominal and noisy DSDs (i.e., the total DSD) to compare with the earlier ANN and highlight the effect of noise. At last, a new application of signal-to-noise ratio (SN) has been implemented to arrive at a notably enhanced ANN. At the end of this chapter all the approaches are compared and the necessity for adapting a Gaussian Process- based pattern recognition technique is outlined.

## 6.2. Conventional Artificial Neural Networks

There is total number of 166 damage scenarios obtained in Section 5.3. They share the same airfoil geometry, material properties, thickness values and the same loading. However, they are subjected to different sizes and locations of damages. Four out of the 166 scenarios were those replicates in the lab experiments (Section 5.1), and therefore have been removed from the (net) training/testing loop of the ANN. For each individual damage scenario (DSD) of the remaining 162 cases, five FE models were run with the same material properties and only randomly changing the ply thicknesses according to intervals provided by Table 6.9, resulting in a total of 162 nominal and 810 noisy damage scenarios.

The 1$^{st}$ step in the design of above SHM tool required determining the best architecture for the ANN. This was done initially using the nominal DSD only. In Tables 6.1 through 6.6 the results of cross validation for the nominal cases are presented for three different neural architectures presented in Figure 6.1 through 6.3. Figures 6.4 and 6.5 illustrate the obtained regression plot and error histogram, respectively, for the optimum ANN which in our case was shown to consist of 4 hidden layers.

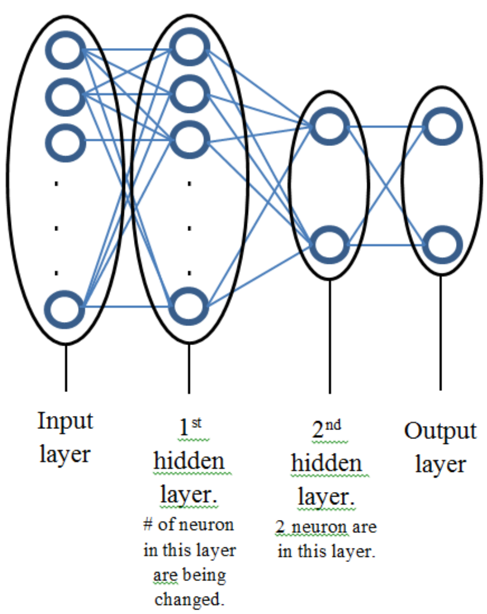


**Figure 6.1.** NN architecture for 2 hidden layers MLP (Multi-Layer Perceptron) networks

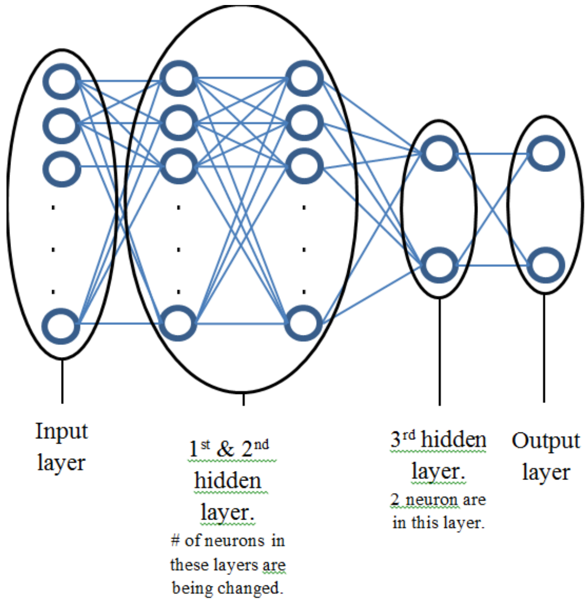


**Figure 6.2.** NN architecture for 3 hidden layers MLP networks

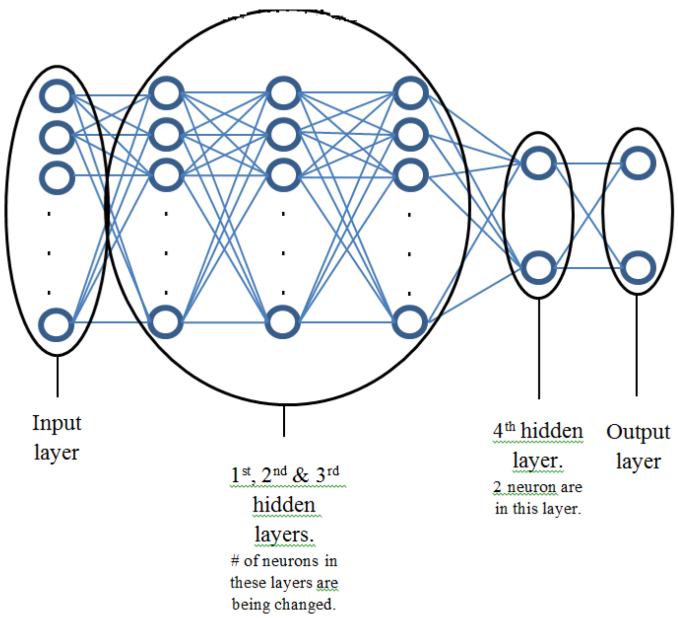


**Figure 6.3.** NN architecture for 4 hidden layers MLP networks

**Table 6.1.** ANNs with 2 hidden layers predicting the size of damage (finding the best number of neurons in the $1^{st}$ layer, Figure 6.1)

| DSDs | Real damage length (cm) | Number of hidden nodes in the $1^{st}$ hidden layer for the 2 hidden layer MLP | | | | | | | DSDs | Number of hidden nodes in the $1^{st}$ hidden layer for the 2 hidden layer MLP | | | | | | |
|---|---|---|---|---|---|---|---|---|---|---|---|---|---|---|---|---|
| | | 10 | 20 | 30 | 40 | 50 | 60 | 70 | | 10 | 20 | 30 | 40 | 50 | 60 | 70 |
| | | **Predicted damage length** (mm) by the NN | | | | | | | | **Percentage error%** in damage length prediction | | | | | | |
| DSD1 | 1.99 | 3.10 | 2.69 | 2.03 | 2.58 | 3.04 | 3.12 | 2.19 | DSD1 | 27.61 | 17.46 | 1.03 | 14.61 | 26.22 | 28.22 | 5.09 |
| DSD2 | 2.13 | 3.12 | 2.31 | 3.01 | 2.74 | 2.85 | 2.35 | 2.56 | DSD2 | 24.71 | 4.30 | 21.89 | 15.19 | 17.73 | 5.25 | 10.66 |
| DSD3 | 1.93 | 2.52 | 2.21 | 2.13 | 1.58 | 2.20 | 1.69 | 1.68 | DSD3 | 14.56 | 6.85 | 4.90 | 8.81 | 6.65 | 6.12 | 6.37 |
| ⋮ | ⋮ | ⋮ | ⋮ | ⋮ | ⋮ | ⋮ | ⋮ | ⋮ | ⋮ | ⋮ | ⋮ | ⋮ | ⋮ | ⋮ | ⋮ | ⋮ |
| DSD161 | 2.67 | 2.33 | 3.06 | 2.90 | 3.44 | 3.16 | 3.03 | 2.67 | DSD161 | 8.61 | 9.77 | 5.76 | 19.13 | 12.30 | 8.96 | 0.18 |
| DSD162 | 3.33 | 2.18 | 3.28 | 3.11 | 3.69 | 3.36 | 3.22 | 2.95 | DSD162 | 28.88 | 1.51 | 5.57 | 8.97 | 0.63 | 3.00 | 9.65 |

| Number of hidden neurons | | | | | | |
|---|---|---|---|---|---|---|
| 10 | 20 | 30 | 40 | 50 | 60 | 70 |
| **Average** of size prediction error% | | | | | | |
| 27.13 | 22.33 | 19.79 | 19.23 | 21.36 | 18.82 | 17.13 |

**Table 6.2.** ANNs with 2 hidden layers predicting the location of damage (finding the best number of neurons in the 1st layer, Figure 6.1)

| DSDs | Real damage location (cm) | Number of hidden nodes in the 1st hidden layer for the 2 hidden layer MLP | | | | | | |
|---|---|---|---|---|---|---|---|---|
| | | 10 | 20 | 30 | 40 | 50 | 60 | 70 |
| | | **Predicted damage location** (cm) by the NN | | | | | | |
| DSD 1 | 2.50 | 10.49 | 18.77 | 6.10 | 3.16 | 12.07 | 14.58 | 3.10 |
| DSD 2 | 5.71 | 5.05 | 9.60 | 6.42 | 7.72 | 9.94 | 5.83 | 6.49 |
| DSD 3 | 9.00 | 24.38 | 21.17 | 14.49 | 15.23 | 23.34 | 8.21 | 8.97 |
| ⋮ | ⋮ | ⋮ | ⋮ | ⋮ | ⋮ | ⋮ | ⋮ | ⋮ |
| DSD 161 | 28.68 | 28.62 | 28.16 | 27.71 | 25.96 | 28.09 | 27.16 | 27.70 |
| DSD 162 | 28.67 | 30.99 | 30.11 | 29.34 | 27.53 | 30.28 | 28.57 | 28.60 |

| DSDs | Number of hidden nodes in the 1st hidden layer for the 2 hidden layer MLP | | | | | | |
|---|---|---|---|---|---|---|---|
| | 10 | 20 | 30 | 40 | 50 | 60 | 70 |
| | **Percentage error%** in damage location prediction | | | | | | |
| DSD 1 | 23.85 | 48.56 | 10.72 | 1.95 | 28.56 | 36.03 | 1.77 |
| DSD 2 | 1.96 | 11.62 | 2.13 | 6.02 | 12.65 | 0.37 | 2.33 |
| DSD 3 | 45.90 | 36.30 | 16.39 | 18.60 | 42.79 | 2.36 | 0.11 |
| ⋮ | ⋮ | ⋮ | ⋮ | ⋮ | ⋮ | ⋮ | ⋮ |
| DSD 161 | 0.16 | 1.54 | 2.87 | 8.10 | 1.75 | 4.52 | 2.93 |
| DSD 162 | 6.91 | 4.30 | 1.99 | 3.42 | 4.80 | 0.29 | 0.21 |

| Number of hidden neurons | | | | | | |
|---|---|---|---|---|---|---|
| 10 | 20 | 30 | 40 | 50 | 60 | 70 |
| **Average** of location prediction error% | | | | | | |
| 18.99 | 17.13 | 15.99 | 14.88 | 19.11 | 14.91 | 14.38 |

**Table 6.3.** ANNs with 3 hidden layers predicting the size of damage (finding the best number of neurons in the $1^{st}$ & $2^{nd}$ layers, Figure 6.2)

| | | Average damage size prediction percentage error | | | | | | | | |
|---|---|---|---|---|---|---|---|---|---|---|
| | | Number of neurons in the $2^{nd}$ hidden layer | | | | | | | | |
| | | 1 | 2 | 3 | | 11 | | 48 | 49 | 50 |
| Number of neurons in the $1^{st}$ hidden layer | 1 | 15.53 | 15.63 | 20.25 | · · · | 14.16 | · · · | 38.97 | 29.63 | 15.54 |
| | 2 | 15.53 | 15.42 | 15.95 | · · · | 38.57 | · · · | 16.47 | 12.69 | 15.55 |
| | 3 | 15.42 | 15.57 | 15.61 | · · · | 14.62 | · · · | 17.81 | 17.16 | 15.44 |
| | | ⋮ | ⋮ | ⋮ | ⋮ | ⋮ | ⋮ | ⋮ | ⋮ | ⋮ |
| | 46 | 15.79 | 15.39 | 17.11 | · · · | **5.25** | · · · | 14.96 | 14.88 | 16.81 |
| | | ⋮ | ⋮ | ⋮ | ⋮ | ⋮ | ⋮ | ⋮ | ⋮ | ⋮ |
| | 48 | 15.74 | 15.95 | 15.94 | · · · | 18.81 | · · · | 9.99 | 8.39 | 9.86 |
| | 49 | 15.73 | 18.62 | 15.31 | · · · | 15.51 | · · · | 7.71 | 9.95 | 5.73 |
| | 50 | 15.53 | 15.50 | 15.61 | · · · | 15.62 | · · · | 9.50 | 5.77 | 5.95 |

**Table 6.4.** ANNs with 3 hidden layers predicting the location of damage (finding the best number of neurons in the $1^{st}$ & $2^{nd}$ layers, Figure 6.2)

| | | Average damage location prediction percentage error | | | | | | | | |
|---|---|---|---|---|---|---|---|---|---|---|
| | | Number of neurons in the $2^{nd}$ hidden layer | | | | | | | | |
| | | 1 | 2 | 3 | | 7 | | 48 | 49 | 50 |
| Number of neurons in the $1^{st}$ hidden layer | 1 | 16.97 | 15.92 | 28.74 | · · · | 7.54 | · · · | 14.29 | 18.30 | 13.36 |
| | 2 | 17.80 | 15.52 | 12.09 | · · · | 10.76 | · · · | 11.63 | 14.08 | 13.68 |
| | 3 | 15.07 | 17.56 | 11.76 | · · · | 8.87 | · · · | 15.38 | 10.50 | 14.64 |
| | | ⋮ | ⋮ | ⋮ | ⋮ | ⋮ | ⋮ | ⋮ | ⋮ | ⋮ |
| | 25 | 8.035 | 6.659 | 6.107 | · · · | **1.83** | · · · | 6.00 | 9.22 | 5.87 |
| | | ⋮ | ⋮ | ⋮ | ⋮ | ⋮ | ⋮ | ⋮ | ⋮ | ⋮ |
| | 48 | 4.62 | 3.76 | 4.63 | · · · | 11.62 | · · · | 5.28 | 3.59 | 3.59 |
| | 49 | 4.43 | 12.12 | 2.68 | · · · | 4.69 | · · · | 4.74 | 4.56 | 4.74 |
| | 50 | 11.45 | 3.36 | 5.96 | · · · | 11.43 | · · · | 3.13 | 9.95 | 4.96 |

**Table 6.5.** ANNs with 4 hidden layers predicting the size of damage (finding the best number of neurons in the 1st, 2nd & 3rd layers, Figure 6.3)

| Number of neurons in the 3rd hidden layer | Number of neurons in the 1st hidden layer | Number of neurons in the 2nd hidden layer: 1 | 2 | · · · | 19 | 20 |
|---|---|---|---|---|---|---|
| 1 | 1 | 17.30 | 16.52 | · · · | 15.51 | 15.48 |
| 1 | 2 | 16.86 | 14.88 | · · · | 15.50 | 15.51 |
| | ⋮ | | | | | |
| 1 | 29 | 15.52 | 15.56 | · · · | 15.51 | 15.65 |
| 1 | 30 | 15.51 | 15.52 | · · · | 38.61 | 15.77 |
| ⋮ | | | | | | |
| 20 | 1 | 16.27 | 20.60 | · · · | 15.71 | 34.60 |
| 20 | 2 | 15.56 | 38.53 | · · · | 15.25 | 16.19 |
| | ⋮ | | | | | |
| 20 | 29 | 14.75 | 16.19 | · · · | 14.84 | 13.12 |
| 20 | 30 | 15.52 | 15.18 | · · · | 13.32 | 12.93 |
| ↓ | | | | | | |
| The best network for damage size prediction | | | | | | |
| The architecture of the hidden layers: 16-18-11-2 | | Average error% in size prediction | | | | 4.04 |

**Table 6.6.** ANNs with 4 hidden layers predicting the location of damage (finding the best number of neurons in the $1^{st}$, $2^{nd}$ & $3^{rd}$ layers, Figure 6.3)

<table>
<tr><td colspan="4" rowspan="2"></td><td colspan="5">Number of neurons in the $2^{nd}$ hidden layer</td></tr>
<tr><td>1</td><td>2</td><td>· · ·</td><td>19</td><td>20</td></tr>
<tr><td rowspan="16">Number of neurons in the $3^{rd}$ hidden layer</td><td rowspan="5">1</td><td rowspan="5">Number of neurons in the $1^{st}$ hidden layer</td><td>1</td><td>18.67</td><td>14.69</td><td>· · ·</td><td>21.52</td><td>15.78</td></tr>
<tr><td>2</td><td>8.15</td><td>16.20</td><td>· · ·</td><td>21.12</td><td>11.10</td></tr>
<tr><td colspan="6">⋮</td></tr>
<tr><td>29</td><td>7.55</td><td>4.28</td><td>· · ·</td><td>4.49</td><td>11.84</td></tr>
<tr><td>30</td><td>5.33</td><td>4.86</td><td>· · ·</td><td>4.14</td><td>4.94</td></tr>
<tr><td colspan="8">⋮</td></tr>
<tr><td colspan="3" rowspan="2"></td><td colspan="5">Number of neurons in the $2^{nd}$ hidden layer</td></tr>
<tr><td>1</td><td>2</td><td>· · ·</td><td>19</td><td>20</td></tr>
<tr><td rowspan="5">20</td><td rowspan="5">Number of neurons in the $1^{st}$ hidden layer</td><td>1</td><td>19.62</td><td>17.22</td><td>· · ·</td><td>21.48</td><td>20.79</td></tr>
<tr><td>2</td><td>17.40</td><td>23.13</td><td>· · ·</td><td>12.40</td><td>8.64</td></tr>
<tr><td colspan="6">⋮</td></tr>
<tr><td>29</td><td>15.85</td><td>21.45</td><td>· · ·</td><td>4.45</td><td>4.77</td></tr>
<tr><td>30</td><td>21.47</td><td>18.22</td><td>· · ·</td><td>4.38</td><td>4.69</td></tr>
<tr><td colspan="9">↓</td></tr>
<tr><td colspan="9">The best network for damage location prediction</td></tr>
<tr><td colspan="4">The architecture of the hidden layers: 24-20-8-2</td><td colspan="4">Average error% in size prediction</td><td>1.05</td></tr>
</table>

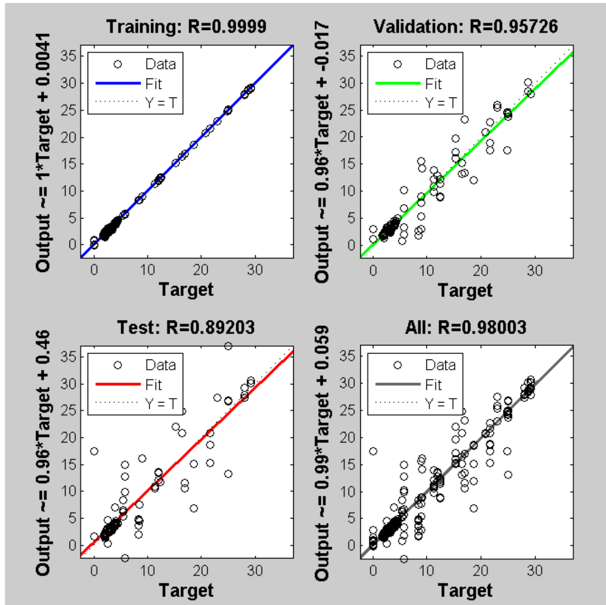


**Figure 6.4.** Regression plot of the optimized Neural Network (training, validation and testing sets, as well as the total set)

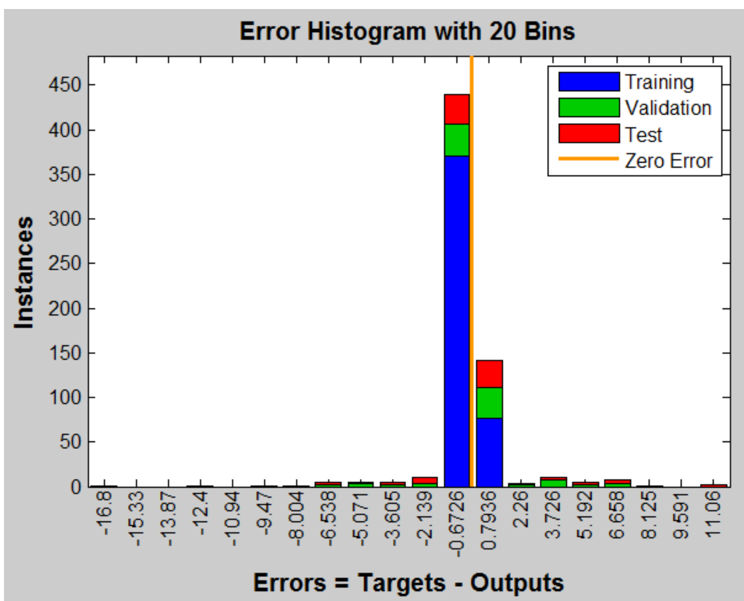


**Figure 6.5.** Error histogram of the optimized Neural Network

Table 6.7 summarizes all the result of cross validation for the mentioned MLP networks trained by nominal DSD. The optimum network was found to consist of 17 neurons in the input layer, 24 neurons for the 1st hidden layer, 20 neurons in the 2nd hidden layer, 8 neurons in the 3rd hidden layer, 2 neurons in the 4th hidden layer which are connected to the last 2 neurons in the output layer (damage location and size) by a linear activation function. In all the layers, except the last one, tan-sigmoid has been employed as the activation function.

**Table 6.7.** Summary of all optimized Neural Networks for nominal DSD without thickness variation

| | Min. damage location prediction error% | Min. damage size prediction error% |
|---|---|---|
| 2 hidden layers | 14.4% (70-2 neurons) | 17.1% (70-2 neurons) |
| 3 hidden layers | 1.8% (25-7-2 neurons) | 5.2% (46-11-2 neurons) |
| 4 hidden layers | 1.1% (24-20-8-2 neurons) | 4.0% (16-18-11-2 neurons) |

Next, then the best trained network (24-20-8-2 NN in Table 6.7) was used to predict damage in all airfoils with and without uncertainty (i.e., the total DSD). In addition, as a second trial and merely for comparison purposes, the same network was trained with both nominal and noisy damage scenarios and then used to predict the total DSD again. The results of the mentioned analyses are provided in Table 6.8. From low prediction% values, it is clear that the conventional ANN is not capable of predicting the thickness varying scenarios when it has only been trained by nominal DSD. If the same network is trained with the entire DSD, however, it is expectedly becoming capable of predicting damage under uncertainty. This shows the generalizability of the Neural Network on one hand, but also it is considered as an important weakness (at least in the current case study) because practically speaking, it means this NN will require testing all damage scenarios under several random repeats to arrive at a large DSD to include in the training pool of a robust SHM system.

**Table 6.8.** Summary of Neural Network analysis for nominal (original) and thickness varying damage scenarios

| | Training set | Predicting | Accuracy of size prediction | Accuracy of location prediction |
|---|---|---|---|---|
| 1 | Original | Original and thickness varying scenarios | 35.5% | 57.2% |
| 2 | Original and thickness varying scenarios | Original and thickness varying scenarios | 95.8% | 97.0% |

## 6.3. Signal-to-Noise (SN) ratio Analysis

As reviewed in chapter 3, the SN analysis is a powerful technique in static and dynamic parametric design studies. In this dissertation, different types of SN ratios have been adapted to weigh the sensory input layer of the optimum MLP network obtained in Section 6.1. The SN ratios have been calculated based on the varying thickness and the nominal damage scenarios (i.e., about 1,000 scenarios). During the training stage, these ratios act like weighting coefficients for the neural network resulting in a dominant effect of sensors with larger SN coefficients. The effectiveness of different SN ratio types was evaluated in the current SHM case study as follows (for further details refer to chapter 3):

- Larger-the-best static SN ratio: $-10\log_{10}\left(\frac{1}{m}\sum\frac{1}{y_{ij}^2}\right)$ also called SN-S
- Smaller-the-best static SN ratio: $-10\log_{10}\left(\frac{1}{m}\sum y_{ij}^2\right)$ also called SN-T
- Nominal-the-best static SN ratio: $10\ \log_{10}\left(\frac{\bar{y_i}^2}{s_i^2}\right)$ where $\ln s_i^2 = \ln\frac{\sum\left(y_{ij}-\bar{y_i}\right)^2}{m-1}$ called SN-L
- Zero-proportional Dynamic SN (SN-D): $10\ \log_{10}\frac{slope^2}{MSE}$; $MSE = Mean\ Square\ Error$

$y_{ij} = \text{the sensor reading in the} i^{\text{th}} \text{ damage scenario and the } j^{\text{th}} \text{ thickness variation}$

Results of SN ratio calculations are summarized in Table 6.9.

**Table 6.9.** Summary of Signal-to-Noise (SN) ratios

| | Sensor 1 | Sensor 2 | Sensor 3 | Sensor 4 | Sensor 5 | Sensor 6 | Sensor 7 | Sensor 8 | Sensor 9 | Sensor 10 | Sensor 11 | Sensor 12 | Sensor 13 | Sensor 14 | Sensor 15 | Sensor 16 | Sensor 17 |
|---|---|---|---|---|---|---|---|---|---|---|---|---|---|---|---|---|---|
| **SN-S** | -34.8 | -34.0 | -31.6 | -32.8 | -32.9 | -33.1 | -32.7 | -33.1 | -32.8 | -32.8 | -32.7 | -32.5 | -32.3 | -32.2 | -31.6 | -26.9 | -34.5 |
| **SN-T** | 30.9 | 21.8 | 17.9 | 14.4 | 13.5 | 17.8 | 10.4 | 23.3 | 14.4 | 21.3 | 25.0 | 24.4 | 25.4 | 27.5 | 15.6 | -3.3 | 28.9 |
| **SN-L** | 34.8 | 34.0 | 31.2 | 32.6 | 32.2 | 32.9 | 29.1 | 33.0 | 32.7 | 32.8 | 32.7 | 32.5 | 32.3 | 32.2 | 30.8 | 0.8 | 34.0 |
| **SN-D** | -30.4 | -32.2 | -43.6 | -37.1 | -34.3 | -32.6 | -32.5 | -31.9 | -31.5 | -31.1 | -31.3 | -31.2 | -31.2 | -31.3 | -32.6 | -41.3 | -30.8 |

Table 6.10 illustrates the prediction results when the conventional neural network has been weighted by the SN ratios in Table 6.9 in order to predict the nominal DSD (the left column) and the noisy DSD (the right column). Note that the noisy DSD scenarios have not been directly used in the training process, but their impacts have been condensed in the SN ratios by weighting the input layer of the trained NN. From Table 6.10, the SN-S ratio type has led to the worst prediction results by providing an average of 23.1% accuracy for size prediction, in the case of being trained by nominal DSD and predicting the noisy DSD. This means the SN-S weights not only have not helped the SHM tool, but also delinked its robustness. The SN-L and SN-D types, however, show a highly improved performance both when used on the original optimum NN and when the NN architecture is re-optimized with the new weighting information. By implementing the dynamic signal to noise ratio analysis (SN-D), the accuracy of damage location prediction was found to be the highest among all NN models (as high as ~92%) when the network is trained by the original (nominal) damage database and used to predict the thickness varying (noisy) scenarios.

**Table 6.10.** Comparing the percentage accuracy of different SN ratio approaches

| SN-S | | | | |
|---|---|---|---|---|
| Nominal DSD training case | | | Training using nominal and predicting nominal + noisy | |
| Accuracy in predicting nominal DSD | | | Accuracy in predicting overall DSD | |
| Accuracy in Size prediction | 91.1 | | Accuracy in Size prediction | 23.1 |
| Accuracy in Location prediction | 97.0 | | Accuracy in Location prediction | 66.1 |
| **SN-T** | | | | |
| Nominal DSD training case | | | Training using nominal and predicting nominal + noisy | |
| Accuracy in predicting nominal DSD | | | Accuracy in predicting overall DSD | |
| Accuracy in Size prediction | 90.9 | | Accuracy in Size prediction | 52.7 |
| Accuracy in Location prediction | 96.4 | | Accuracy in Location prediction | 60.0 |
| **SN-L** | | | | |
| SN-L using nominal optimum NN architecture | | | | |
| Nominal DSD training case | | | Training using nominal and predicting nominal + noisy | |
| Accuracy in predicting nominal DSD | | | Accuracy in predicting overall DSD | |
| Accuracy in Size prediction | 88.7 | | Accuracy in Size prediction | 79.0 |
| Accuracy in Location prediction | 94.6 | | Accuracy in Location prediction | 70.6 |
| SN-L using SN-L factored optimum NN architecture | | | | |
| Nominal DSD training case | | | Training using nominal and predicting nominal + noisy | |
| Accuracy in predicting nominal DSD | | | Accuracy in predicting overall DSD | |
| Accuracy in Size prediction | 96.1 | | Accuracy in Size prediction | 86.8 |
| Accuracy in Location prediction | 98.1 | | Accuracy in Location prediction | 79.0 |
| **SN-D** | | | | |
| SN-D using nominal optimum NN architecture | | | | |
| Nominal DSD training case | | | Training using nominal and predicting nominal + noisy | |
| Accuracy in predicting nominal DSD | | | Accuracy in predicting overall DSD | |
| Accuracy in Size prediction | 92.0 | | Accuracy in Size prediction | 87.3 |
| Accuracy in Location prediction | 96.1 | | Accuracy in Location prediction | 93.8 |
| SN-D using SN-D factored optimum NN architecture | | | | |
| Nominal DSD training case | | | Training using nominal and predicting nominal + noisy | |
| Accuracy in predicting nominal DSD | | | Accuracy in predicting overall DSD | |
| Accuracy in Size prediction | 95.4 | | Accuracy in Size prediction | 92.2 |
| Accuracy in Location prediction | 98.2 | | Accuracy in Location prediction | 91.2 |

## 6.4. Summary of conventional and enhanced NN implementation

MLP Artificial neural network is a powerful technique for pattern recognition in structural health monitoring applications, but its efficiency reduces when dealing with unseen uncertainty in the input parameters. One way to deal with this issue is to include the uncertainty scenarios in the training set, but this approach involves developing a vast damage database which requires considerable time and budget. Another approach is weighting the conventional neural network by signal-to-noise coefficients. These weighting parameters can be estimated from past experience/expert knowledge or by analyzing/running several noisy damage scenarios. In this chapter, the noisy DSD was analyzed for each input neuron to calculate the corresponding SN ratio for that node in the input layer. This approach dramatically increased the efficiency of the NN-bases SHM, even though it was trained with the original damage scenarios (nominal DSD) and the weights were only used in the final prediction stage after training. Table 6.11 is a complete summary of all different training and prediction scenarios using the NN and weighted NN in this chapter.

**Table 6.11.** Summary results of conventional and weighted neural networks

| NN type | Training set | Predicting | % Accuracy of **size** prediction | % Accuracy of **location** prediction |
|---|---|---|---|---|
| Conventional NN | Original | Original + thickness varying | 35.5% | 57.2% |
| Conventional NN | Original + thickness varying | Original + thickness varying | 95.8% | 97.0% |
| SN-L NN with re-optimized architecture | Original | Original + thickness varying | 86.8% | 79.0% |
| SN-T NN with re-optimized architecture | Original | Original + thickness varying | 52.7% | 60.0% |
| SN-S NN with re-optimized architecture | Original | Original + thickness varying | 23.1% | 66.1% |
| SN-D NN with re-optimized architecture | Original | Original + thickness varying | 92.2% | 91.2% |

# Chapter 7

# Gaussian Processes (GP) for Structural Health Monitoring

## Chapter preview

In this chapter, two Gaussian Processes (the standard and regression types) have been implemented to predict the state of damage in the composite airfoil structure studied in the preceding chapter via the ANN approach. Different covariant functions have been evaluated to simulate the GP process, along with an optimum function which in this case was the rational-quadratic covariant function. Results will show a remarkable capability of the new GP-based approach to deal with uncertainty in pattern recognition problems for SHM of multi-layer structures such as the composite airfoil under study.

## 7.1. Gaussian Processes

As shown in detail in Chapter 6, Multi-Layer Perceptron (MLP) Neural Networks, despite their generalizability, are not always able to deal with the uncertainty of input parameters in the conventional form, and an implementation of signal-to-noise analysis by weighting the input layer of the network is needed to result in an accurate SHM. However the latter approach was presumed to be very costly in practice (excessive time and budget will be needed to develop the required damage scenarios) and sensitive to estimation of weights. Unlike neural networks, or regression processes, in Gaussian Processes (GPs) no model/architecture is pre-imposed on the outcome of the process. Gaussian Processes are based on covariance functions which describe the type of dependency/impact that every pair of input nodes have on each other. This relation is usually formulated in the form of exponential functions with the absolute or square Euclidean distance between the input points. Depending on the type of data, different covariant functions can be selected (see also Table 3.1). Table 7.1 illustrates the result of different covariant functions used in the airfoil case study for predicting the location and extent of damage while training a GP by only original damage scenarios (nominal DSD), and then predicting the noisy (thickness varying) damage scenarios. Theoretical considerations of the GP methods were presented in Chapter 3.

**Table 7.1.** Comparing different covariance functions for the case of predicting noisy (thickness varying) case studies using nominal (original) damage scenarios (for the definition of covariant functions refer to Table 3.1)

| % Error | | | | |
|---|---|---|---|---|
| **Y1= size & Y2= location** | Percentage error % | | Average standard deviation of prediction?? Or do you mean COV/coefficient of variation which is (STD/predicted value) | |
| <u>Covariant functions tested:</u> | Y1 | Y2 | std-Y1 | std-Y2 |
| noise function | --- | --- | --- | --- |
| constant function | --- | --- | --- | --- |
| linear | 71.06 | 47.97 | 28.68 | 1510.23 |
| linear ARD | 318.42 | 22.17 | 1.15 | 1.37 |
| linear with bias | 39.93 | 128.3 | 0.21 | 0.46 |
| third order polynomial | 19.11 | 33.94 | 0.27 | 2.01 |
| Gaussian with ARD | 26.32 | 15.54 | 0.47 | 3.05 |
| Isotropic Gauss no scale | 63.03 | --- | --- | --- |
| **rational quadratic** | **11.88** | **13.84** | **0.32** | **0.38** |
| isotropic | 12.46 | 16.07 | 0.24 | 0.51 |
| Matern class q=3 | 15.74 | 28.62 | 0.29 | 4.22 |
| periodic | diverged | | diverged | |
| compact support poly degree 2 | 17.62 | 25.86 | 0.28 | 2.73 |
| squared exponential | 19.3 | 29.27 | 0.28 | 7.09 |
| NN covariance function | 13.96 | 19.11 | 0.28 | 0.87 |

| % Accuracy | | | | |
|---|---|---|---|---|
| **Y1= size & Y2= location** | Percentage accuracy % | | Average standard deviation of prediction?? | |
| <u>Covariant functions tested:</u> | Y1 | Y2 | std-Y1 | std-Y2 |
| noise function | --- | --- | --- | --- |
| constant function | --- | --- | --- | --- |
| linear | 28.94 | 52.03 | 28.68 | 1510.23 |
| linear ARD | 18.42 | 77.83 | 1.15 | 1.37 |
| linear with bias | 60.07 | 28.3 | 0.21 | 0.46 |
| third order polynomial | 80.89 | 66.06 | 0.27 | 2.01 |
| Gaussian with ARD | 73.68 | 84.46 | 0.47 | 3.05 |
| Isotropic Gauss no scale | 36.97 | --- | --- | --- |
| **rational quadratic** | **88.12** | **86.16** | **0.26** | **0.39** |
| isotropic | 87.54 | 83.93 | 0.24 | 0.51 |
| Matern class q=3 | 84.26 | 71.38 | 0.29 | 4.22 |
| periodic | diverged | | diverged | |
| compact support poly degree 2 | 82.38 | 74.14 | 0.28 | 2.73 |
| squared exponential | 80.7 | 70.73 | 0.28 | 7.09 |
| NN covariance function | 86.04 | 80.89 | 0.28 | 0.87 |

The Gaussian Process did not yield meaningful results using a noise function, the constant function, and the isotropic Gaussian covariant function. The periodic covariant function led to the divergence of the GP algorithm. The linear, linear ARD, linear with bias and Gaussian with ARD resulted in poor predictions. The 3rd order polynomial function was only capable of predicting the location of delaminations with 80.89% accuracy, and its precision for delamination size prediction was 66.06%. The only successful covariant functions, according to Table 7.1, has been the Rational Quadratic (RQ), isotropic, Matern, compact support polynomial, Squared Exponential (SE) and Neural Network (NN) covariant functions with the accuracies ranging from 80.7% to 88.12% in damage location and 70.73% to 86.16% in damage size predictions. The Squared Exponential (SE) and the Neural Network (NN) are among most common types of covariant function used in the Gaussian Process literature [76]. Nevertheless, for the current case study, the Rational Quadratic (RQ) was observed to be the most accurate covariant function according to Table 7.1. Therefore, the SE, NN and RQ covariant functions were selected and investigated further in the subsequent sections.

Table 7.2 shows the result of running GP for the aforementioned covariant functions with and without applying the Dynamic Signal-to-Noise ratios (the most precise weighting coefficients obtained for the NN in Chapter 6) to the training set (nominal DSD). For each weighting/covariant combination, three simulations were considered:

1. Only dealing with nominal DSD for both training and predicting stages
2. Training based on the nominal DSD and testing the predictability of all cases including the noisy (thickness varying) DSD. This combination of testing/predicting is of most interest to designers from a practical point of view; because the training part of the algorithm is only fed with a small number of damage scenarios under nominal conditions, and then the prediction takes over all damage cases including those under ‘unseen’ uncertainty.
3. Training and predicting based on the combination of nominal and noisy DSDs (i.e., using the total DSD). In this case, 70% of the total DSD is randomly chosen as part of the training and the remaining 30% is used for testing purposes.

**Table 7.2.** GP with/out dynamic SN ratios

| Weighting/covariant combination used | Training set | Predicting set | Damage size prediction accuracy % | Damage location prediction accuracy % |
|---|---|---|---|---|
| Unweighted/single Squared Exponentials | Nominal | Nominal | 91.12 | 98.14 |
| | Nominal | Nominal+Noisy | 80.70 | 70.73 |
| | Nominal+Noisy | Nominal+Noisy | 96.26 | 100.00 |
| Unweighted /single NN covariant functions | Nominal | Nominal | 99.97 | 100.00 |
| | Nominal | Nominal+Noisy | 86.04 | 80.89 |
| | Nominal+Noisy | Nominal+Noisy | 99.96 | 100.00 |
| Unweighted /single RQ | Nominal | Nominal | 99.95 | 100.00 |
| | Nominal | Nominal/Noisy | 88.12 | 86.16 |
| | Nominal+Noisy | Nominal+Noisy | 99.96 | 100.00 |
| Dynamic SN/single Squared Exponentials | Nominal | Nominal | 99.97 | 100.00 |
| | Nominal | Nominal+Noisy | 84.52 | 77.42 |
| | Nominal+Noisy | Nominal+Noisy | 96.28 | 100.00 |
| Dynamic SN/single NN covariant functions | Nominal | Nominal | 99.97 | 100.00 |
| | Nominal | Nominal+Noisy | 78.22 | 79.57 |
| | Nominal+Noisy | Nominal+Noisy | 99.97 | 100.00 |
| Dynamic SN/single RQ | Nominal | Nominal | Did Not converge. | |
| | Nominal | Nominal+Noisy | | |
| | Nominal+Noisy | Nominal+Noisy | | |

Very surprisingly, unlike the conventional neural network in Chapter 6 where the addition of signal-to-noise ratios resulted in sudden changes in damage prediction accuracy, for GPs in Table 7.2 the original non-weighted algorithms seem to be more accurate. The only GP that responded favourably to the addition of weighting coefficients is the single Square Exponential (SE). Multiplying the input data with the SN ratio in the case of SE covariant function increased the accuracy from 80.70% and 70.73% to 84.52% and 77.42% for the size and location predictions, respectively. This improvement was not observed for the NN covariant function, where the accuracy dropped from 86.04% and 80.89% to 78.22% and 79.57%, respectively. The situation became even worse for the RQ covariant function, where the procedure did not converge at all with the weighted dataset. In conclusion, it was found in this section that *adding* *weighting coefficients generally does not lead to better predictions for GP-based SHM. It can actually lead to poor predictions or even the divergence of the process.*

## 7.2. A Regression-Gaussian Process

The combination of regression and the Gaussian Process is known as 'regression-kriging' (RK) [39]. RK is a pattern recognition technique used for spatial predictions by combining the capabilities of the Ordinary-Least-Square (OLS) regression with a Gaussian Process. Figure 7.1 illustrates the idea behind the RK. The OLS regression is essentially used to provide an approximate solution to the pattern of interest, and then the GP algorithm tries to fit into the remaining prediction space by considering the deviation between the provided dataset and the predicted OLS values (i.e., like a sequential fitting procedure). The RK approach is very popular in the geostatistics, meteorology and soil mapping applications. In this section, the application of RK is evaluated for the original and noisy DSD scenarios of the airfoil case study. Table 7.3 summarizes the result of the OLS regression and the Gaussian Process (OSL-GP or RK) for the mentioned datasets. In the standard GP, the mean function was assumed to be zero and the covariant function predicts the actual target values; however in general the mean function can be chosen to be non-zero. In the RK, the linear regression curve (OLS) is presumed to act like the mean function, a starting point for the GP algorithm with RQ covariant function.

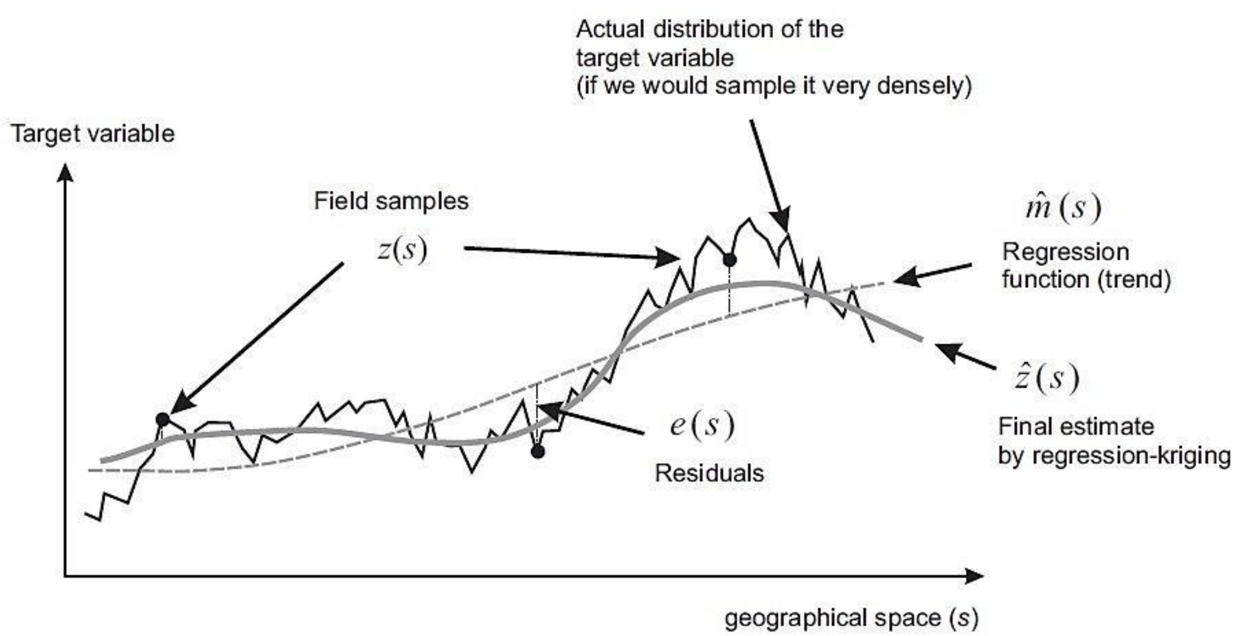


**Figure 7.1.** Regression-Kriging (RK) (source: wikipedia.com)

**Table 7.3.** Summary of the OLS regression, RK and modified GP subject to the nominal and the noisy damage scenarios for the training stage

| Method | Training set for OLS Regression | Training set for GP | Prediction set | Size of damage-prediction accuracy % | Location of damage - prediction accuracy % |
|---|---|---|---|---|---|
| OLS Regression | Nominal | --- | Nominal | 80.07 | 86.53 |
| | Nominal+Noisy | --- | Nominal+Noisy | 77.62 | 84.10 |
| | Nominal | --- | Nominal+Noisy | 6.83 | 10.08 |
| OLS Regression + GP | Nominal | Nominal | Nominal | 99.98 | 100.00 |
| | Nominal | Nominal | Nominal+Noisy | 8.08 | 8.2 |
| | Nominal+Noisy | Nominal+Noisy | Nominal+Noisy | 97.21 | 100.00 |
| | Nominal+Noisy | Nominal | Nominal+Noisy | 87.46 | 87.64 |

As seen from results in Table 7.3, the initial OLS increases the accuracy of the approach when the training and prediction datasets are identical. For the nominal dataset case, the accuracy improves from 80.07% and 86.53% (OLS only) to 99.98% and 100.00% for the size and location responses, respectively. OLS alone is only capable of predicting 77.62% and 84.10% of nominal+noisy cases when trained with both of them, but when the GP is added to the same procedure the precision becomes as high as 97.21% and 100.00%, respectively. Finally, it is noteworthy that the OLS regression on its own has shown a good performance when it is trained and tested on the same type of dataset (nominal with or without noisy) that is not the objective of this study (in another words, the desired/ideal algorithm should be able to predict noisy cases when it has only been trained by the original cases). **However, the predictability of OLS has been fully lost when the training only consists of the nominal DSD and the prediction evaluation is done over the whole database (which is the most practical case in real-life applications).** In the latter case, the addition of GP has also not helped the prediction. In other words, the addition of a poor OLS fitted model can notably limit the great capability of GP as found in the previous section (compare Tables 7.2 & 7.3). More specifically, in the current sequential RK procedure, the solution of the OLS regression becomes the mean function for GP and if it is poor, it affects the true nature of autocorrelation among data points in the prediction space. A remedy to this problem would be the use of higher order OLS models and/or implementation of the RK method in an iterative manner until a desirable accuracy is found [76].

## 7.3. Summary of GP in SHM

In this chapter different covariant functions were investigated in the context of a GP procedure for predicting the size and location of damage in the airfoil case study presented in Chapter 5. Besides the conventional single covariant GP procedure, the idea of weighting the input data by the dynamic SN ratios and starting the GP from the OLS regression baseline were investigated, seeking for an improvement in predicting the total DSD from the nominal DSD. For the GP with a Rational Quadratic (RQ) covariant function, the damage prediction accuracy reached almost to 90%. The weighting of input layer by SN coefficients did not result in a desired outcome. It actually caused a divergence of the RQ-GP SHM model and only a minor improvement was seen for the common Squared Exponential (SE)-GP model. The idea of combining the OLS regression and GP worked well only when the training and prediction sets were the same. When the OLS was trained by nominal cases and the prediction was done over the total DSD including noise, however, the GP did not lead to an agreeable improvement. As a conclusion, it is believed that the GP by itself is a very powerful method for SHM but it should be trained and implemented for every new case study by checking different possible covariant functions, seeking for the most optimum one. In the current case study, Table 7.4 summarizes all the GP variations for predicting the total DSD from the training via the nominal DSD. The RQ-GP SHM model appears to be the optimum in this study.

**Table 7.4.** Summary of all standard GPs, a SN weighted GP and OSL-GP for training with original damage scenarios and predicting the damage size and location for nominal plus thickness-varying scenarios

| Covariant function | SN-D ratios used? | Overall ranking | Ranking in dame size prediction | Ranking in damage location prediction | Size prediction accuracy% | Location prediction accuracy% |
|---|---|---|---|---|---|---|
| Rational quadratic (RQ) | No | 1 | 1 | 1 | 88.12 | 86.16 |
| Isotropic | No | 2 | 2 | 3 | 87.54 | 83.93 |
| NN covariance function | No | 3 | 3 | 4 | 86.04 | 80.89 |
| SND SE | Yes | 4 | 4 | 5 | 84.52 | 77.42 |
| Gaussian with ARD | No | 5 | 9 | 2 | 73.68 | 84.46 |
| Compact support poly degree 2 | No | 6 | 6 | 6 | 82.38 | 74.14 |
| Matern class q=3 | No | 7 | 5 | 7 | 84.26 | 71.38 |
| Squared exponential | No | 8 | 8 | 8 | 80.7 | 70.73 |
| Third order polynomial | No | 9 | 7 | 9 | 80.89 | 66.06 |
| OLS-GP | No | 10 | 10 | 10 | 8.08 | 8.2 |

# Chapter 8

# Summary and Future Work

## Preface

In this chapter the performance of all candidate techniques studied in the earlier chapters toward a *robust* structural health monitoring under uncertainty is summarized. The main findings of each analysis have been highlighted. Some potential future work directions are also outlined at the end of the chapter.

## 8.1 Summary

In this dissertation, the concept of uncertainty analysis in structural health monitoring was studied. The main motivation of the work was implementing advanced statistical pattern recognition techniques capable of considering variations in input parameters and eventually developing a structural monitoring system immune to uncertainty of training parameters. For this reason, Chapter 2 provided a comprehensive literature review on the successful applications of structural health monitoring in different industries and the impact of uncertainty on the reliability and robustness of the developed systems. Chapter 3 reviewed the mathematical considerations of the conventional algorithms commonly used for pattern recognitions, as well as outlining the background of the proposed novel GP approach for SHM.

Chapters 4, 5 were feasibility studies (proof of concepts) for the impact of uncertainty on the accuracy and robustness of the structural health monitoring of two different composite structures; namely, a T-joint and an airfoil. Chapter 4 statistically studied the impact of misalignment of fibers and loading deviation (as possible sources of uncertainty in practice), on the strain patterns of the T-joint under tensile loading. The structure was subjected to five different factors (fiber misalignments in four components of the structure as well as the deviation of loading direction), each having two levels. The strain measurement was carried out in two ways; first by measuring along three distinct sensor points (called point-to-point analysis) and the second by a continuous approach (called integral analysis). This feasibility study showed that **the uncertainty can be as important as the damage itself and increasing the number of sensors cannot necessarily eliminate the noise effect for subsequent SHM training and predictions.** Also for this case study, statistically, **no significant interaction was observed between the fabrication/testing parameters and the damage; i.e. the noise effects caused by the misalignment of fibers and deviation of vertical tensile loading were comparable for all damage scenarios.**

Chapter 5 then took over a different and more complex case study to evaluate the impact of uncertainty in the robustness of the structural health monitoring system. Unlike the previous chapter, in Chapter 5 the thickness variation is considered as the main source of production uncertainty. Early in Chapter 5, a common symmetric airfoil profile was studied experimentally and numerically under three different damage scenarios (artificial delamination). For each damage scenario, five different thicknesses for each ply of the composite airfoil were assumed to represent manufacturing uncertainty. The variation in the strain field measured at each sensory point was studied separately, trying to correlate the variation to the thickness variation (noise) and/or the presence of damage itself (signal). Only for about one fourth of the sensors, the deviation directly corresponded to the presence of damage and all the rest of sensors were capturing the strain change caused because of noise instead of the damage; i.e. almost three fourth of the sensors were not able to focus on the damage and all the variations measured at them could only be correlated to the manufacturing uncertainty (noise). Later in the same chapter, to check the generalization of the latter conclusion to a large damage database signature, the same ANOVA analysis was repeated with several (162) damage scenarios of different sizes and locations. For each one of these scenarios one model with original (nominal) ply thicknesses and five models with randomly changed thicknesses were developed via the FE analysis of the airfoil. The ANOVA of resulting strain distributions showed that this time, none of the sensors in the airfoil could distinguish between thickness variation (uncertainty) and the presence of damage (main parameter of SHM). This chapter was a turning point in our study because it statistically proved that **a 'robust' structural health monitoring system requires a different approach than conventional techniques (such as adding more number of damage scenarios to database, or propagating/checking the uncertainty effect after the SHM model is trained, etc). Otherwise, in practice, the signal variations caused by manufacturing/material/testing noises can potentially lead to false alarms by the SHM system.**

In Chapter 6, a conventional Artificial Neural Networks (ANN) and its modification were studied for damage prediction of the airfoil example studied in Chapter 5. The Multi-Layer Perceptron (MLP) neural network was chosen because it is the basis of most of the networks studied currently in the literature for SHM applications. The developed neural network showed great accuracy when was trained and predicted the same type of DSD. The DSD could consist of the nominal damage scenarios with no noise (called 'nominal DSD') or be combination original and thickness-varying damage scenarios (called 'total DSD'). **The developed NN showed poor prediction quality when being trained by the nominal DSD and trying to predict the total DSD under uncertainty.** For this reason, later in Chapter 6, a new Signal-to-Noise (SN) based NN was introduced to provide meaningful weights for the input layer of the MLP network that would possibly minimize the prediction error caused by the uncertainty effect. **Among different types of SN, the dynamic SN weighted neural network showed an outstanding accuracy of**

**~90% in damage prediction**. **The practical problem with this approach, however, is estimating of the proper SN ratios. This estimation may come from past experience, knowledge expert or by developing a large initial database encompassing several uncertainty cases. This is against our mission which aimed to minimize the risk and *cost* of uncertainty analysis for the SHM applications**; therefore, in the next chapter another new approach was investigated.

In Chapter 7, Gaussian Processes (GPs) which are very powerful mathematical algorithms for pattern recognition problems were studied. In a GP, no particular input-output model, unlike the ordinary least square (OLS) regression or NN, is imposed on the algorithm. The only decision the user should make is on the type of dependency (correlation) that each pair of input points in the training dataset have on each other-- which is expressed by the choice of a covariant function. Different types of covariant functions were numerically simulated in MATLAB and results were astonishing in the airfoil case study. **Only training the GP with the nominal DSD via a Rational Quadratic (RQ) covariant function was able to get an accuracy of ~90% in predicting the size and location of damage in all cases (total DSD) under uncertainty**. Another difference between the GP and the earlier method was found to be in regard to the addition of SN ratios to the input layer of training dataset. **Unlike the NN, the weighted GP did not lead to improved results.** In fact, the addition of SN ratios led to the divergence of the most optimum GP (i.e., the one with the covariant function of type RQ). The last idea in Chapter 7 was combining the GP and a linear OLS regression which is commonly referred to as Regression-Kriging or RK. **The RK approach is very common in geo-statistics but did not resulted in an improved outcome in the present case study, unless more sophisticated (higher order) models were used for the OLS training part or when it is trained with the noisy DSD**, which is again against our goal to arrive at a robust SHM with a minimal cost for practical implementations.

At last, Table 8.1 summarizes all the top ranked candidate approaches that were found in this dissertation dealing with the uncertainty effect in SHM of the airfoil composite structure. In the same table, the approximate time encountered during the implementation of each method is also included. Given the implementation time and the lack of need for weighting the training data, the GP SHM (specially the RQ type) appears to be most appealing in this study. **To find the**

**optimum architecture for the NN SHM, the cross validation took almost three weeks (24 hours a day), but in the GP it took almost a day. The individual run time of the GP is also considerably shorter than the NN.** The summary of the findings of this research regarding the application of conventional NN, SN weighted NN, and GP for a robust structural health monitoring is as follows:

- Conventional Neural Networks (NNs), of different number of hidden layers, were not able to handle uncertainty on their own.
- A conventional NN, however, can perform well if trained with noise scenarios, which is practically expensive.
- A dynamic signal-to-noise (weighted) NN approach can improve the performance of NN dramatically. However, the performance of weighted NN is highly sensitive to the estimation of signal-to-noise ratios, hence again not practical.
- Gaussian Process SHM, by itself (without any weighting or need for noise information during training), was capable of predicting all damage scenarios in the presence of uncertainty. This would be closer to the will of manufacturers in real-world applications (lower implementation time, lower number of training datasets/lower cost, reasonably reliable and robust prediction of damage).

**Some practical insights:**

One very interesting issue to notice in Table 8.1 is that for most of the top ranked techniques (say with accuracies > 70%), the accuracy in damage size prediction is greater than the accuracy in location prediction. This is seen as a good outcome for brittle materials such as composites since in such materials during service, the damage propagation would be sudden and in a short period of time, and hence to minimize catastrophic failure the SHM designer would prefer to be certain about the accuracy of damage extent prediction.

In ductile materials the story is different. In such materials, since the damage development process is normally smooth/more gradual, inspectors would have enough time to put the structure out of service and conduct comprehensive on-ground NDT tests over the damaged parts. Hence, in ductile structures the accuracy in location prediction would be of more importance.

There is another important issue that should be addressed here, and that is whether or not the obtained ~90% accuracy with the GP-RQ method is enough for practical applications. The answer, as outlined briefly above, would depend on many parameters such as the type of material, damage tolerance of the structure and the side maintenance schedules. For a ductile structure the proposed accuracy seems quite satisfactory, but for a brittle structure, because of the sudden damage-development nature, more accurate SHM systems might be needed. In either way, in this dissertation only a few numbers of possible covariant functions, under a single-covariant architecture formulation, were tested and one can always improve the accuracy by studying more number of covariant functions, or combining them.

The last concern regarding practical implementations of the proposed GP SHM approach goes back to the choice of optimum GP algorithm. As addressed in Chapter 7, Table 7.2, by training different types of GP with the nominal scenarios and predicting for the same type of dataset, many of the covariant functions demonstrated high accuracy (over 95%). This makes it hard to decide on an optimum covariant function for a given application by relying on nominal database only. In this dissertation, the FE developed noisy damage scenarios were used to assess the accuracy of different covariant functions and in this way, they revealed distinguishable performances, whereby the RQ-type showed superiority. In practical (cost-sensitive) applications, however, when such a comprehensive database is not provided, one can start by experimenting/running only a small portion of the noisy database (say 10% of the total) in order to choose an appropriate covariant function. If there is an outstanding function, it can be selected and used to finalize the training and predict the remaining damage scenarios under uncertainty. However, if no covariant function makes a good prediction at this stage, one may repeat the procedure but by considering say 20% of noisy database. This process can continue until a satisfactory covariant function is chosen. The other possible, and perhaps most cost-effective, solution would be to use only a portion of given nominal database for training and keep the rest to compare the performance of different covariant functions.

**Table 8.1.** Summary of all different approaches to deal with manufacturing uncertainty in structural health monitoring of the composite airfoil studied; all values are for the case of training with nominal DSD and predicting the total DSD.

| Overall ranking | Technique | Weights used? | Rank in damage size prediction | Rank in damage location prediction | Architecture optimization time | Individual run-time |
|---|---|---|---|---|---|---|
| 1 | **SN-D** – NN | YES | 1 (92.22%) | 1 (91.18%) | Three straight weeks | Up to 15 minutes |
| 2 | **GP** with RQ | NO | 2 (88.12%) | 2 (86.16%) | Less than a day | A minute |
| 3 | **GP** with NN | NO | 3 (86.04%) | 3 (80.89%) | Less than a day | A few seconds |
| 4 | **GP** with SE | YES | 4 (84.52%) | 5 (77.42%) | Less than a day | A few seconds |
| 5 | **GP** with NN | YES | 7 (78.22%) | 4 (79.57%) | Less than a day | A few seconds |
| 6 | **GP** with SE | NO | 5 (80.70%) | 6 (70.73%) | Less than a day | A few seconds |
| 7 | **SN-L** NN | NO | 6 (79.00%) | 7 (70.58%) | Three straight weeks | Up to 15 minutes |
| 8 | **SN-T** NN | NO | 8 (52.67%) | 8 (59.96%) | Three straight weeks | Up to 15 minutes |
| 9 | **Not-weighted** NN | NO | 9 (35.54%) | 9 (57.17%) | Three straight weeks | Up to 15 minutes |

## 8.2. Future work

In this dissertation the effect of sensor architecture is briefly addressed in Chapter 4 and was assumed to be fixed in the rest of the thesis. However, it can have a considerable impact on the performance of a developed SHM system. Therefore, implementing information theory to find optimum sensor patterns and assessing the impact of different sensor architectures on the performance of developed GP SHM approach can be a worthwhile subject for future studies. Such an effort would cover subjects such as:

1. Optimum number of sensors
2. Optimum sensor locations
3. Fail-safe sensor architecture designs

Also in this dissertation the performance of the new GP approach and the NN weighted with SN ratios were only studied under static tensile loading. However, most of the loads applied to structures in service are dynamic and/or under combined loading modes (tensile, bending, torsion, etc.). Therefore, another very important direction for future work can be evaluating the performance of GP under different loading regimes.

Finally, aging of the composite structures has recently been one of the main concerns for manufactures. The impact of ageing in the form of material deterioration (specially the resin), wide-spread fatigue damages, etc. is needed to be addressed for modern SHM systems. Investigating the impact of structural aging on the performance/ predictability of the proposed algorithms in this thesis (weighted NN and GP) may be another potential direction for future research.

# References

## References of Chapters 1, 2, 3, 6, 7 and 8

[1] C. Boller, N. Meyendorf. State-of-the-Art in Structural Health Monitoring for Aeronautics. Proceeding of the International Symposium on NDT in Aerospace, Fürth/Bavaria, Germany, December 3-5, 2008.

[2] Edited by D. Balageas, C.P. Fritzen, A. Gumes. Structural Health Monitoring. Printed and bound in Great Britain by Antony Rowe Ltd. Chippenham, Wiltshire, 2006.

[3] I. Perez, M. DiUlio, S. Maley, N. Phan. Structural Health Monitoring in the Navy. International Journal of Structural Health Monitoring 9(3): 199, 2010.

[4] J. M. Lopez-Higuera. Introduction to optical fiber sensor technology. Handbook of Optical Fibre Sensing Technology. J. M. Lopez-Higuera, Ed. New York: Wiley, 2002, 1–21, 2002.

[5] H.V.D. Auweraer, B. Peeters. International research projects on Structural Health Monitoring: An overview. International Journal of Structural Health Monitoring. 2: 341, 2003.

[6] C. R. Farrar, K. Worden. An Introduction to Structural Health Monitoring. Philosophical Transactions of the Royal Society A 365, 303, 2007.

[7] I. Searle, S. Ziola, S. May. Damage detection experiments and analysis for the F-16. 1st European Workshop on Structural Health Monitoring, 310, 1997.

[8] R. Ikegami. Structural Health Monitoring: assessment of aircraft customer needs Structural Health Monitoring 2000. Proceedings of the Second International Workshop on Structural Health Monitoring, Stanford, CA, September 8-10, Lancaster-Basel, Technomic Publishing Co, Inc, 12, 1999.

[9] I. Searle, S. Ziola, B. Seidel. Crack detection on a full-scale aircraft fatigue test2. Proceeding of SPIE Smart Sensing, Processing, and Instrumentation, 267, 1997.

[10] E.W. Obrien. Reduction of scatter factors by use of Structural Health Monitoring. European Workshop on Structural Health Monitoring, 294-297, 2002.

[11] C.A. Paget, K. Atherton, E. Obrien. Damage assessment in a full-scale aircraft wing by modified acoustic emission. Proceeding of the 2nd European Workshop on Structural Health Monitoring, July 7-9, Munich, Germany, 2004.

[12] T. Martin, I. Read, P. Foote. Automated notification of structural damage for Structural Health Management using acoustic emission detection. 4th European Workshop on Structural Health Monitoring, 828-835, 2003.

[13] S. Hunt, I. Hebden. Eurofighter 2000 Structural health and usage monitoring: an integrated approach. Proceeding 2nd Joint NASA/FAA/DOD Conference on Aging Aircraft, 1999.

[14] S. Hunt, I. Hebden. Validation of the Eurofighter Typhoon structural health and usage - monitoring system F3-2000. International Journal of Structural Health Monitoring 743–752, 2000.

[15] R.D. Finlayson, M. Friesel, M. Carlos, P. Cole, J.C. Lenain. Health Monitoring of Aerospace Structures with Acoustic Emission and Acousto-ultrasonics. Proceeding of the 15th World Conference on Non-Destructive Testing, 15-21 October 2000, Roma, Italy, 2000.

[16] M.A. Friesel, Y. Ji, W. Yan, R.K. Miller, and M.F. Carlos. Helicopter Drivetrain Damage Detection and Classification using Acoustic Emission and a Kinematic Variable. Journal of the American Helicopter Society, Fall 1999.

[17] C. Paget, H. Speckmann, T. Krichel and F. Eichelbaum. Validation of SHM sensors in Airbus A380 full scale fatigue test Chapter 105. Encyclopedia of Structural Health Monitoring, 2009.

[18] F.M. Hemez. Uncertainty, validation of computer models and the myth of numerical predictability. Los Alamos National Laboratory Report, 2001.

[19] G. Manson, K. Worden, D.J. Allman. Experimental validation of a Structural Health Monitoring methodology-Part II. Novelty detection on a Gnat aircraft Journal of Sound and Vibration, 259 (2): 345-363, 2003.

[20] G. Manson, K. Worden, D.J. Allman. Experimental validation of a Structural Health Monitoring methodology-Part III. Damage location on an aircraft wing Journal of Sound and Vibration, 259 (2): 345-363, 2003.

[21] G. Manson, K. Worden, G. Pierce, T. Denoeux. Uncertainty analysis Chapter 49, Encyclopedia of Structural Health Monitoring, 2009.

[22] W. Staszewski, K. Worden. Signal Processing for Damage Detection in Health Monitoring of Aerospace Structures – Smart Sensor Technologies and Signal Processing, J. Wiley & Sons, Chichester, 2004, 163-203, 2004.

[23] W. Fan, P. Qiao. Vibration-based damage identification methods: A review and comparative study Structural Health Monitoring 10: 83-113, 2011.

[24] S.W. Doebling, C.R. Farrar, M.B. Prime, D.W. Shevit. Damage Identification and Health Monitoring of Structural and Mechanical Systems from Changes in their Vibration Characteristics: A Literature Review Los Alamos National Laboratory report, (LA-13070-MS), 1996.

[25] H. Sohn, C. Farrar, N. Hunter, K. Worden. A Review of Structural Health Monitoring Literature: 1996–2001 Los Alamos National Laboratory report, (LA-13976-MS), 2003.

[26] E.P. Carden, P. Fanning. Vibration based condition monitoring: A review Structural Health Monitoring, 3, 355–377, 2004.

[27] J. M. López-Higuera, L. R. Cobo. Fiber Optic Sensors in Structural Health Monitoring Journal of Lightwave Technology, VOLUME 29, NO. 4, February 15, 2011.

[28] R.S. Geng. Application of acoustic emission for aviation industry – problems and approaches, Proc of the 16th WCNDT 2004 - World Conference on NDT, Aug 30 - Sep 3, 2004, Montreal, Canada, 2004.

[29] K.W. Dittrich, G. Mueller. In-flight measurement of acoustic background noise for the development of impact detection algorithms, Proceeding SPIE, Volume 5046, 2003, 263- 271, 2003.

[30] C. Paget, H. Speckmann, T. Krichel, F. Eichelbaum. Validation of SHM Sensors in Airbus A380 Full-Scale Fatigue Test. Encyclopedia of Structural Health Monitoring, John Wiley & Sons, Ltd. 2009.

[31] Yago Gómez-Ullate Ricón, Francisco Montero de Espinosa Freijo. Piezoelectric Transducers for Structural Health Monitoring: Modeling and Imaging. Piezoelectric Transducers for Structural Health Monitoring: Modeling and Imaging, Springer Series in Materials Science, Volume 140, 727-772, 2011.

[32] J. Hawood, P.T. Coverley, W.J. Staszewski, K. Worden. An automatic impact monitor for a composite panel employing smart sensor technology, Smart Materials and Structures, 14, 265-271, 2005.

[33] C. Pardo De Vera, J.A. Guemes. Embedded self-sensing piezoelectric for damage detection. Proceedings of the International Workshop on Structural Health Monitoring, September 18-20, Stanford, CA 445-455, 1997.

[34] V. Giurgiutiu, J. Bao, W. Shao. Active sensor wave propagation health monitoring of beam and plate structures. Proceeding of SPIE, Volume 4327, 234-245, 2001.

[35] C. Bois, C. Hochard. Measurements and modeling for the monitoring of damaged laminate composite structures. 1st European Workshop on Structural Health Monitoring, 425-432, 2002.

[36] M. Kemp. Self-sensing composites for smart damage detection using electrical properties, Proceedings of 2nd European Conference on Smart Structures and Materials (ECSSM 2). 12-14 October 1994, Glasgow, 1994.

[37] R. Schueler, S.P. Joshi, K. Schulte. Damage detection in CFRP by electrical conductivity mapping. Composites Science and Technology, Volume 61, no. 6, 921-930, 2001.

[38] L. Hou, S.A. Hayes. A resistance-based damage location sensor for carbon fiber composites. Smart Materials and Structures, Volume 11, 2002, 966-969.

[39] N. Angelidis, N. Khemiri, P.E. Irving. Experimental and finite element study of the electrical potential technique for damage detection in CFRP laminates. Smart Materials and Structures, Volume 14, no. 1, 147-154, 2005.

[40] H. Guo, G. Xiao, N. Mrad, and J. Yao. Fiber Optic Sensors for Structural Health Monitoring of Air Platforms. International Journal of Sensors, 11, 3687-3705.

[41] J. Gomez, J. Zubia, G. Aranguren, J. Arrue, H. Poisel, I. Saez. Comparing polymer optical fiber, fiber Bragg grating, and traditional strain gauge for aircraft structural health monitoring. APPLIED OPTICS, Volume 48, No. 8, March 2009.

[42] I. R. Husdi, K. Nakamura, and S. Ueha, Sensing characteristics of plastic optical fibres measured by optical time domain reflectometry. Measurement Science and Technology, Volume 15, no. 8, 1553–1559, 2004.

[43] K. Nakamura, I. R. Husdi, and S. Ueha, A distributed strain sensor with the memory effect based on the POLYMER OPTICAL FIBER OTDR. SPIE 17th International Conference on Optical Fibre Sensors, 2005, Volume 5855, 807–810.

[44] S. Liehr, P. Lenke, K. Krebber, M. Seeger, E. Thiele, H. Metschies, B. Gebreselassie, J. H. Münich, and L. Stempniewski. Distributed strain measurement with polymer optical fibers integrated into multifunctional geotextiles. SPIE, 2008, Volume 7003, 700302–700302-15.

[45] P. Lenke, S. Liehr, K. Krebber, F.Weigand, and E. Thiele. Distributed strain measurement with polymer optical fiber integrated in technical textiles using the optical time domain reflectometry technique. POLYMER OPTICAL FIBER Conference, 2007, 21–24.

[46] J. Brendel. Optical time-domain reflectometry for POLYMER OPTICAL FIBER test and measurement, in Proceeding POLYMER OPTICAL FIBER Conference, 2001, 45–50.

[47] S. Liehr, P. Lenke, M. Wendt, K. Krebber, M. Seeger, E. Thiele, H. Metschies, B. Gebreselassie, J. Christian Münich. Polymer Optical Fiber Sensors for Distributed Strain Measurement and Application in Structural Health Monitoring, IEEE SENSORS JOURNAL, VOLUME 9, NO. 11, NOVEMBER 2009.

[48] Health Monitoring for Airframe Structural Characterization, NASA/CR-2002-211428.

[49] Ch.E. Katsikeros, G.N.Labeas. Development and validation of a strain-based Structural Health Monitoring system. Mechanical Systems and Signal Processing 23 (2009) 372– 383.

[50] K. Koski, J. Tikka, M. Ba¨ckstro¨m, A. Siljander, S. Liukkonen, G. Marquis. An aging aircraft's wing under complex multiaxial spectrum loading: Fatigue assessment and repairing. International Journal of Fatigue 28 (2006) 652–656.

[51] S. Kim, S. Pakzad, D. Culler, J. Demmel, G. Fenves, S. Glaser, M. Turon. Health Monitoring of Civil Infrastructures Using Wireless Sensor Networks. Proceedings of the 6$^{th}$ International Conference on Information Processing in Sensor Networks (IPSN 2007), Cambridge, MA, USA, 25-27 April, 2007.

[52] H. Choi, S. Choi, H. Cha. Structural Health Monitoring System based on Strain Gauge Enabled Wireless Sensor Nodes. Department of Computer Science, Yonsei University, Korea.

[53] Hybus incorporated, H-mote, http://www.hybus.net/lan_english/

[54] T. R. F. Fulford-Jones, G. Wei, M. Welsh. A Portable, Low-Power, Wireless Two-Lead EKG System. 26th IEEE EMBS Annual International Conference, San Francisco, CA, USA, 1-5 September 2004.

[55] G.M. Kamath, Ramesh Sundaram, Nitesh Gupta, M. Subba Rao. Damage Studies in Composite Structures for Structural Health Monitoring using Strain Sensors. Structural Health Monitoring 2010 9: 497 originally published online 12 March 2010.

[56] D. C Betz, G. Thursby, B. Culshaw, W. J Staszewski. Acousto-ultrasonic sensing using fiber Bragg gratings. Smart Materials and Structures 12 (2003) 122–128.

[57] A. Cusano, P. Capoluongo, S. Campopiano, A. Cutolo, M. Giordano, F. Felli, A. Paolozzi, and M. Caponero. Experimental Modal Analysis of an Aircraft Model Wing by Embedded Fiber Bragg Grating Sensors, IEEE SENSORS JOURNAL, VOLUME 6, NO. 1, FEBRUARY 2006.

[58] M. Benedetti, V. Fontanari and D. Zonta. Structural health monitoring of wind towers: remote damage detection using strain sensors. Smart Materials and Structures 20 (2011).

[59] H. Sohn, C.K. Oh, Statistical pattern recognition. Encyclopedia of Structural Health Monitoring, 2009.

[60] F. Chu, S. Yuan and Z. Peng, Machine learning techniques. Encyclopedia of Structural Health Monitoring, 2009.

[61] H. Azzam. A practical approach for the indirect prediction of structural fatigue from measured flight parameters. Proceeding of the Institution of Mechanical Engineering, Part G, Journal of Aerospace Engineering 211(G1) 29-38, 1997.

[62] H. Azzam. The use of mathematical models and artificial intelligent techniques to improve hums prediction capabilities. Proceedings of the Royal Aeronautical Society, Innovation in Rotorcraft Technology Conference. London. 1997.

[63] H. Azzam, I. Hebden, L. Gill, F. Beavan, M. Wallace. Fusion and decision making techniques for structural prognosis health management. IEEE Aerospace Conference, Paper # 1535, Montana MT, 2005.

[64] M. Wallace, H. Azzam, S. Newman. Indirect approaches to individual aircraft structural monitoring. Proceeding of the Institution of Mechanical Engineering, Part G, Journal of Aerospace Engineering 218(G1) 329-346, 2004.

[65] S.C. Reed, D.G. Cole. Development of a parametric aircraft fatigue monitoring system using artificial neural network. 22nd Symposium of the International Committee on Aeronautical Fatigue, EMAS publishing: Sheffield 47-63, 2003.

[66] G. Scallonila, J. Cracia, J. Cabrejas, JI. Armijo. A full-scale parametric based fatigue monitoring system using neural networks. Presented at the 24th Symposium of the International Committee on Aeronautical Fatigue, Naples 2007.

[67] O. Levinski. Australian Defense Science and Technology Organization. Prediction of buffet loads using artificial neural network, Document DSTO-RR-0218, 2001.

[68] V. Lopes, Jr. G. Park, HH. Cudney, DJ. Inman. Smart structures health monitoring using artificial neural network. Journal of Structural Health Monitoring 976-385, 2000.

[69] K. Gurney. An introduction to neural networks, First edition. University of Sheffield, 1997.

[70] S. Haykin. Neural Networks-A Comprehensive Foundation, 2nd edition. Prentice-Hall Inc., USA, 1997.

[71] X. Fang, H. Luo and J. Tang. Structural Damage Detection using Neural Network with Learning Rate Improvement. Computers and Structures,Volume 83, no.25, 2150-2161, 2005.

[72] A. Kesavan, S. John, I. Herszberg. Strain-based Structural Health Monitoring of complex composite structures. Structural Health Monitoring 7, 203-213, 2008.

[73] M.S . Al-Haik, MY. Hussaini, H. Garmestani. Prediction of Nonlinear Viscoelastic Behaviour of Polymeric Composites using an Artificial Neural Network. International Journal of Plasticity, vol.22, no.7, 1367–1392, 2006.

[74] R. Koker, N. Altinkok, A. Demir. Neural Network based Prediction of Mechanical Properties of Particulate Reinforced Metal Matrix Composites using various Training Algorithms. Journal of Materials and Design, 2006.

[75] AP. Singh, TS. Kamal, S. Kumar. Virtual Curve Tracer for Estimation of Static Response Characteristics of Transducers. Journal of Measurement, Volume 38, no.2, 166-175, 2005.

[76] C.E. Rasmussen and C. K. I. Williams. Gaussian Processes for Machine Learning. The MIT Press, ISBN 0-262-18253-X, 2006.

[77] A. McHutchon, C.E. Rasmussen. Gaussian Process Training with Input Noise. Proceeding of Neural Information Processing Systems Foundation, 2011.

[78] S. Grossberg. Studies of Mind and Brain, Neural Principles of Learning, Perception, Development, Cognition, and Motor Control. Springer, 1982.

[79] M.L. Stein. Interpolation of Spatial Data. Springer-Verlag, New York, 1999.

[80] I.I. Gihman, A.V. Skorohod. The Theory of Stochastic Processes. Springer-Verlag, Berlin, 1974.

[81] R. von Mises. Mathematical Theory of Probability and Statistics. Academic Press, 1964.

[82] A. O'Hagan. Curve Fitting and Optimal Design for Prediction. Journal of the Royal Statistical Society B, 40:1–42, 1978.

[83] F.P. Agterberg. Georges Matheron: Founder of Spatial Statistics. Geological Survey of Canada, 2005.

[84] M. P. Deisenroth, D. Fox, and C. E. Rasmussen. Gaussian Processes for Data-Efficient Learning in Robotics and Control. IEEE Transactions on Pattern Analysis and Machine Intelligence, 22 May 2014.

[85] D. C. McFarlane and K. Glover. Lecture Notes in Control and Information Sciences. Chapter Robust Controller Design using Normalised Coprime Factor Plant Descriptions. Volume 138, Springer- Verlag, 1989.

[86] K. J. Astr¨om and B. Wittenmark. Adaptive Control. Dover Publications, 2008.

[87] B. Wittenmark. Adaptive Dual Control Methods: An Overview. IFAC Symposium on Adaptive Systems in Control and Signal Processing, 1995.

[88] S. Fabri and V. Kadirkamanathan. Dual Adaptive Control of Nonlinear Stochastic Systems using Neural Networks. Automatica, 34(2):245–253, 1998.

[89] A. A. Fel'dbaum. Dual Control Theory, Parts I and II. Journal of Automation and Remote Control, 21(11):874–880, 1961.

[90] J. A. Bagnell and J. G. Schneider. Autonomous Helicopter Control using Reinforcement Learning Policy Search Methods. International Conference on Robotics and Automation, 2001.

[91] J. G. Schneider. Exploiting Model Uncertainty Estimates for Safe Dynamic Control Learning. In Advances in Neural Information Processing Systems. 1997.

[92] B. Berger and F. Rauscher. Evaluation of Gaussian processes for black-box engine modelling. 6th Conference Design of Experiments (DoE) in Engine Development, 2011.

[93] B. Berger, F. Rauscher, and B. Lohmann. Analysing Gaussian processes for stationary black-box combustion engine modelling. 18th IFAC World Congress, Milano, Italy, 2011.

[94] B. Berger and F. Rauscher. Robust Gaussian Process Modelling For Engine Calibration. 7th Vienna International Conference on Mathematical Modelling (MATHMOD 2012), Vienna University of Technology, Vienna, Austria, 2012.

[95] W. Y. Fowlkes, C. M. Creveling. Engineering Methods for Robust Product Design: Using Taguchi Methods in Technology and Product Development. Prentice Hall, Chapter 6: The Static Signal to Noise Ratios, 2013.

[96] W. Y. Fowlkes, C. M. Creveling. Engineering Methods for Robust Product Design: Using Taguchi Methods in Technology and Product Development, Prentice Hall, Chapter 7: The Dynamic Signal-to-Noise Methods and Metrics, 2013.

[97] M. Welvaert, Y. Rosseel. On the Definition of Signal-To-Noise Ratio and Contrast-To-Noise Ratio for fMRI Data. Public Library of Science 8(11) 2013.

[98] L. Griffantia, F. Baglioa, M. G. Pretia, P. Cecconic, M. Rovarisd, G. Basellib, M. M. Laganà. Signal-to-noise ratio of diffusion weighted magnetic resonance imaging: Estimation methods and in vivo application to spinal cord. Biomedical Signal Processing and Control 7, 285–294, 2012.

[99] Suranai Poungponsri, Xiao-Hua Yu. An adaptive filtering approach for electrocardiogram (ECG) signal noise reduction using neural networks. Neurocomputing 117, 206–213, 2013.

[100] Zhenqing Liu, Mingda Lu, Moan Wei. Structure noise reduction of ultrasonic signals using artificial neural network adaptive filtering. Ultrasonics 35, 325-328, 1997.

[101] Lingyun Zou, Zhengzhi Wang, Jiaomin Huang. Prediction of Subcellular Localization of Eukaryotic Proteins Using Position-Specific Profiles and Neural Network with Weighted Inputs. Journal of Genetics and Genomics, 34(12): 1080-1087, 2007.

[102] Tao Chen, Xiao-li Xu1, and Shao-hong Wang. An Intelligent Prediction Method Based on Information Entropy Weighted Elman Neural Network, Intelligent Computing and Information Science. International Conference on Industrial and Information Systems, Chongqing, China, January 8-9, 2011 Proceedings, Part II.

**References of Chapter 4**

[1] Christian BOLLER, Norbert MEYENDORF. State-of-the-Art in Structural Health Monitoring for Aeronautics Proceeding of International Symposium on NDT in Aerospace. Fürth/Bavaria, Germany, December 3-5, 2008.

[2] Charles R. FARRAR, Keith WORDEN. An Introduction to Structural Health Monitoring. Philosophical Transactions of the Royal Society A 365, 303–315, 2007.

[3] C. Boller, M. Buderath. Fatigue in aerostructures – where structural health monitoring can contribute to a complex subject. Philosophical Transactions of the Royal Society 365, 561–587, 2007.

[4] R. Ikegami. Structural Health Monitoring: assessment of aircraft customer needs Structural Health Monitoring 2000. Second International Workshop on Structural Health Monitoring, Stanford, CA, September 8-10, 1999.

[5] J.M.W. BROWNJOHN. Structural Health Monitoring of Civil Infrastructure. Philosophical Transactions of the Royal Society 365, 589-622, 2007.

[6] Light Structures Inc. Exploration & Production: The Oil & Gas Review, Volume 2, 2003.

[7] Ved Prakash SHARMA, J.J. Roger CHENG. Structural Health Monitoring of Syncrude's Aurora II Oil Sand Crusher University of Alberta. Department of Civil & Environmental Engineering, Structural Engineering Report No 272, 2007.

[8] D. BARKE, W.K. CHIU. Structural Health Monitoring in Railway Industry: A Review. Structural Health Monitoring 4, 81-93, 2005.

[9] B.R. RANDALL. State of the Art in Monitoring Rotating Machinery – Part I. Journal of Sound and Vibrations 38, March, 14-21, 2004.

[10] B.R. RANDALL. State of the Art in Monitoring Rotating Machinery – Part II. Journal of Sound and Vibrations 38, May, 10-17, 2004.

[11] B. Tang, Orthogonal array-based Latin hypercubes Journal of the American Statistical Association, 88(424):1392–1397, 1993.

[12] J.-S. Park. Optimal Latin-hypercube designs for computer experiments. Journal of Statistical Planning and Inference, 39:95–111, 1994.

[13] X. Qu, G. Venter, R.T. Haftka. New formulation of minimum bias central composite experimental design and Gauss quadrature. Structural and Multidisciplinary Optimization, 28:231–242, 2004.

[14] R. Jin, W. Chen, A. Sudjianto. An efficient algorithm for constructing optimal design of computer experiments. Journal of Statistical Planning and Inference, 134:268–287, 2005.

[15] T.W. Simpson, D.K.JOURNAL OF Lin, W. Chen. Sampling strategies for computer experiments: Design and analysis. International Journal of Reliability and Applications, 2(3):209–240, 2001.

[16] R.H. Myers, D.C. Montgomery. Response Surface Methodology—Process and Product Optimization Using Designed Experiments. New York: Wiley, 1995.

[17] A. Kesavan, S. John, I. Herszberg. Strain-based structural health monitoring of complex composite structures. Structural Health Monitoring, 7:203-213, 2008.

**References of Chapter 5**

[1] C. Boller, N. Meyendorf. State-of-the-art in structural health monitoring for aeronautics. International Symposium on NDT in Aerospace, Fürth/Bavaria, Germany, December 3-5, 2008.

[2] D. Balageas, C.P. Fritzen, A. Gumes. Structural Health Monitoring. Antony Rowe Ltd, Chippenham, Wiltshire, 2006.

[3] I. Perez, M. DiUlio, S. Maley, N. Phan. Structural health monitoring in the navy. International Journal of Structural Health Monitoring, 9(3): 199–9, 2010.

[4] JOURNAL OF M. Lopez-Higuera. Introduction to optical fiber sensor technology. Handbook of Optical Fibre Sensing Technology, Editor: JOURNAL OF M. Lopez-Higuera, New York: Wiley, 2002, 1–21, 2002.

[5] H. Teimouri, A.S. Milani, R. Seethaler. On the Effect of Fabrication and Testing Uncertainties in Structural Health Monitoring. Design of Experiments – Applications, Editor: M. Borges Silva, InTech Publisher (in press).

[6] A. Kesavan, S. John, I. Herszberg. Strain based structural health monitoring of complex composite structures. Structural Health Monitoring, 2008, 1-13.

[7] D.I. Kachlakev. Finite Element Method (FEM) Modeling for Composite Strengthening/Retrofit of Bridges. Research Project Work Plan, Civil, Construction and Environmental Engineering Department, Oregon State University, Corvallis, Oregon, 1998.

[8] D.I. Kachlakev. Strengthening Bridges Using Composite Materials. FHWA-OR-RD-98-08, Oregon Department of Transportation, Salem, Oregon, 1998.

[9] D.I. Kachlakev, and DJ. McCurry Junior. Simulated Full Scale Testing of Reinforced Concrete Beams Strengthened with FRP Composites: Experimental Results and Design Model Verification. Oregon Department of Transportation, Salem, Oregon, June 2000.

[10] www.NetComposites.com.

[11] M. Davis. Assessing Adhesive Bond Failures: Mixed-Mode Bond Failures Explained. ISASI Australian Safety Seminar, Canberra, June 2010.

[12] M. Davis, O.F. JOURNAL and D.A. Bond. The Importance of Failure Mode Identification in Adhesive Bonded Aircraft Structures and Repairs. Aircraft Structural Integrity Section Directorate, Royal Australian Air Force, ICCM 12, Paris, France, September 2008.

[13] E. Greene. Marine Composites. Eric Greene Associates, ISBN 0-9673692-0-7, Annapolis, MD, December 1999.

[14] N. Clegg. A Short Guide to Osmosis & its Treatment. Nigel Clegg Associates, Sedgefield, UK, 2009.

[15] M. Gower, G. Sims, R. Lee, S. Frost, and M. Wall. Measurement Good Practice Guide No. 78 Assessment and Criticality of Defects and Damage In Material Systems. National Physical Laboratory, Edington, Middlesex, United Kingdom, June 2005.

[16] M. Gower, G. Sims, R. Lee, S. Frost, and M. Wall. Measurement Good Practice Guide No. 78 Assessment and Criticality of Defects and Damage in Material Systems. National Physical Laboratory, Edington, Middlesex, United Kingdom, June 2005.

[17] E.E. Gdoutos and I.M. Daniel. Failure Mechanisms of Sandwich Structures. Theoretical Applied Mechanics, Volume 35, 105–118, 2008.

[18] D. Zenkert, A. Shipsha, P. Bull, and B. Hayman. Damage Tolerance Assessment of Composite Sandwich Panels with Localised Damage. Composites Science and Technology 65, Elsevier Ltd., 2005.

# Appendix

## Appendix A: Finite Element Modeling

In this section very briefly the Finite Element simulation process of the airfoil samples is explained. Table A.1 summarizes the damage scenarios used in terms of the corresponding delamination size and location. The model geometry, corresponding to the profile of the airfoil NACA0012, can be found in the airfoil database. The following steps have been taken to create the airfoil model in the ABAQUS software.

1. Creating parts (airfoil surfaces for composite layers beneath and above the core, connecting laminate and the volume for the PVC foam separately)
2. Defining material properties.
3. Defining composite sections, stacking sequence and the corresponding attributes.
4. Assembling the parts together.
5. Defining the constraints between parts.
6. Meshing the whole model.
7. Defining the external loading and boundary conditions.
8. Running the model.
9. Gathering strain information from the corresponding nodes.

Table A.1 Definition of the numerical damage scenarios (the location and extent of delamination between the PVC foam and the carbon layer beneath it; for the 162 numerical damage scenarios).

| DSD# | Damage length (mm) | Position (mm) of the middle point of delamination | DSD# | Damage length (mm) | Position (mm) of the middle point of delamination | DSD# | Damage length (mm) | Position (mm) of the middle point of delamination |
|---|---|---|---|---|---|---|---|---|
| 1 | 19.9 | 2.5 | 55 | 19.5 | 10.3 | 109 | 23.3 | 291.8 |
| 2 | 21.4 | 5.7 | 56 | 23.2 | 13.8 | 110 | 42.2 | 291.1 |
| 3 | 19.3 | 9.0 | 57 | 20.1 | 16.9 | 111 | 21.2 | 54.0 |
| 4 | 19.7 | 11.9 | 58 | 20.2 | 19.9 | 112 | 27.2 | 54.2 |
| 5 | 20.0 | 15.2 | 59 | 20.2 | 23.3 | 113 | 19.7 | 112.8 |
| 6 | 20.2 | 18.6 | 60 | 23.6 | 26.5 | 114 | 32.8 | 112.8 |
| 7 | 20.2 | 21.6 | 61 | 20.1 | 28.3 | 115 | 20.1 | 169.2 |
| 8 | 20.2 | 25.0 | 62 | 19.9 | 29.3 | 116 | 33.5 | 169.2 |
| 9 | 20.1 | 28.0 | 63 | 31.3 | 2.8 | 117 | 20.2 | 229.6 |
| 10 | 30.5 | 4.0 | 64 | 30.8 | 6.2 | 118 | 33.7 | 229.6 |
| 11 | 32.0 | 8.4 | 65 | 29.3 | 10.1 | 119 | 20.1 | 286.8 |
| 12 | 29.7 | 12.4 | 66 | 29.9 | 14.4 | 120 | 33.4 | 286.7 |
| 13 | 30.1 | 16.4 | 67 | 30.2 | 18.8 | 121 | 25.6 | 25.0 |
| 14 | 30.3 | 20.8 | 68 | 30.3 | 22.8 | 122 | 35.7 | 25.6 |
| 15 | 30.3 | 24.8 | 69 | 30.3 | 27.2 | 123 | 27.4 | 57.2 |
| 16 | 29.9 | 29.2 | 70 | 29.9 | 29.2 | 124 | 33.5 | 57.3 |
| 17 | 39.0 | 5.5 | 71 | 28.7 | 29.8 | 125 | 25.8 | 90.1 |
| 18 | 39.3 | 11.3 | 72 | 38.6 | 3.6 | 126 | 38.6 | 90.2 |
| 19 | 40.1 | 16.9 | 73 | 41.6 | 8.5 | 127 | 26.3 | 119.4 |
| 20 | 40.4 | 23.0 | 74 | 39.8 | 14.3 | 128 | 32.9 | 119.4 |
| 21 | 39.9 | 28.7 | 75 | 40.3 | 19.9 | 129 | 26.7 | 152.5 |
| 22 | 15.6 | 1.1 | 76 | 40.4 | 25.7 | 130 | 33.3 | 152.5 |
| 23 | 15.5 | 2.2 | 77 | 39.9 | 28.7 | 131 | 26.8 | 185.9 |

| | | | | | | | | |
|---|---|---|---|---|---|---|---|---|
| 24 | 15.5 | 3.2 | 78 | 42.2 | 29.1 | 132 | 33.6 | 185.9 |
| 25 | 18.6 | 4.2 | 79 | 30.8 | 25.2 | 133 | 26.9 | 216.2 |
| 26 | 19.0 | 5.1 | 80 | 41.4 | 25.5 | 134 | 33.7 | 216.2 |
| 27 | 18.4 | 6.2 | 81 | 27.4 | 57.2 | 135 | 27.0 | 249.8 |
| 28 | 19.5 | 7.2 | 82 | 39.5 | 57.5 | 136 | 33.7 | 249.8 |
| 29 | 19.6 | 8.2 | 83 | 32.2 | 90.1 | 137 | 26.8 | 280.1 |
| 30 | 19.7 | 9.2 | 84 | 45.0 | 90.2 | 138 | 33.5 | 280.1 |
| 31 | 19.8 | 10.5 | 85 | 26.3 | 119.4 | 139 | 25.1 | 39.8 |
| 32 | 19.9 | 11.4 | 86 | 39.4 | 119.4 | 140 | 35.8 | 40.5 |
| 33 | 19.9 | 12.4 | 87 | 26.7 | 152.5 | 141 | 24.6 | 83.2 |
| 34 | 19.9 | 13.4 | 88 | 40.0 | 152.5 | 142 | 38.4 | 83.8 |
| 35 | 20.0 | 14.4 | 89 | 33.6 | 185.9 | 143 | 23.1 | 124.3 |
| 36 | 20.0 | 15.4 | 90 | 40.3 | 185.9 | 144 | 36.3 | 124.3 |
| 37 | 20.0 | 16.4 | 91 | 26.9 | 216.2 | 145 | 23.4 | 164.1 |
| 38 | 20.1 | 17.4 | 92 | 40.4 | 216.2 | 146 | 30.1 | 164.2 |
| 39 | 20.1 | 18.4 | 93 | 33.7 | 249.8 | 147 | 23.6 | 207.7 |
| 40 | 20.1 | 19.1 | 94 | 40.4 | 249.8 | 148 | 37.0 | 207.8 |
| 41 | 20.1 | 20.4 | 95 | 26.8 | 280.1 | 149 | 23.6 | 248.2 |
| 42 | 20.1 | 21.4 | 96 | 40.2 | 280.0 | 150 | 37.1 | 248.2 |
| 43 | 20.1 | 22.5 | 97 | 19.6 | 39.5 | 151 | 23.3 | 291.8 |
| 44 | 20.1 | 23.5 | 98 | 37.9 | 39.5 | 152 | 36.4 | 291.6 |
| 45 | 20.1 | 24.5 | 99 | 25.6 | 83.7 | 153 | 27.2 | 54.2 |
| 46 | 20.1 | 25.5 | 100 | 44.9 | 84.0 | 154 | 33.1 | 54.3 |
| 47 | 20.1 | 26.5 | 101 | 23.1 | 124.3 | 155 | 26.2 | 112.8 |
| 48 | 20.1 | 27.5 | 102 | 42.8 | 124.4 | 156 | 32.8 | 112.8 |
| 49 | 20.1 | 28.5 | 103 | 23.4 | 164.1 | 157 | 26.8 | 169.2 |
| 50 | 20.0 | 29.5 | 104 | 43.4 | 164.2 | 158 | 33.5 | 169.2 |
| 51 | 19.6 | 30.5 | 105 | 16.8 | 207.7 | 159 | 27.0 | 229.6 |
| 52 | 19.4 | 1.8 | 106 | 37.0 | 207.8 | 160 | 33.7 | 229.6 |
| 53 | 22.6 | 4.1 | 107 | 16.8 | 248.2 | 161 | 26.7 | 286.8 |
| 54 | 19.2 | 7.4 | 108 | 37.1 | 248.2 | 162 | 33.4 | 286.7 |